

Doctoral T H E S I S

**Search for the Lepton Flavor  
Violating Decay  $\mu^+ \rightarrow e^+ \gamma$  With  
A Sensitivity of  $10^{-12}$**

by

**Xue Bai**

DEPARTMENT OF PHYSICS, SCHOOL OF SCIENCE

THE UNIVERSITY OF TOKYO

December 2012

---

## Abstract

The MEG experiment is a precise rare decay search designed to observe  $\mu^+ \rightarrow e^+\gamma$  or lack thereof as a sensitive low energy probe of new physics. In this thesis we present an updated result using the data taken in 2010, which correspond to  $1.1 \times 10^{14}$  muon decays in the stopping target.

The previous preliminary result based on the 2009 data gave a higher than expected upper limit of  $1.5 \times 10^{-11}$  at 90% C.L. with a few possible events in the signal region[1][2][3]. To examine this result, we analyzed the 2010 data which has twice higher statistical sensitivity than the 2009 data. In addition, we improved several aspects of calibration and analysis such as detector alignment, implementation of correlations in position observables, improved magnetic field map and improved likelihood analysis. We applied these improvements to the 2009 data and confirmed that that the excess signals still remain but the sensitivity is improved.

We adopted a "blind analysis" and a maximum likelihood fit. After unblinding the signal region, the number of  $\mu^+ \rightarrow e^+\gamma$  decay events in the data sample is extracted by a maximum likelihood fit. A 90% confidence interval is then constructed using the Feldman-Cousins technique. We evaluated an expected sensitivity of the 2010 data to be  $2.2 \times 10^{-12}$  by toy Monte Carlo experiment, which was also confirmed by analysis of the side band data. All the analysis is done by hiding the signal region until probability density functions for a likelihood fit are settled upon.

The obtained result is consistent with a null hypothesis and we set an upper limit on the branching ratio

$$B(\mu^+ \rightarrow e^+ \gamma) < 1.7 \times 10^{-12} \text{ at 90\% C.L.} \quad (1)$$

for the 2010 data and

$$B(\mu^+ \rightarrow e^+ \gamma) < 2.4 \times 10^{-12} \text{ at 90\% C.L.} \quad (2)$$

for the combined data of 2009 and 2010.

This result exceeds the previous world's best limit of  $1.2 \times 10^{-11}$  set by the MEGA experiment[4].

# Contents

<b>List of Figures</b>	<b>iii</b>
<b>List of Tables</b>	<b>v</b>
<b>1 Introduction</b>	<b>1</b>
<b>2 <math>\mu \rightarrow e\gamma</math> Decay</b>	<b>5</b>
2.1 Theoretical Background . . . . .	5
2.1.1 Standard Model and Beyond . . . . .	5
2.1.2 Muon Decay in the Standard Model . . . . .	6
2.1.3 SUSY and Lepton Flavor Violation . . . . .	8
2.2 Experimental Search . . . . .	13
2.2.1 History of $\mu \rightarrow e\gamma$ Search . . . . .	13
2.2.2 Signal and backgrounds of $\mu \rightarrow e\gamma$ . . . . .	15
2.2.3 Requirements of $\mu \rightarrow e\gamma$ Search . . . . .	18
<b>3 MEG Experiment</b>	<b>21</b>
3.1 Detectors Overview . . . . .	21
3.2 Beam . . . . .	23
3.2.1 Proton Accelerators . . . . .	23
3.2.2 $\pi$ E5 . . . . .	23
3.2.3 Beam Transport System . . . . .	23
3.3 Stopping Target . . . . .	27
3.4 Liquid Xenon Gamma-ray Detector . . . . .	28
3.4.1 Liquid Xenon . . . . .	28
3.4.2 Photomultiplier . . . . .	32

## CONTENTS

---

3.4.3	Design of LXe Detector . . . . .	32
3.4.4	Cryogenic System . . . . .	34
3.4.5	Purification System . . . . .	36
3.5	Positron Spectrometer . . . . .	38
3.5.1	COBRA Magnet . . . . .	38
3.5.2	Drift Chamber . . . . .	42
3.5.3	Timing Counter . . . . .	46
3.6	Calibration Apparatus . . . . .	50
3.6.1	Setup For $\pi^0$ Run . . . . .	50
3.6.2	Cockcroft-Walton Proton Accelerator . . . . .	53
3.7	Electronics and Data Acquisition . . . . .	54
3.7.1	Electronics Chain . . . . .	54
3.7.2	Data Acquisition System with MIDAS . . . . .	55
3.7.3	Waveform Digitization with DRS . . . . .	56
3.7.4	Trigger System . . . . .	56
3.8	Simulation and Analysis . . . . .	58
<b>4</b>	<b>Run 2010</b> . . . . .	<b>61</b>
4.1	Physics Run . . . . .	62
4.2	$\pi^0$ Run . . . . .	62
4.3	Calibration Runs . . . . .	63
4.4	Run Condition . . . . .	63
4.5	BTS problem . . . . .	65
<b>5</b>	<b>Event Reconstruction</b> . . . . .	<b>67</b>
5.1	Drift Chamber . . . . .	67
5.1.1	Waveform Analysis . . . . .	68
5.1.2	Hit Reconstruction . . . . .	69
5.1.3	Track Reconstruction . . . . .	69
5.1.4	Track Fitting . . . . .	70
5.2	Timing Counter . . . . .	71
5.2.1	Waveform Analysis . . . . .	71
5.2.2	Hit Reconstruction . . . . .	72
5.3	DCH-TIC Interconnection . . . . .	72

5.4	LXe Detector . . . . .	73
5.4.1	Waveform Analysis . . . . .	73
5.4.2	Photon Reconstruction . . . . .	75
5.4.3	Pileup . . . . .	79
<b>6</b>	<b>Calibration</b>	<b>83</b>
6.1	DRS . . . . .	83
6.1.1	Voltage Calibration . . . . .	83
6.1.2	Time Calibration . . . . .	83
6.2	Drift Chamber . . . . .	84
6.2.1	z-coordinate Calibration . . . . .	84
6.2.2	Time Offset Calibration . . . . .	84
6.2.3	Time-to-Distance Calibration . . . . .	84
6.3	Timing Counter . . . . .	85
6.3.1	z-coordinate Calibration . . . . .	85
6.3.2	Inter-Bar Time Offset Calibration . . . . .	85
6.4	LXe Gamma-ray Detector . . . . .	85
6.4.1	PMT calibration . . . . .	85
6.4.2	Non-Uniformity . . . . .	93
6.4.3	Energy Scale and Light yield . . . . .	94
<b>7</b>	<b>Performance</b>	<b>99</b>
7.1	Event Selection . . . . .	99
7.1.1	Photon Cuts . . . . .	99
7.1.1.1	Fiducial Volume and Acceptance . . . . .	99
7.1.1.2	Pileup Rejection . . . . .	99
7.1.1.3	Cosmic Ray Veto . . . . .	100
7.1.2	Positron Cuts . . . . .	101
7.1.2.1	Fiducial Volume . . . . .	101
7.1.2.2	Drift Chamber Hit Pattern . . . . .	101
7.1.2.3	Quality of Track Fit . . . . .	102
7.1.2.4	Vertex Cut . . . . .	102
7.1.2.5	DCH-TIC Matching Cut . . . . .	102
7.1.2.6	Ghost Track Selection . . . . .	103

## CONTENTS

---

7.2	Gamma Energy . . . . .	103
7.3	Positron Energy . . . . .	107
7.4	Relative Angle . . . . .	107
7.4.1	Positron Emission Angle . . . . .	107
7.4.2	Muon Decay Vertex . . . . .	108
7.4.3	Gamma ray Position . . . . .	109
7.4.4	Combined Resolution . . . . .	110
7.5	Relative Timing . . . . .	110
7.5.1	Positron Time . . . . .	110
7.5.2	Gamma-ray Time . . . . .	110
7.5.3	Gamma-Positron Relative Time . . . . .	111
7.6	Efficiency . . . . .	113
7.6.1	Positron Detection Efficiency . . . . .	113
7.6.2	Gamma ray Efficiency . . . . .	113
7.7	Summary of Performance . . . . .	114
<b>8</b>	<b>Improvements for 2010 Data</b>	<b>115</b>
8.1	Alignment . . . . .	115
8.1.1	DC Alignment . . . . .	115
8.1.2	Relative Alignment Between DC and LXe . . . . .	116
8.1.3	Target Alignment . . . . .	118
8.2	Correlations . . . . .	119
8.3	Magnetic Field Map . . . . .	122
8.4	Likelihood Analysis . . . . .	123
8.5	Update on 2009 Result . . . . .	123
<b>9</b>	<b>Physics Analysis on Data 2010</b>	<b>129</b>
9.1	Overview of Analysis . . . . .	129
9.1.1	Data Set . . . . .	129
9.1.2	Pre-Selection . . . . .	130
9.1.3	Blinding . . . . .	130
9.1.4	Definition of Analysis Window . . . . .	131
9.2	Maximum Likelihood Analysis . . . . .	132
9.2.1	Definition . . . . .	132

9.3	Probability Density Functions . . . . .	135
9.3.1	Signal . . . . .	136
9.3.2	Radiative Muon Decay . . . . .	142
9.3.3	Accidental Background . . . . .	143
9.3.4	Confidence Interval . . . . .	151
9.4	Normalization . . . . .	152
9.5	Systematics . . . . .	153
9.6	Sensitivity . . . . .	155
9.6.1	Background Evaluation By Sideband Analysis . . . . .	155
9.6.2	Sensitivity . . . . .	161
9.7	Maximum Likelihood Fit on the Data . . . . .	163
9.7.1	Upper Limit on Branching Ratio . . . . .	164
9.7.2	Event Distribution . . . . .	166
9.8	Conclusion . . . . .	169
<b>10</b>	<b>Prospects</b>	<b>171</b>
	<b>Bibliography</b>	<b>173</b>

## CONTENTS

---

# List of Figures

1.1	Event distributions in the analysis region obtained by preliminary analysis of the 2009 data[1][2][3]. The contours show 1, 1.64 and $2\sigma$ regions of the signal PDF, which cover 39, 74 and 87% of probability, respectively. In the left plot, selections in $t_{e\gamma}$ and $\theta_{e\gamma}$ , each of which is 90% efficient on the signal, are applied. In the right plot, a selection in $E_e$ (90% on the signal) and a selection in $E_\gamma$ (73% on the signal) are applied. . . . .	2
2.1	Feynman diagram describing the $\mu \rightarrow e\gamma$ decay in the SM with a neutrino-mass extension. The internal fermion line is a neutrino mass eigenstate. By diagonalizing the neutrino propagator in flavor space, off-diagonal flavor couplings, $U_{\mu i}$ and $U_{ei}$ , are induced. . . . .	8
2.2	Predictions for $Br(\mu \rightarrow e\gamma)$ at various values of $\tan\beta$ as a function of the left-handed selectron mass for $M_R = 10^{13}$ GeV.[5] . . . . .	10
2.3	Predictions for $Br(\mu \rightarrow e\gamma)$ are shown as a function of the universal gaugino mass for two cases of $\tan\beta$ , scanning an LHC relevant space in the parameters describing the Planck scale masses. Both the PMNS case (green) and the CKM case (red) are explored. . . . .	12
2.4	Historical progress of $\mu^+ \rightarrow e^+\gamma$ search.[6] . . . . .	14
2.5	Schematics of $\mu^+ \rightarrow e^+\gamma$ event signature (a), and two types of backgrounds (b)(c) . . . . .	15
2.6	Positron energy spectrum of unpolarized $\mu^+ \rightarrow e^+\nu_e\nu_\mu$ decay (Michel spectrum). . . . .	17
2.7	Photon energy spectrum of unpolarized $\mu^+ \rightarrow e^+\nu_e\bar{\nu}_\mu\gamma$ decay. . . . .	18
3.1	Overview of the MEG experiment. . . . .	22

## LIST OF FIGURES

---

3.2	Layout of detectors in the MEG experiment. . . . .	22
3.3	Proton Accelerators at PSI. . . . .	24
3.4	590MeV ring cyclotron at PSI. . . . .	25
3.5	$\pi$ E5 beamline components. . . . .	25
3.6	Pion and muon beam intensity at $\pi$ E5. . . . .	26
3.7	Schematic view of MEG beam transport system. . . . .	26
3.8	Muon stopping target. . . . .	27
3.9	Mounting position of the target. . . . .	27
3.10	Photon reaction in liquid xenon. . . . .	29
3.11	Diagram of xenon phase[7]. . . . .	31
3.12	PMT for the LXe detector. . . . .	32
3.13	Schematic view of the liquid xenon detector. . . . .	33
3.14	Development view of the faces of liquid xenon detector. Each face is equipped with 216, 234, $144 \times 2$ and $54 \times 2$ PMTs for inner, outer, lateral and top or bottom. . . . .	34
3.15	Liquid xenon detector . . . . .	35
3.16	PMTs mounted inside the LXe detector. . . . .	35
3.17	Cryogenic system of the LXe detector. . . . .	36
3.18	Liquid xenon tank and gaseous purification system. . . . .	37
3.19	Gas xenon storage tanks. . . . .	37
3.20	A photograph of COBRA magnet. . . . .	38
3.21	Comparison between COBRA spectrometer and uniform magnetic field. (a) and (c) show trajectories of positrons emitted transverse to the field. The uniform field makes many turns inside the detector, whereas the gradient field sweep the positron out of the detector much more quickly. (b) and (d) show trajectories of mono-energetic positrons emitted at various angles. In the uniform field, the bending radius depends on the emission angle, whereas it is independent in the gradient field. . . . .	39
3.22	Rate of Michel positrons per $cm^2$ per second as a function of radius assuming muon decay rate of $3 \times 10^7/sec$ . . . . .	40
3.23	Magnetic field ( $B_z$ ) along beam axis ( $x = y = 0$ ). . . . .	40
3.24	Map of COBRA magnetic field. . . . .	41

3.25 A photograph of the 16 drift chamber modules mounted on the support structure. . . . .	42
3.26 Drift chamber module. . . . .	43
3.27 Section of wires in two layers. . . . .	43
3.28 Schematic of vernier pattern on the cathode pads. . . . .	44
3.29 Field map and drift lines of drift chamber calculated by the GARFIELD simulation . . . . .	45
3.30 Picture of timing $\phi$ -counter. . . . .	47
3.31 Design of timing $\phi$ counter. . . . .	48
3.32 Timing z-counter and APDs. . . . .	49
3.33 Kinematics of the $\pi^0 \rightarrow \gamma\gamma$ decay. . . . .	50
3.34 Overview of the setup in $\pi^0$ run. . . . .	51
3.35 Liquid hydrogen target. . . . .	52
3.36 NaI detector. . . . .	52
3.37 CW accelerator. . . . .	53
3.38 Energy peaks in the LXe detector with CW accelerator. . . . .	54
3.39 Schematic of data flow and electronics. . . . .	55
3.40 Schematic of DAQ system. . . . .	56
3.41 Schematic of DRS principle. . . . .	57
3.42 Structure of MEG software. . . . .	58
4.1 Integrated muons during the MEG data taking in 2010. . . . .	62
4.2 Degradation system. . . . .	64
4.3 DRS4 board. . . . .	65
5.1 The six waveforms associated with a hit. The horizontal red lines are the calculated baselines, the vertical red lines are the leading edge time, and the region between the two dashed blue lines is the expected region where triggered signal appear. . . . .	68
5.2 $z$ reconstruction of the drift chamber hit. (a) shows the vernier circle. One turn corresponds to a period of vernier pattern (5 cm). (b) shows relation of the vernier phase with anode charge division. . . . .	70
5.3 Event display of positron tracking. Fitting is performed with Kalman filter. . . . .	71

## LIST OF FIGURES

---

5.4	Figure 5.10: An example of the waveforms used in the timing counter reconstruction. The black line is a DRS output, which is fitted to a template (red). The blue line is the NIM pulse output, which is fitted to another template (green). The time delay of the NIM pulse with respect to the DRS waveform is due to an electronic delay in the double threshold discriminator. . . . .	72
5.5	Typical waveform of a PMT in LXe detector. . . . .	74
5.6	A high-pass filtered waveform. . . . .	74
5.7	A saturated waveform. . . . .	75
5.8	Charge estimation with ToT. Pulse shape of template waveform is used to get the conversion factor from ToT to charge. . . . .	76
5.9	Correlation between $in, max$ and sum of inner PMT $N_{pho}$ for $w < 3$ cm. . . . .	79
5.10	Linearity plot of $E_\gamma$ vs $N_{sum}$ . The five points are given from 4.4 and 11.7 MeV from CW-B run, 17.6 MeV from CW-Li run, and 54.9 and 82.9 MeV from $\pi^0$ run. Red line is the best-fit linear function whose intercept is fixed to zero. . . . .	80
5.11	Distribution of normalized $\chi^2$ of the time fitting on data (dotted line) and signal MC without pileup (solid line). . . . .	81
5.12	Photon distribution before and after pileup elimination. . . . .	82
6.1	Inside view of LXe detector shows $^{241}\text{Am}$ source on wire and LED on the wall. Three LEDs with different attenuations are mounted on lateral faces. . . . .	86
6.2	Closeup of $^{241}\text{Am}$ source on wire. Diameter is $100\ \mu\text{m}$ and length is about 2 mm. . . . .	86
6.3	Gain calculation. . . . .	88
6.4	Gain shift of a worst PMT after beam blocker opened in upper figure and closed in lower. . . . .	89
6.5	Gain - HV curve and fit. . . . .	90
6.6	History of gain during MEG and $\pi^0$ run. . . . .	91
6.7	Reconstructed positions of alpha wires. . . . .	92
6.8	Comparison of alpha peaks between MC and data. . . . .	92
6.9	Stability of averaged QE. . . . .	93

**LIST OF FIGURES**

---

6.10 Non-uniformity correction on $u - v$ plane. . . . .	94
6.11 Non-uniformity correction on $u - v$ plane. . . . .	94
6.12 Cosmic ray peak. . . . .	95
6.13 Gamma ray peaks from AmBe sources. . . . .	96
6.14 Alpha peak of all sources. . . . .	97
6.15 Ni peak during beam time. . . . .	97
7.1 The accepted regions of the LXe detector are shown in red in the $u-v$ plane on the left and the $u-w$ plane on the right. . . . .	100
7.2 Distribution of the subtracted energy in the pileup elimination. Red filled entries are rejected by the selection criteria. . . . .	101
7.3 Cosmic ray cut. Black plot shows the events in the acceptance taken without beam. Red one shows MC signal events. Blue lines show the selection criteria. . . . .	102
7.4 Energy peak of 54.9MeV in $\pi^0$ run. . . . .	104
7.5 Energy resolution at 54.9 MeV on inner face ( $w \geq 2$ cm). . . . .	105
7.6 Energy Scale. . . . .	106
7.7 Fitting of a Michel spectrum. The dashed black line is the theoretical spectrum and the dashed blue line is the resolution function. The acceptance curve is shown in the bottom plot. . . . .	108
7.8 A fit to the distribution of energy difference between two turns. . . . .	109
7.9 Lead cubes and the support. . . . .	109
7.10 PMT grouping. Blue circles belong to the 'odd' group while orange circles belong to the 'even' group. . . . .	111
7.11 timing difference between LXe detector and reference counter . . . . .	112
7.12 Time difference between positron and gamma ray in 2010. . . . .	112
8.1 Definition of variables used in CR analysis. Blue lines are the reconstructed trajectory by DCH. . . . .	117
8.2 Trigger patches used in CW runs. . . . .	117
8.3 Target markers. . . . .	118
8.4 Position of the holes when misalignment happens. Dotted line shows the assumed target and solid line is the actual target. . . . .	119
8.5 Extraction of the $\delta\phi_e$ vs $\delta E$ and $\delta Y$ vs $\delta E$ correlations. . . . .	120

## LIST OF FIGURES

---

8.6	Extraction of the $\delta Z$ vs $\delta\phi_e$ and $\delta Z$ vs $\delta E$ correlations. . . . .	120
8.7	Illustration of the double turn track method. . . . .	121
8.8	Preliminary result of 2009 data before applying the improvements. (a)-(e) show the summed PDFs weighted with best fit values of each types. The blue lines are total sums of all PDFs. The green, red, and magenta lines show the signal, RD, and background PDF respectively. The black dots are the best fit values. (f) shows the contour plot on $N_{sig} - N_{RD}$ . The dashed, solid, and dotted lines show contours of the likelihood function at 1, 1.645, 2 sigma respectively[1][2][3]. . . . .	124
8.9	Event distributions in the analysis region.[2][1][3] The contours show 1, 1.64 and $2\sigma$ regions of the signal PDF, which cover 39, 74 and 87% of probability, respectively. In the left plot, selections in $t_{e\gamma}$ and $\theta_{e\gamma}$ , each of which is 90% efficient on the signal, are applied. In the right plot, a selection in $E_e$ (90% on the signal) and a selection in $E_\gamma$ (73% on the signal) are applied. . . . .	125
8.10	Updated result of sensitivity in 2009. . . . .	125
8.11	Updated result of 2009 data. The green, red, magenta and blue lines show the signal, RD, background and total sums of PDF respectively. . . . .	126
8.12	Updated event distributions in the analysis region for 2009 data. In the left plot, selections in $t_{e\gamma}$ and $\theta_{e\gamma}$ , each of which is 90% efficient on the signal, are applied ( $ t_{e\gamma}  < 0.278$ nsec, $ \theta_{e\gamma}  > 178.34^\circ$ ). In the right plot, a selection in $E_e$ (90% on the signal) and a selection in $E_\gamma$ (73% on the signal) are applied ( $51 < E_\gamma < 55$ MeV, $52.34 < E_e < 55$ MeV). . . . .	126
8.13	Confidence level curve in 2009 data. . . . .	127
9.1	The blind box, the analysis window, both timing sidebands, and the low gamma energy sideband are shown on the $(E_\gamma, t_{e\gamma})$ plane. . . . .	131
9.2	Probability density functions (PDFs) of each observable $(E_\gamma, E_e, \phi_{e\gamma}, \theta_{e\gamma}, t_{e\gamma})$ averaged over all events within the analysis region. The green, red and magenta lines show PDFs of signal, radiative muon decay and accidental background (S, R, B), respectively. . . . .	135

9.3	Residual energy distribution in $\pi^0$ due to opening angle resolution. The true energy is corrected by the energy-opening angle correlation to the kinematic edge using the reconstructed opening angle. (a) is for the 54.9 MeV side and (b) is for the 83.9 MeV side. . . . .	139
9.4	Divisions in $(u, v)$ for signal PDF extraction. Separate but same color regions are combined. . . . .	140
9.5	Examples of $\pi^0$ 54.9 MeV peak fit. Red lines are the best fit functions. Green and yellow bands show the confidence intervals of the function at 68% and 95% C.L. calculated with the covariance matrix evaluated in fitting. . . . .	141
9.6	BG distribution on $(\theta_{e\gamma}, \phi_{e\gamma})$ measured in time sidebands. The red box is the analysis region. . . . .	144
9.7	Position dependence of angular distribution for 2010 data. . . . .	144
9.8	BG $\theta_{e\gamma}$ distributions in $u_\gamma$ slices for 2010 data. The black line is the best fitted function. The green and yellow band show the 68% and 95% confidence intervals respectively. The red arrow shows the analysis region in the likelihood fit. . . . .	145
9.9	BG $\phi_{e\gamma}$ distributions in $v_\gamma$ slices for 2010 data. The black line is the best fitted function. The green and yellow band show the 68% and 95% confidence intervals respectively. The red arrow shows the analysis region in the likelihood fit. . . . .	146
9.10	Divisions in $(u, v)$ for background PDF extraction. . . . .	148
9.11	Examples of background fit for 2010 data. Black lines are the best fit functions and blue bands show the confidence intervals at 95% C. L. calculated with the covariance matrix. . . . .	149
9.12	Components of background. Data points show the $\gamma$ -ray background spectrum taken from the sideband physics data. Green line is the fitted spectrum from RMD and AIF. Blue line is the green line plus effects of pileup. Black line is the cosmic ray spectrum and the red line is the fitted result of all background. . . . .	150

## LIST OF FIGURES

---

9.13 Likelihood fit in positive time sideband. Summed PDFs weighted with best fit numbers of each types are superimposed on each plot. The green, red, magenta and blue lines show the signal, RD, background and total sums of PDF respectively. . . . .	158
9.14 Likelihood fit in negative time sideband. Summed PDFs weighted with best fit numbers of each types are superimposed on each plot. The green, red, magenta and blue lines show the signal, RD, background and total sums of PDF respectively. . . . .	158
9.15 Likelihood fit in angle sideband. Summed PDFs weighted with best fit numbers of each types are superimposed on each plot. The green, red, magenta and blue lines show the signal, RD, background and total sums of PDF respectively. . . . .	159
9.16 Likelihood fit in angle sideband. Summed PDFs weighted with best fit numbers of each types are superimposed on each plot. The green, red, magenta and blue lines show the signal, RD, background and total sums of PDF respectively. . . . .	159
9.17 Likelihood fit in angle sideband. Summed PDFs weighted with best fit numbers of each types are superimposed on each plot. The green, red, magenta and blue lines show the signal, RD, background and total sums of PDF respectively. . . . .	160
9.18 Likelihood fit in angle sideband. Summed PDFs weighted with best fit numbers of each types are superimposed on each plot. The green, red, magenta and blue lines show the signal, RD, background and total sums of PDF respectively. . . . .	160
9.19 Updated result of sensitivity in 2009. . . . .	161
9.20 Distribution of $N_{sig}$ upper limit at 90% confidence level in toy experiments for 2010 data. A median of this distribution (4.8) is defined as a 90% confidence sensitivity. . . . .	162
9.21 Distribution of $N_{sig}$ upper limit at 90% confidence level in toy experiments for combined data of 2009 and 2010. A median of this distribution (5.2) is defined as a 90% confidence sensitivity. . . . .	162
9.22 Updated result of 2009 data. The green, red, magenta and blue lines show the signal, RD, background and total sums of PDF respectively. .	163

9.23	Result of maximum likelihood fit for 2010 data. Summed PDFs weighted with best fit numbers of each types are superimposed on each plot. The green, red, magenta and blue lines show the signal, RD, background and total sums of PDF respectively. . . . .	164
9.24	Result of maximum likelihood fit for combined data of 2009 and 2010. Summed PDFs weighted with best fit numbers of each types are superimposed on each plot. The green, red, magenta and blue lines show the signal, RD, background and total sums of PDF respectively. . . . .	165
9.25	Confidence level curve for 2009, 2010 and combined data. . . . .	166
9.26	Updated event distributions in the analysis region for 2009 data. In the left plot, selections in $t_{e\gamma}$ and $\theta_{e\gamma}$ , each of which is 90% efficient on the signal, are applied ( $ t_{e\gamma}  < 0.278$ nsec, $ \theta_{e\gamma}  > 178.34^\circ$ ). In the right plot, a selection in $E_e$ (90% on the signal) and a selection in $E_\gamma$ (73% on the signal) are applied ( $51 < E_\gamma < 55$ MeV, $52.34 < E_e < 55$ MeV). . . . .	167
9.27	Event distribution in the analysis region for 2010 data. The signal 2D PDFs are superimposed as contours at 1, 1.64, 2 sigma as blue solid, dot-dashed, and dashed lines respectively. The number shows the rank by $S/(S + R + B)$ . In plot (a), selections in $t_{e\gamma}$ and $\theta_{e\gamma}$ , each of which is 90% efficient on the signal, are applied ( $ t_{e\gamma}  < 0.278$ nsec, $\cos \theta_{e\gamma}  < -0.9996$ ). In plot (b), a selection in $E_e$ (90% on the signal) and a selection in $E_\gamma$ (73% on the signal) are applied ( $51 < E_\gamma < 55$ MeV, $52.34 < E_e < 55$ MeV). . . . .	167
9.28	Event distribution in the analysis region for combined data of 2009 and 2010. The signal 2D PDFs are superimposed as contours at 1, 1.64, 2 sigma as blue solid, dot-dashed, and dashed lines respectively. The number shows the rank by $S/(S + R + B)$ . Events with rank (2,3,4) are from 2009, events with rank (1,5) are from 2010 data.. In plot (a), selections in $t_{e\gamma}$ and $\theta_{e\gamma}$ , each of which is 90% efficient on the signal, are applied ( $ t_{e\gamma}  < 0.278$ nsec, $\cos \theta_{e\gamma}  < -0.9996$ ). In plot (b), a selection in $E_e$ (90% on the signal) and a selection in $E_\gamma$ (73% on the signal) are applied ( $51 < E_\gamma < 55$ MeV, $52.34 < E_e < 55$ MeV). . . . .	168
10.1	Future prospects of sensitivity. . . . .	171

## LIST OF FIGURES

---

# List of Tables

2.1	Decay modes and branching ratios of muon. . . . .	6
3.1	Properties of LXe . . . . .	30
3.2	Properties of the PMT. . . . .	33
7.1	A table of inefficiencies for each cut. The inefficiencies are calculated as the fraction of events rejected by making only the cut with respect to making no cuts. The $\gamma$ acceptance cut inefficiency is calculated when positron cuts, pileup cut, and cosmic ray cut are already applied. . . . .	104
7.2	Performance in 2010. . . . .	114
8.1	Resolution in 2009. . . . .	123
8.2	Confidence intervals on 2009 data. . . . .	127
9.1	$E_e$ parameters. . . . .	137
9.2	Fit results of time response extraction from $E_\gamma$ -sideband. . . . .	138
9.3	Fractions of background components in the signal region. All the rest come from pileup or reconstruction tail. . . . .	150
9.4	Systematic uncertainties. . . . .	155
9.5	Best fit results of number of signal, radiative muon decay and background events. . . . .	156
9.6	Upper limits at 90% C.L. in number of signal events and branching ratio $\mathcal{B}$ . . . . .	156
9.7	Fit results in angle sidebands. . . . .	157
9.8	Confidence intervals on 2009 data. . . . .	165
9.9	Confidence intervals on 2010 data. . . . .	165

**LIST OF TABLES**

---

9.10 Confidence intervals on combined data of 2009 and 2010. . . . . 166

# 1

## Introduction

Although the Standard Model has been supported by essentially all the experimental results, it is thought to be a low energy approximation of a more fundamental theory of particle physics. New physics is thought to come in at a mass scale that has not been experimentally explored yet.

One way to explore new physics scenarios beyond the SM is to look for a lepton flavor violating decay. While lepton flavor symmetry is broken among neutral leptons by observations of neutrino oscillations, the process among the charged leptons, i.e. charged-lepton-flavor violation (cLFV) is considered to have too small rates to detect at present. Some models of new physics incorporating supersymmetry, however predict large branching ratios that are near the current experimental limits.

The MEG experiment is a  $\mu^+ \rightarrow e^+\gamma$  search aimed at either a discovery or improving the limit set by the MEGA experiment of  $Br(\mu^+ \rightarrow e^+\gamma) < 1.2 \times 10^{-11}$  (90% CL) [4] down to  $\mathcal{O}(10^{-13})$ . The MEG experiment achieves a higher sensitivity with relatively low accidental background using the world's most intense continuous muon beam at Paul Scherrer Institut (PSI), a positron spectrometer with a specially graded magnetic field, and an innovative 900 liter liquid xenon gamma-ray detector.

In 2009 we took data for two months and had a preliminary result of higher than expected upper limit with a few possible events in the signal region[1][2][3].

## 1. INTRODUCTION

---

The preliminary result of the maximum likelihood fit is

$$(N_{sig}, N_{RD}, N_{BG}) = (3.0^{+6.9}, 35_{-22}^{+24}, 332_{-36}^{+38}), N_{obs} = 370 \quad (1.1)$$

where the asymmetric errors are 1.645 sigma of MINOS errors obtained from MINUIT[8]. The negative error of  $N_{sig}$  is not written as it is outside of the defined fitting region.

The single event sensitivity in 2009 is estimated to be

$$S_{2009} = 6.1 \times 10^{-12} \quad (1.2)$$

The upper limit of branching ratio is

$$Br(\mu^+ \rightarrow e^+ \gamma) < 1.5 \times 10^{-11} \text{ at } 90\% \text{ C.L.} \quad (1.3)$$

The event distributions are shown in Figure 1.1. The events are labeled with the order of the likelihood ratio.

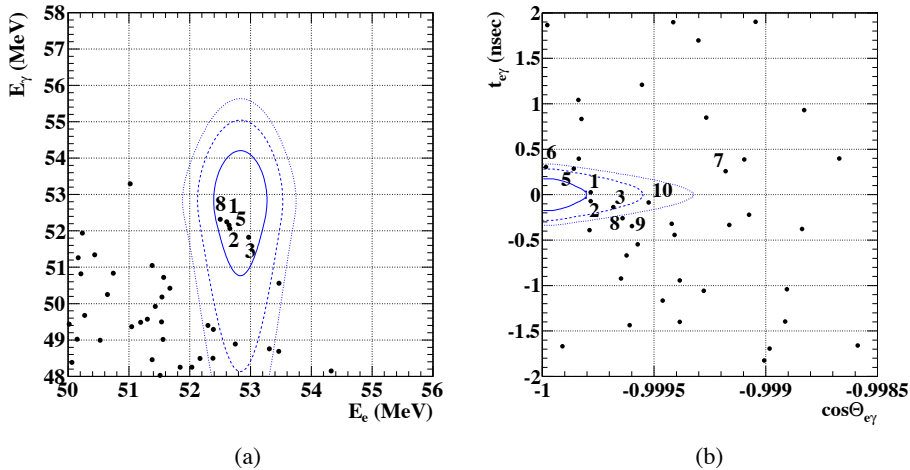


**Figure 1.1:** Event distributions in the analysis region obtained by preliminary analysis of the 2009 data[1][2][3]. The contours show 1, 1.64 and  $2\sigma$  regions of the signal PDF, which cover 39, 74 and 87% of probability, respectively. In the left plot, selections in  $t_{e\gamma}$  and  $\theta_{e\gamma}$ , each of which is 90% efficient on the signal, are applied. In the right plot, a selection in  $E_e$  (90% on the signal) and a selection in  $E_\gamma$  (73% on the signal) are applied.

---

In 2010, we took data for 67 days and observed  $1.1 \times 10^{14}$  muon decays. It correspond to twice more statistics than the 2009 data. In addition, we improved several aspects of calibration and analysis such as detector alignment, implementation of correlations in position observables, improved magnetic field map and improved likelihood analysis. In this thesis we analyze the 2009 and 2010 data with these improvements to examine the possible excess seen in the preliminary 2009 data analysis.

The theme of this thesis is a search for  $\mu^+ \rightarrow e^+\gamma$  using the MEG data taken in 2010. The analysis is structured as (a) standard analysis (b) improvements in 2010 (c) updated result of 2009 data (d) result of 2010 data (e) combined result of 2009 and 2010.

In Chapter 2, the standard model and SUSY-GUT theories are briefly introduced as well as the experimental searches for  $\mu^+ \rightarrow e^+\gamma$ . In Chapter 3, the experimental apparatus of MEG is described in detail. Methods for event reconstruction are described in Chapter 4. Calibration is discussed in Chapter 5. The performance of the detector is evaluated in Chapter 6. Aspects and conditions of runs in 2010 are given in Chapter 7 and the improvements made in 2010 are discussed in Chapter 8. The analysis to search for the  $\mu^+ \rightarrow e^+\gamma$  decay is described in Chapter 9 and the result is discussed. Future perspectives are discussed in Chapter 10.

## 1. INTRODUCTION

---

## 2

# $\mu \rightarrow e\gamma$ Decay

We discuss theoretical and experimental features of  $\mu \rightarrow e\gamma$  decay in this chapter. Firstly, the limits of Standard Model and various scenarios for new physics along with their predictions for  $Br(\mu \rightarrow e\gamma)$  are discussed. Then the history of  $\mu \rightarrow e\gamma$  search and its experimental features are summarized in the next section.

### 2.1 Theoretical Background

#### 2.1.1 Standard Model and Beyond

The behavior of fermions and gauge bosons are well described in the Standard Model (SM). Various features have been experimentally verified under TeV-scale energy. Nonetheless, it contains some fundamental and theoretical problems and is considered to be a low-energy approximation of a more fundamental theory.

The SM does not account for the existence of three generations of quarks and leptons. This problem is known as a flavor puzzle of the SM. The Standard Model also lacks a dark matter candidate.

Another problem of the SM is the hierarchy problem. It is related to the huge difference of energy scales between the weak scale of  $\mathcal{O}(100 \text{ GeV})$  and the reduced Planck scale of  $\mathcal{O}(10^{18} \text{ GeV})$ , where quantum gravitational effects become important.

## 2. $\mu \rightarrow E\gamma$ DECAY

---

Many extended models from SM have been proposed, such as supersymmetry and extra dimensions. One way to verify these models is through higher energy particle collision, while a search for rare mixings of lepton flavor, which is sensitive to many new physics models, provides another approach.

### 2.1.2 Muon Decay in the Standard Model

Muon is the second generation charged lepton that interacts through electromagnetic and weak interactions. It also couples to the Higgs boson. Muons decay through the charged-weak current interaction mediated by  $W_\mu^\pm$  gauge bosons. The decay modes and their branching ratios are summarized in Table 2.1. The dominant mode is Michel decay,  $\mu \rightarrow e\nu_\mu\bar{\nu}_e$ .

Decay mode	Branching ratio	Reference
$\mu^- \rightarrow e^- \nu_\mu \bar{\nu}_e$	$\sim 100\%$	
$\mu^- \rightarrow e^- \nu_\mu \bar{\nu}_e \gamma$	$(1.4 \pm 0.4)\%$	[9]
$\mu^- \rightarrow e^- \nu_\mu \bar{\nu}_e e^+ e^-$	$(3.4 \pm 0.4) \times 10^{-5}$	[10]
$\mu^- \rightarrow e^- \nu_e \bar{\nu}_\mu$	$< 1.2\%$	[11]
$\mu^- \rightarrow e^- \gamma$	$< 1.2 \times 10^{-11}$	[12]
$\mu^- \rightarrow e^- e^+ e^-$	$< 1.0 \times 10^{-12}$	[13]
$\mu^- \rightarrow e^- \gamma \gamma$	$< 7.2 \times 10^{-11}$	[14]

**Table 2.1:** Decay modes and branching ratios of muon.

### Neutrino Mass and Mixing

In the minimum standard model where neutrinos are massless, lepton flavor is conserved and occurrence of processes such as  $\mu \rightarrow e\gamma$  is prohibited. The observations of neutrino oscillations however indicate neutrino mass terms in the Lagrangian and physics beyond the SM.

If neutrinos are not massless, their mass matrix will be non-diagonal and complex just as the case for quark sector. The mass eigenstates are different from the flavor

eigenstates:

$$\nu_\alpha = \sum_i U_{\alpha i} \nu_i, \quad (2.1)$$

where  $\nu_\alpha = \nu_e, \nu_\mu, \nu_\tau$  are flavor eigenstates and  $\nu_i = \nu_1, \nu_2, \nu_3$  are mass eigenstates with masses  $m_1, m_2, m_3$ .  $U$  is a unitary matrix known as Pontecorvo-Maki-Nakagawa-Sakata (PMNS) matrix.

A neutrino of flavor  $\alpha$  at  $t = 0$  evolves after a time interval of  $t$  as

$$|\nu_\alpha(t)\rangle = \sum_i U_{\alpha i} e^{-iE_i t} |\nu_i(0)\rangle. \quad (2.2)$$

The probability of finding flavor  $\nu_\beta$  in  $\nu_\alpha$  beam at a distance  $x$  from the source is given by

$$P_{\nu_\alpha \rightarrow \nu_\beta} = \sum_i |U_{\alpha i}|^2 |U_{\beta i}|^2 + \sum_{i \neq j} U_{\alpha i} U_{\beta i}^* U_{\alpha j} U_{\beta j}^* \cos\left(\frac{2\pi x}{L_{ij}}\right), \quad (2.3)$$

where  $L_{ij} = 2\pi/(E_i - E_j) \simeq 4\pi p/|m_i^2 - m_j^2|$  is the oscillation length. For neutrino oscillation, non-zero neutrino masses and mixing angles are needed.

Neutrino mixing contributes to transition between charged leptons at the one-loop level as shown in Figure 2.1. However the LFV processes in charged lepton (cLFV) are severely suppressed because of the GIM mechanism. The branching ratio in the minimum extension of SM is given as

$$Br(\mu \rightarrow e\gamma) = \frac{3\alpha}{32\pi} \sum_i \left| U_{\mu i} U_{ei} \frac{\Delta m_{1i}^2}{m_W^2} \right|^2 < 10^{-54} \quad (2.4)$$

using the current measurements of the differences in the squared neutrino masses[15]:

$$|\Delta m_{32}^2| \approx 2.5 \times 10^{-3} eV^2 \quad (2.5)$$

$$\Delta m_{21}^2 \approx 7 \times 10^{-5} eV^2 \quad (2.6)$$

Thus an observation of  $\mu \rightarrow e\gamma$  would demonstrate the existence of new physics beyond the minimal extension of the Standard Model to include neutrino masses. The branching ratio in Eq 2.4 needs to be enhanced in order to be detected. In the

## 2. $\mu \rightarrow E\gamma$ DECAY

---

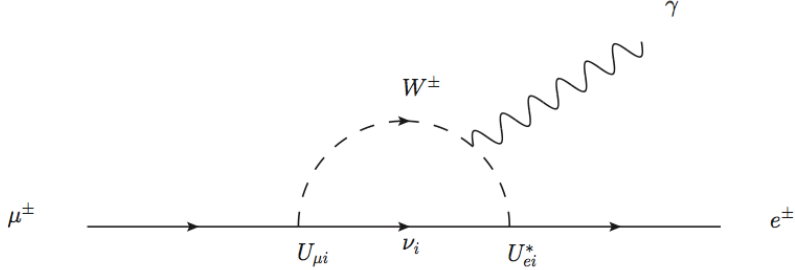


**Figure 2.1:** Feynman diagram describing the  $\mu \rightarrow e\gamma$  decay in the SM with a neutrino-mass extension. The internal fermion line is a neutrino mass eigenstate. By diagonalizing the neutrino propagator in flavor space, off-diagonal flavor couplings,  $U_{\mu i}$  and  $U_{ei}$ , are induced.

following section we review some examples of such a scenario.

### 2.1.3 SUSY and Lepton Flavor Violation

The mechanisms for generating neutrino masses have important consequences for lepton flavor violation.

The sector describing neutrino masses can be written as

$$\bar{\nu}^c M_\nu \bar{\nu} + h.c. = [\bar{\nu}_L \quad \bar{\nu}_R^c] \begin{bmatrix} m_L & m_D^T \\ m_D & M_R \end{bmatrix} \begin{bmatrix} \bar{\nu}_L^c \\ \bar{\nu}_R \end{bmatrix} + h.c. \quad (2.7)$$

If no new physics occurs below the Planck scale, neutrino masses  $m_{ij} \sim 10^{-5}$  eV are too small. With right-handed neutrinos, a Dirac mass term can be accommodated, yielding neutrino masses  $m_{ij}^D \sim Y_{ij}^\nu \langle \phi \rangle$ . If this is the sole source of neutrino mass, unnaturally small values of Yukawa couplings are required to reproduce experimental results.

Another way to explain the small neutrino masses is through seesaw mechanism[16]. If the left-handed Majorana mass is set to zero ( $m_L = 0$ ) and the Dirac mass is much smaller than the right-handed Majorana mass ( $m_D \ll M_R$ ), then Eq 2.7 gives neutrino masses as

$$m_N \simeq M_R, m_\nu \simeq \frac{m_D^2}{M_R} \quad (2.8)$$

$m_D$  is expected to be of the same order as the lepton masses, since they both arise through Yukawa terms. This requires right-handed neutrino masses in the range of  $10^6 - 10^{15}$  GeV[17] to get the right scale for the light neutrinos.

### SUSY

In the minimum SUSY extension of the SM (MSSM), LFV would originate from the misalignment between particle and superparticle mass eigenstates. Off-diagonal slepton mass terms would contribute to LFV. With no inherent guiding principles to limit the form of the soft breaking terms, it's unclear why  $\mu \rightarrow e\gamma$  does not take place at large rates. However, constraints from LFV and FCNC in quark sector suggest a small fermion-sfermion misalignment. This is known as the SUSY flavor problem[18].

A number of solutions have been proposed. In gauge mediation scenarios, for example, supersymmetry breaking is delivered to the visible sector by messenger fields charged under Standard Model gauge groups. The degree of flavor violation is tied to the scale of supersymmetry breaking; Other proposals involve postulating various flavor symmetries or kinematic suppression through heavy superpartner masses[19].

The following models focus on the gravity mediation scenario, in which the slepton mass matrix is taken to be diagonal and proportional to the unit matrix at the Planck scale,  $M_{Pl} \sim 10^{18}$  GeV.

### MSSM with Seesaw

Right-handed neutrinos can be incorporated into the MSSM through a superpotential for the leptons. If neutrino mixing is assumed to come entirely from Yukawa couplings, the information from neutrino oscillations can be related to the slepton mixing. Solar and atmospheric neutrino observations may be used to estimate typical values for  $Br(\mu \rightarrow e\gamma)$ , displayed in Figure 2.2[5].

## 2. $\mu \rightarrow E\gamma$ DECAY

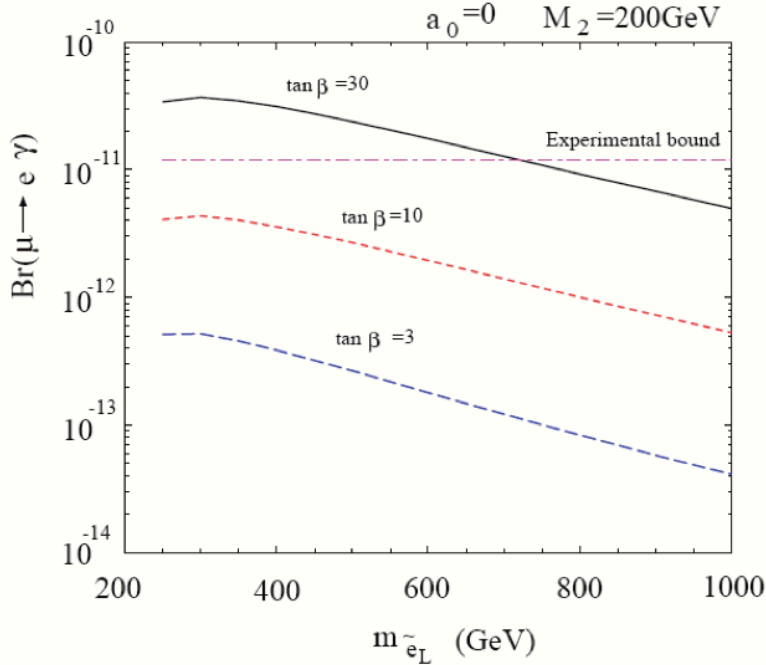


**Figure 2.2:** Predictions for  $Br(\mu \rightarrow e\gamma)$  at various values of  $\tan\beta$  as a function of the left-handed selectron mass for  $M_R = 10^{13}$  GeV.[5]

## SUSY-GUTS

Grand-unified theories (GUT) try to unify  $SU(2) \times U(1)$  electroweak interaction and  $SU(3)$  strong interaction in a single simple gauge group.

The simplest GUT model is the minimal  $SU(5)$  model. However it cannot unify the gauge couplings of the SM at the single scale and minimal  $SU(5)$  is ruled out by strong limits on proton decay from Super Kamiokande[20].

With right-handed neutrinos of singlet ( $SU(5)_{RN}$ ),  $SU(5)$  model gets a natural enhancement of the branching ratio due to the left-handed sleptons mass matrix.

$SO(10)$  gauge group on the other hand has a 16-dimensional representation, which can naturally accommodate all 15 fermions of a single generation (two quarks and two anti-quarks per family with three possible colors, a charged lepton and anti-lepton, and a left-handed Majorana neutrino that is its own anti-particle) as well

as a corresponding right-handed neutrino into a single multiplet. It can be extended in various ways to include a seesaw mechanism.

Most models work in either the CKM (Cabibbo-Kobayashi-Maskawa) case with small mixing in the neutrino Yukawa couplings or the PMNS (Pontecorvo-Maki-Nakagawa-Sakata) case with large mixing in the neutrino Yukawa couplings. The universal scalar mass  $m_0$ , trilinear couplings  $A_0$ , and universal gaugino mass  $M_{1/2}$  are free parameters that tie down the theory at the Planck scale. Other parameters include superpotential, an undetermined sign in the Higgs potential parameters, and  $\tan\beta$ . For a fixed  $\tan\beta$ ,  $Br(\mu \rightarrow e\gamma)$  can be predicted by scanning a range in the other parameters, as shown in Figure 2.3.[21]

### Summary

In general, cLFV could be induced in many extensions to the SM. While the predicted rate is highly model dependent, a discovery or stricter limit on  $\mu \rightarrow e\gamma$  would provide a guidance in narrowing down the allowed parameter space in each class of models, and valuable information for the new physics.

## 2. $\mu \rightarrow E\gamma$ DECAY

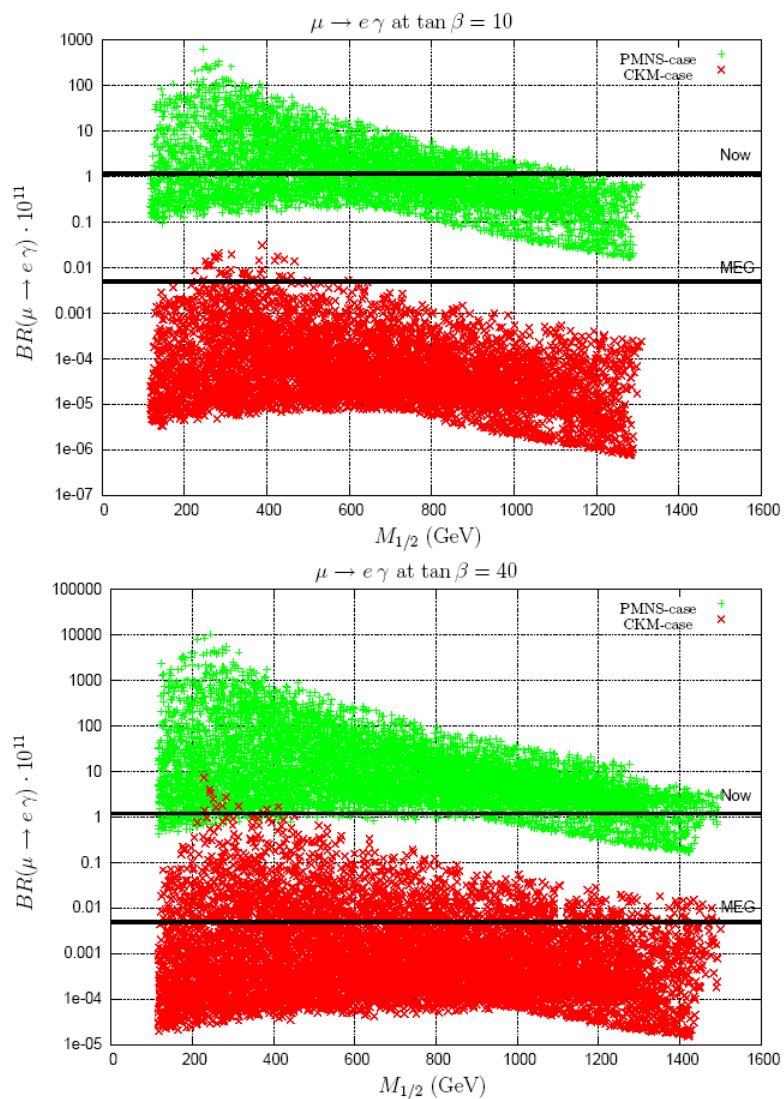


**Figure 2.3:** Predictions for  $Br(\mu \rightarrow e\gamma)$  are shown as a function of the universal gaugino mass for two cases of  $\tan\beta$ , scanning an LHC relevant space in the parameters describing the Planck scale masses. Both the PMNS case (green) and the CKM case (red) are explored.

## 2.2 Experimental Search

### 2.2.1 History of $\mu \rightarrow e\gamma$ Search

The muon was initially discovered by Anderson and Nedermeyer[22] in an experiment that measured the fractional energy loss of cosmic ray particles. At first it was thought to be the mediator of the force between protons and neutrons as predicted by Yukawa[23] on the basis of its mass. In 1947, however, it was shown through experiment[24] that the muon does not interact via the strong interaction, and thus the muon cannot be the  $\pi$  meson of Yukawa. The muon was thought to decay into a electron and a gamma ray if it is simply a heavy electron.

The first search for  $\mu^+ \rightarrow e^+\gamma$  was made in 1947 using cosmic-ray muons[25] and it gave an upper limit on the branching ratio of less than 10%. In 1955, an upper limit of  $B < 2 \times 10^{-5}$  was set using the Nevis cyclotron at the Columbia University[26].

In the late 1950s, it was pointed out that if the form of the 4-fermion interaction was, as a number of experiments supported, indeed a universal V-A one in which currents interacted with themselves through the exchange of a heavy charged boson, the predicted branching ratio for  $\mu^+ \rightarrow e^+\gamma$  was about  $10^{-4}$ [27], at odds with the current experimental limit. It was suggested that the apparent absence of  $\mu^+ \rightarrow e^+\gamma$  could be explained by associating separate lepton numbers for muons and electrons, and requiring them to both be conserved. In order to explain the abundantly observed  $\mu \rightarrow e\nu\nu$ , the outgoing neutrinos had to also carry muon ( $\mu_\nu$ ) and electron number ( $\nu_e$ ). Both the two-neutrino hypothesis and the separate conservation of lepton number were first confirmed in 1962 at Brookhaven[28].

With this discovery, interest in the search for neutrino-less decay modes of the muon waned and experiments essentially ended for about 15 years, until a new era of searches began in 1977 with an experiment making use of the intense muon beam at the Swiss Institute for Nuclear Research (SIN)[29], which is the site of present day PSI. More improvements in the limit followed. The best pre-MEG upper limit of  $1.2 \times 10^{-11}$  (90% CL) comes from MEGA experiment at the Los Alamos National Laboratory Meson Physics Facility (LAMPF)[30]. In an era where beyond the Standard Model physics is pervaded by numerous free parameters weakly constrained by experiments, the prospect for discovery or even a more stringent limit provides an alluring motivation to look for

## 2. $\mu \rightarrow E\gamma$ DECAY

---

$\mu \rightarrow e\gamma$ . A summary of the measurements of  $\text{BR}(\mu \rightarrow e\gamma)$  leading up to MEG is provided in Figure 2.4.

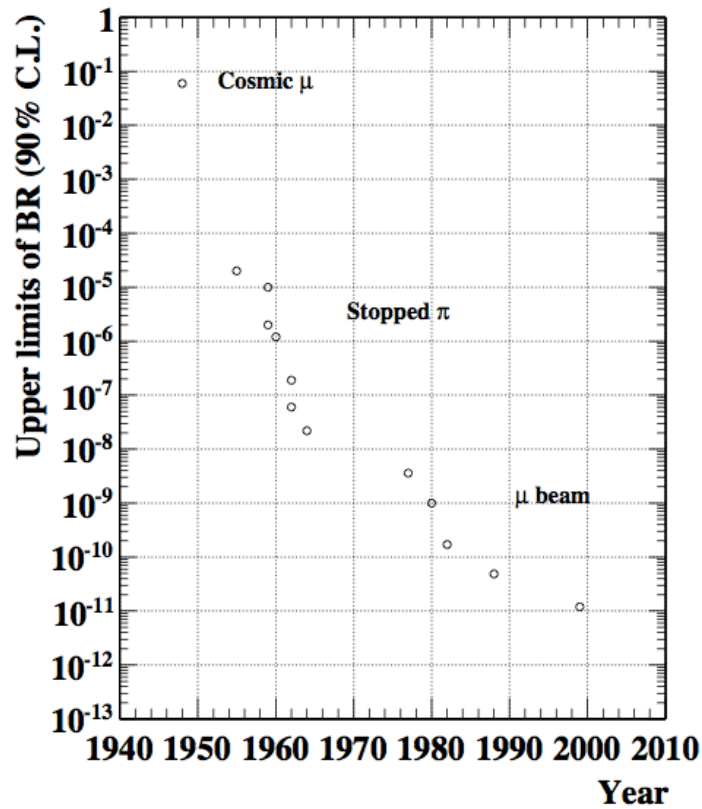
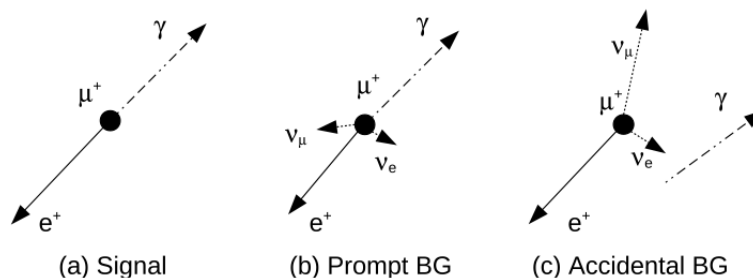


Figure 2.4: Historical progress of  $\mu^+ \rightarrow e^+\gamma$  search.[6]

2.2.2 Signal and backgrounds of  $\mu \rightarrow e\gamma$ 


**Figure 2.5:** Schematics of  $\mu^+ \rightarrow e^+\gamma$  event signature (a), and two types of backgrounds (b)(c) .

**Signal Event Signature**

In the muon rest frame, a  $\mu^+ \rightarrow e^+\gamma$  event is identified by a back-to-back positron and photon consistent with simultaneous emission from a common vertex, and with energies approximately equal to half the muon mass. Further, conservation of the energy-momentum 4-vector requires  $E_{e^+} = 52.83$  MeV and  $E_\gamma = 52.82$  MeV. Signal events are identified by measured positron energy ( $E_e$ ), photon energy ( $E_\gamma$ ), time( $t_{e\gamma}$ ), and opening angle ( $\Theta_{e\gamma}$ ).

**Prompt Background**

One source of background comes from radiative muon decay ( $\mu^+ \rightarrow e^+\nu_e\bar{\nu}_\mu\gamma$ ) with a nearly back to back positron and photon and two neutrinos that carry off little energy. The branching ratio for this process is suppressed in that region of phase space. For  $E_e > 46$  MeV,  $E_\gamma > 30$  MeV, and no constraint on the opening angle, the radiative decay branching fraction is of order  $10^{-7}$ [31].

The expected background can be calculated by integrating tree level differential decay width over a finite signal box. Let us take  $x \equiv 2E_e/m_\mu$ ,  $y \equiv 2E_\gamma/m_\mu$ , and  $z \equiv \pi - \Theta_{e\gamma}$ , and  $\delta x$ ,  $\delta y$ ,  $\delta z$  as the respective half-widths of a signal box centered at  $x = y = 1$  and  $z = 0$ , the expected branching ratio for unpolarized muons at the tree

## 2. $\mu \rightarrow E\gamma$ DECAY

---

level is[32]

$$d\mathcal{B}_{RD}(\mu^+ \rightarrow e^+\nu_e\bar{\nu}_\mu\gamma) = \frac{\alpha}{8\pi}[J_1 + J_2], \quad (2.9)$$

Where  $J_1$  and  $J_2$  are given by,

$$J_1 = \frac{8}{3}(\delta x)^3(\delta y)\left(\frac{\delta z}{2}\right)^2 - (\delta x)^2\left(\frac{\delta z}{2}\right)^4 + \frac{1}{3}\frac{1}{(\delta y)^2}\left(\frac{\delta z}{2}\right)^8 \quad (2.10)$$

$$J_2 = 8(\delta x)^2(\delta y)^2\left(\frac{\delta z}{2}\right)^2 - 8(\delta x)(\delta y)\left(\frac{\delta z}{2}\right)^4 + \frac{8}{3}\left(\frac{\delta z}{2}\right)^6 \quad (2.11)$$

when  $\delta z < 2\sqrt{\delta x\delta y}$ .

For energy resolutions of order 1%, a box analysis with high signal efficiency is subject to radiative decay background at the level of merely  $10^{-15}$  compared to the signal sensitivity goal of order  $10^{-13}$ .

### Accidental Background

Another source of background stems from accidental occurrences of a positron coming from Michel decay ( $\mu^+ \rightarrow e^+\nu_e\nu_\mu$ ) and a photon coming either from radiative muon decay, positron annihilation in flight (AIF) in the stopping target or materials in the drift chamber, or bremsstrahlung.

The effective branching ratio of the accidental background can be estimated by

$$\mathcal{B}_{acc} = R_\mu \cdot f_e^0 \cdot f_\gamma^0 \cdot \left(\frac{\delta\omega_{e\gamma}}{4\pi}\right) \cdot (2\delta t_{e\gamma}) \quad (2.12)$$

where  $R_\mu$  is the instant beam rate;  $\delta t_{e\gamma}$  is the half-width of signal box for time coincidence,  $\delta\omega_{e\gamma}$  is that for opening angle, and  $f_e^0$  and  $f_\gamma^0$  are fractions of the spectrum in Michel decay, and in gamma, respectively.

The positron spectrum (Michel decay) is shown in Figure 2.6.  $f_e^0$  can be estimated by integrating the Michel spectrum over  $1 - \delta x \leq x \leq 1$ . Since the spectrum is almost flat at  $x \approx 1$ , we can get  $f_e^0 \approx 2(\delta x)$ .

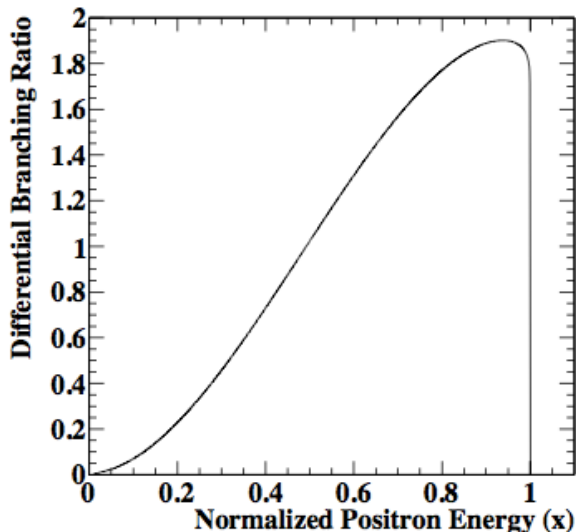


**Figure 2.6:** Positron energy spectrum of unpolarized  $\mu^+ \rightarrow e^+ \nu_e \bar{\nu}_\mu$  decay (Michel spectrum).

To estimate  $f_\gamma^0$ , the differential branching ratio of radiative decay is integrated over positron energy ( $x$ ) and the angle between positron and gamma ( $\Theta_{e\gamma}$ ). The photon spectrum is shown in Figure 2.7. By neglecting the terms suppressed by  $m_e/m_\mu$ , The partial branching ratio integrated over the signal region ( $1 - \delta y \leq y \leq 1 - r$ ) can be calculated as

$$f_\gamma^0 = \int_{1-\delta y}^{1-r} dy \frac{d\mathcal{B}_{RD}(\mu^+ \rightarrow e^+ \nu_e \bar{\nu}_\mu \gamma)}{dy} \approx \frac{\alpha}{2\pi} (\delta y)^2 [\ln(\delta y) + 7.33] \quad (2.13)$$

From the above, the effective branching ratio of accidental background is

$$\mathcal{B}_{acc} \approx R_\mu \cdot (2\delta x) \cdot \left[ \frac{\alpha}{2\pi} (\delta y)^2 (\ln(\delta y) + 7.33) \right] \cdot \frac{(\delta z)^4}{4} \cdot (2\delta t_{e\gamma}) \quad (2.14)$$

With the proposed beam rate and resolutions of MEG[33], the effective accidental background is estimated to be of the order  $10^{-14}$ .

## 2. $\mu \rightarrow E\gamma$ DECAY

---

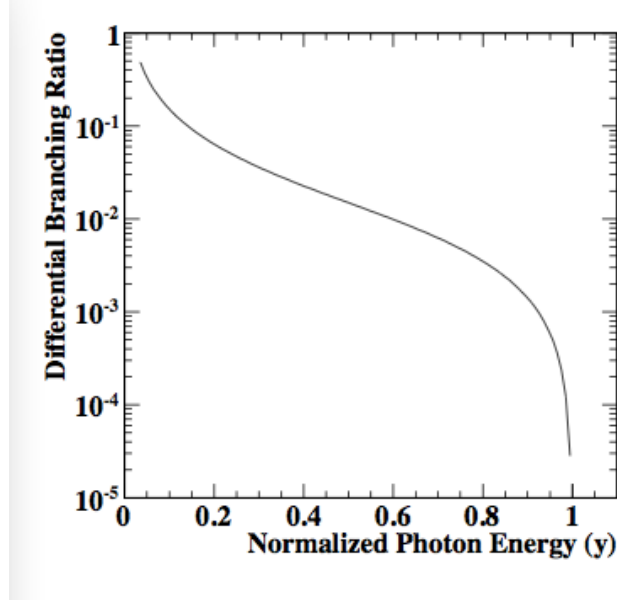


Figure 2.7: Photon energy spectrum of unpolarized  $\mu^+ \rightarrow e^+ \nu_e \bar{\nu}_\mu \gamma$  decay.

### 2.2.3 Requirements of $\mu \rightarrow e\gamma$ Search

As discussed above, accidental background is the dominant background source, and it will limit the experiment.

To search for  $\mu^+ \rightarrow e^+ \gamma$  we need a large number of muons. Since the accidental background is proportional to the intensity of muon beam, a direct current (DC) muon beam is the best in order to suppress backgrounds. MEG experiment uses the worlds most intense DC muon beam from 590 MeV proton ring cyclotron facility of 2 mA intensity at Paul Sherrer Institut (PSI) in Switzerland.

There is little background of gamma ray near the signal region. We can reduce background efficiently with a good gamma-ray energy resolution.

In contrast, there are many positrons in the signal region. Therefore it is difficult to reduce background by improving positron energy measurement. It is more important to efficiently measure a large amount of positrons generated by the high rate muon beam.

## 2.2 Experimental Search

---

In summary, in order to search for  $\mu^+ \rightarrow e^+\gamma$  at a high sensitivity, we need an intense DC  $\mu^+$  beam, a positron detector that can track high rate positrons, and detectors with good resolutions.

## 2. $\mu \rightarrow E\gamma$ DECAY

---

# 3

## MEG Experiment

The MEG experiment takes place at Paul Scherrer Institut (PSI) in Switzerland. In order to reduce background events, precise measurement of energy, emission angle and time of positron and gamma are very important. This chapter describes the hardware components, calibration apparatus, DAQ and analysis software of MEG experiment.

### 3.1 Detectors Overview

The detectors of MEG consist of positron detector and liquid xenon(LXe) gamma-ray detector, for the detection of positrons and photons from  $\mu^+ \rightarrow e^+ + \gamma$ , respectively, as shown in Figure 3.1.

#### Coordinate System

We define an orthogonal coordinate system by  $(x, y, z)$  as a global coordinate system (Figure 3.2). The origin is set as the center of COBRA magnet and also the center of the MEG target. The positive  $z$ -axis is defined to be parallel to the beam direction, pointing downstream. The  $y$ -axis points upwards so the  $x$ -axis is perpendicular to the face of the LXe detector, which is confined to  $x < 0$ . For particle emission angle,  $\theta$  is the zenith angle with respect to positive  $z$ -axis, so the beam direction is presented with  $\theta = 0$ , and  $\phi$  is an azimuthal angle made in the  $x - y$  plane with respect to the positive  $x$ -axis.

### 3. MEG EXPERIMENT

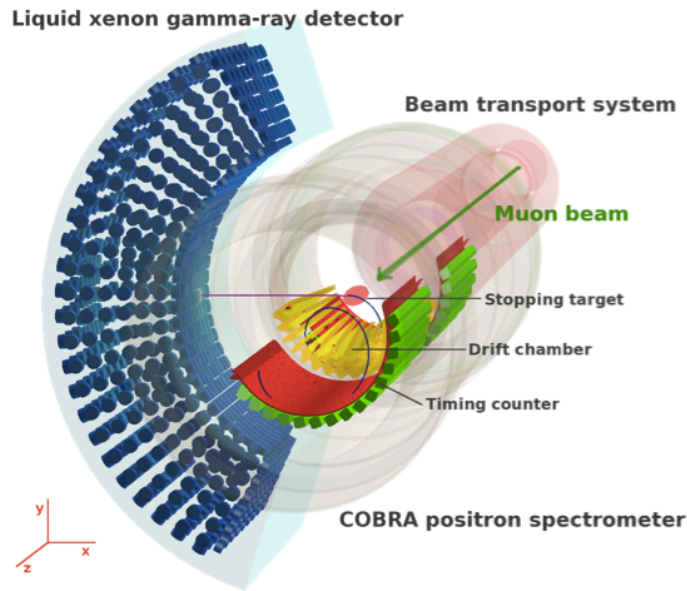


Figure 3.1: Overview of the MEG experiment.

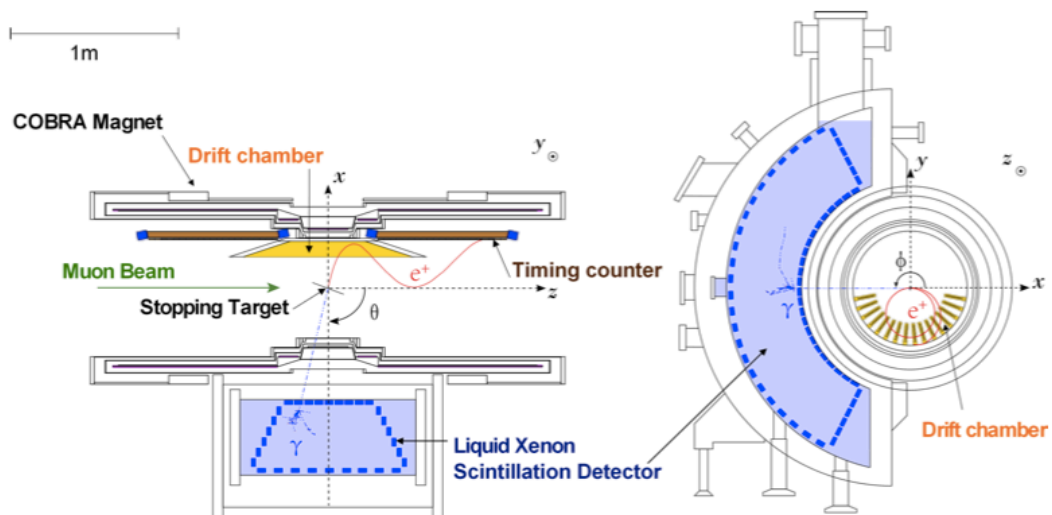


Figure 3.2: Layout of detectors in the MEG experiment.

## 3.2 Beam

In order to detect  $\mu^+ \rightarrow e^+ + \gamma$  with a great sensitivity, MEG experiment requires an extremely intense source of  $\mu^+/s$ . The  $\pi E5$  beam line at PSI has the most intense DC beam in the world with maximum intensity of  $10^8 \mu^+/s$ . A surface muon beam is produced from pion decays on the surface of the production target. MEG experiment uses a reduced beam intensity of  $3 \times 10^7 \mu^+/s$  to optimize the sensitivity of the experiment.

### 3.2.1 Proton Accelerators

The facility to provide protons consists of three accelerators (Figure 3.3). At first the Cockcroft-Walton accelerator injects 870 keV protons into Injector 2 cyclotron, which provides 72 MeV protons with 0.2% FWHM spread, and 50.63 MHz frequency. Then the Proton Ring Cyclotron (Figure 3.4) accelerates the 72MeV proton beam up to 590MeV energies to form a beam current of 2.2 mA. They are then directed through a series of meson production targets, one of which, dubbed target E, is a 4cm thick graphite target.

### 3.2.2 $\pi E5$

$\pi E5$ , one of the 5 beam lines sharing target E as a source, supplies low energy pions and muons. The  $\pi E5$  area has a suitable channel to obtain surface muons. Figure 3.5 shows the components of  $\pi E5$  beam line. The measured flux of pions and muons in E5 at the end of the last bending magnet (AST) is presented in Figure 3.6.

### 3.2.3 Beam Transport System

Figure 3.7 shows the beam transport system in the  $\pi E5$  area to bring the muon beam to stopping target. The muon beam is directed through two sets of quadrupole triplet magnets with a Wien filter in-between. The Wien filter applies perpendicular electric and magnetic fields, separating positive muons from positron contamination by  $7.5\sigma$ . Next, the beam is focused by a superconducting beam transport solenoid magnet (BTS). A momentum degrader at the center of the BTS is made of Mylar with a thickness

### 3. MEG EXPERIMENT

---

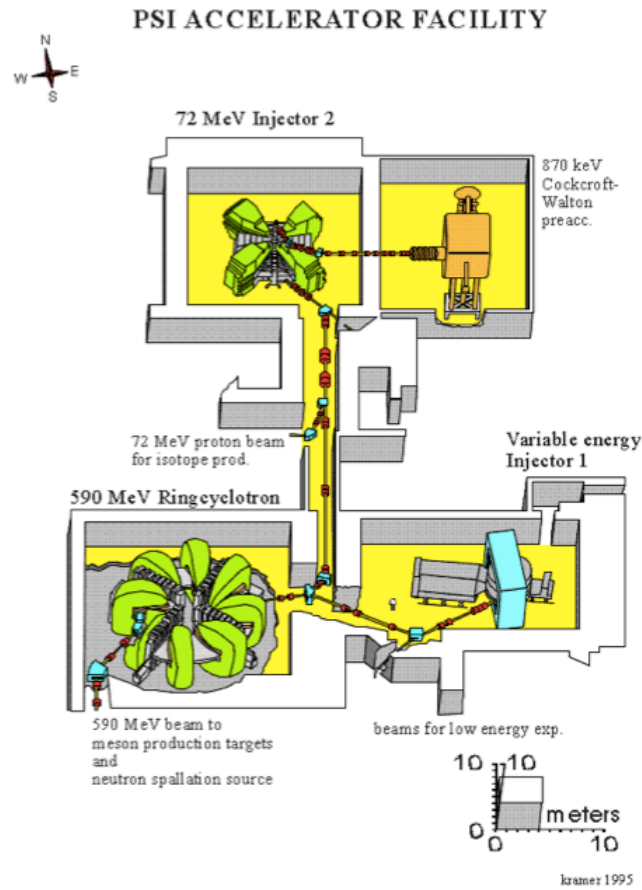


Figure 3.3: Proton Accelerators at PSI.

between 200 and 450 $\mu\text{m}$  which can be optimized to maximize stopping efficiency with less backgrounds. The final spot size on the stopping target is  $\sigma_x \approx 1\text{cm}$ ,  $\sigma_y \approx 1\text{cm}$ .

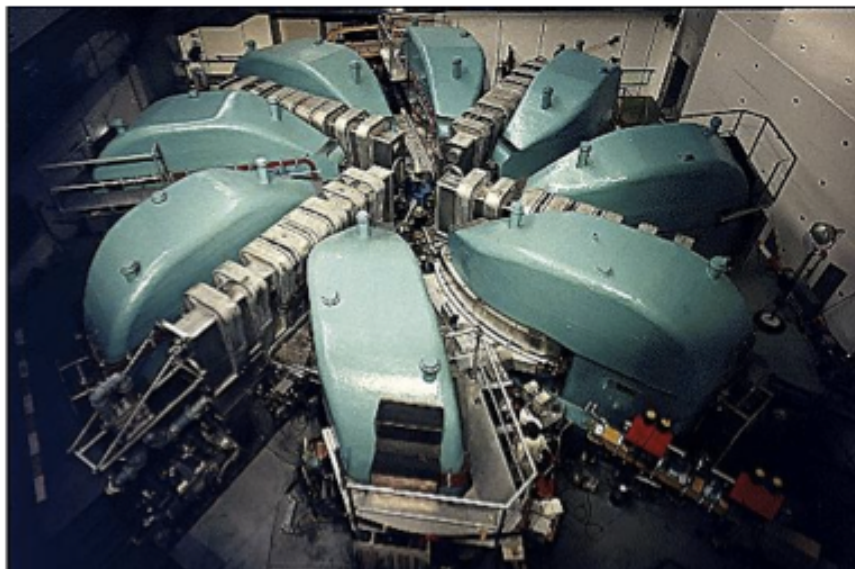


Figure 3.4: 590MeV ring cyclotron at PSI.

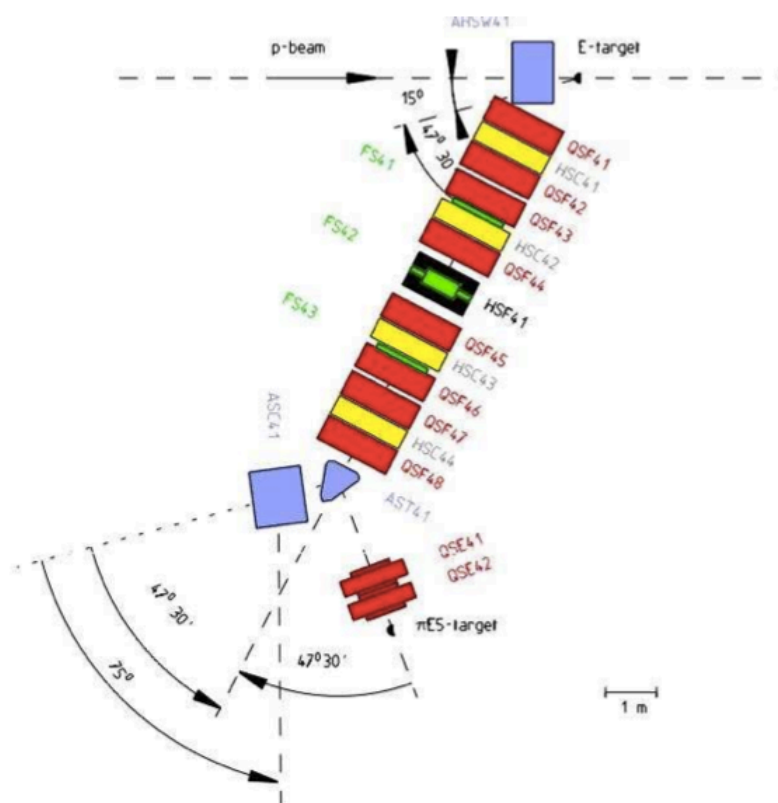


Figure 3.5:  $\pi E5$  beamline components.

### 3. MEG EXPERIMENT

---

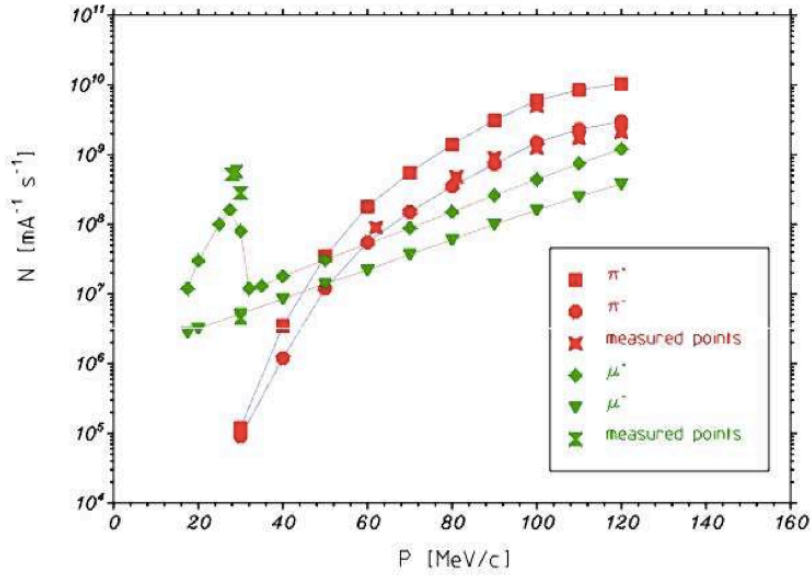


Figure 3.6: Pion and muon beam intensity at  $\pi$ E5.

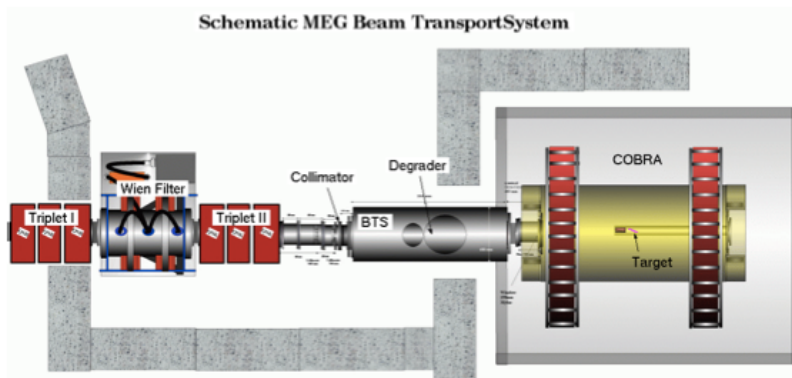


Figure 3.7: Schematic view of MEG beam transport system.

### 3.3 Stopping Target

The muon stopping target is an elliptical, polyethylene/polyester sandwich foil supported by a Rohacell frame[34] (Figure 3.8).

The target material and thickness are optimized to minimize scattering of positrons in the target and annihilation in flight. The dimension of the target is 79.8 mm along vertical axis and 200.5 mm along the long axis, with a thickness of  $205\mu\text{m}$ . It has six holes of 10 mm diameter to check its positioning using the vertex position reconstructed with the positron tracking.

The target is put at a slant angle of  $20.5^\circ$  in the middle of the COBRA magnet (Figure 3.9) to increase muon stopping power without significantly increasing the amount of target material typically traversed by exiting positrons.



**Figure 3.8:** Muon stopping target.

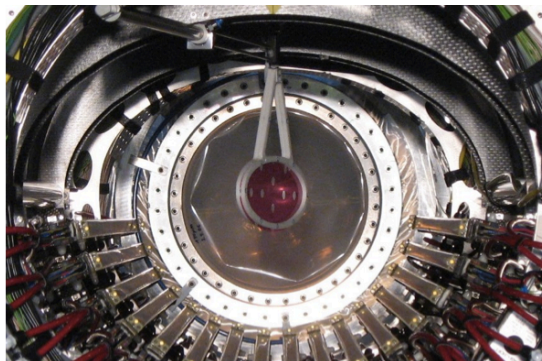


**Figure 3.9:** Mounting position of the target.

### 3. MEG EXPERIMENT

---

## 3.4 Liquid Xenon Gamma-ray Detector

### 3.4.1 Liquid Xenon

For MEG experiment, a liquid xenon detector of 900 liter volume is developed[35]. The characteristics of liquid xenon as scintillator has been studied for a long time, but rarely has it been used in such a great volume before due to the difficulties of handling. There are many advantages of using liquid xenon as a scintillator:

- High density 2.95 g/cm<sup>3</sup> and short radiation length  $X_0 = 2.77$  cm
- High light yield, 80% of NaI
- Fast response time of 45 ns for gamma rays
- No self absorption of scintillation light in liquid xenon
- Uniformity
- Particle discrimination

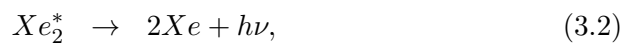
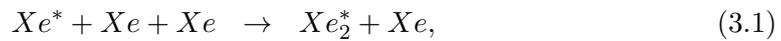
There are some difficulties such as cost, requirement of low temperature, high purity to avoid absorption of scintillation light, and detection of vacuum ultraviolet (VUV) scintillation light. These concerns were all solved in MEG LXe detector.

The properties of liquid xenon are summarized in Table 3.1.

### Mechanism of Scintillation Light

The origin of scintillation light from liquid xenon is de-excitation process of excited dimers of xenon,  $Xe_2^*$ . Figure 3.10 shows scintillation signals of liquid xenon by various particles.

There are two different processes[44] for the de-excitation. One is a self-trapping process of excited xenon atom,



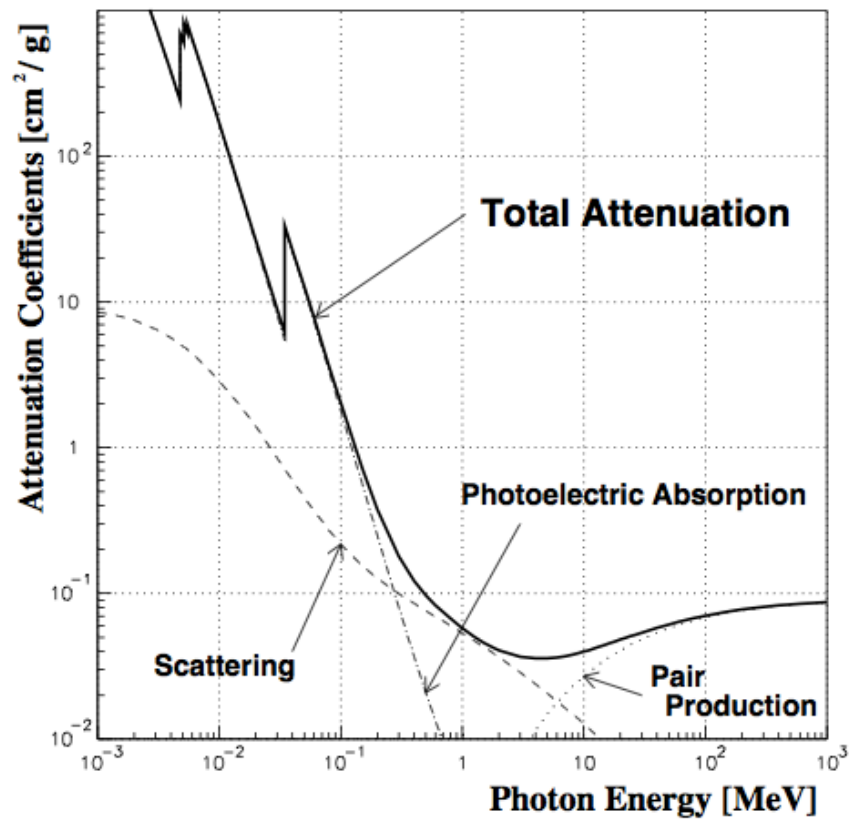


Figure 3.10: Photon reaction in liquid xenon.

### 3. MEG EXPERIMENT

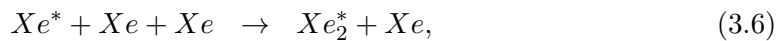
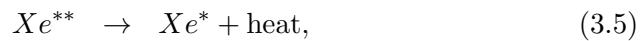
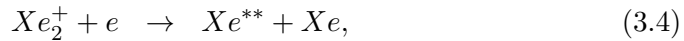
---

**Table 3.1:** Properties of LXe

Material Properties	Value	Ref
Atomic Number	54	
Atomic Weight	131.293	[15]
Density at 161.4K	2.978g/cm <sup>3</sup>	[36]
Boiling point	165.1K	[15]
Melting point	161.4K	[15]
Triple point (temperature)	161.3K	[37]
Triple point (pressure)	0.805 atm	[37]
Radiation length	2.77 cm	[15]
Critical Energy	14.5 MeV	[38]
Mollier radius	4.2cm	[38]
Scinti. wavelength (peak±FWHM)	(178 ± 14 nm)	[39]
Refractive index at 175nm	1.57 to 1.72	[40]
$W_{ph}$ for electron	21.6 eV	[41]
$W_{ph}$ for $\alpha$ particles	17.9 eV	[41]
Decay time (recombination)	45 ns	[42]
Decay time (fast components)	4.2 ns	[42]
Decay time (slow components)	22 ns	[42]
Absorption length	> 100 cm	[35]
Scattering length	29cm to 50 cm	[43]

where  $h\nu$  is vacuum ultraviolet (VUV) scintillation light. The two states of excited dimer  $Xe_2^*$ , singlet and triplet, correspond to fast and slow components respectively.

The other process is a recombination process originating from a xenon ion,



where the time dependence of the scintillation is dominated by the kinematics of

### 3.4 Liquid Xenon Gamma-ray Detector

---

the recombination process.

The wave length of the scintillation light emitted from both of these two processes are in the vacuum ultra-violet(VUV), which is  $178 \pm 14\text{nm}$  for peak and FWHM, and the decay time constant is relatively short, 45 nsec in the recombination process. The liquid state has the benefit of homogeneity. Figure 3.11 shows the diagram of xenon and liquid phase should be kept between 161 and 165 K at 1 atm.

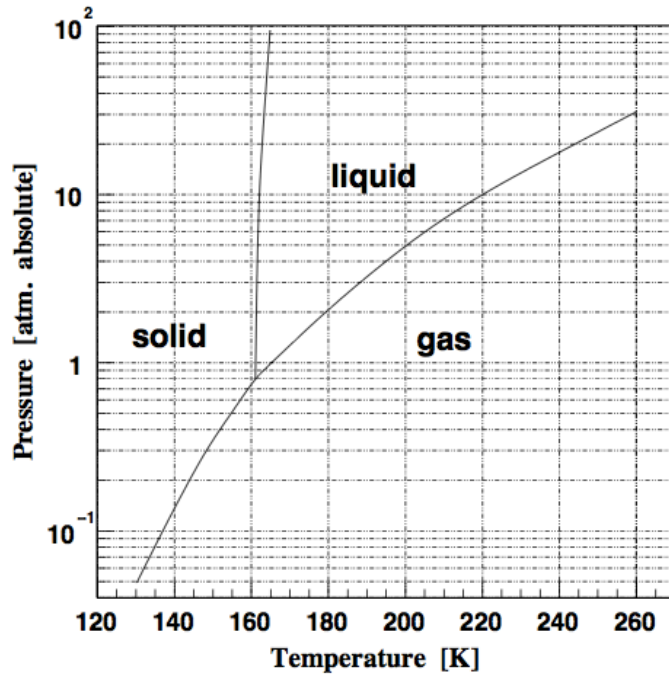


Figure 3.11: Diagram of xenon phase[7].

The impurities in the liquid xenon should be removed with a purification system to avoid absorption. There is no self absorption in xenon, but contaminations such as oxygen, nitrogen and water decrease a light yield of short-wavelength scintillation light. A purification system as well as a light yield monitor is needed for stable operation of the liquid xenon detector.

### 3. MEG EXPERIMENT

---

#### 3.4.2 Photomultiplier

We cooperated with Hamamatsu Photonics in developing UV-sensitive PMT R9869[45] (Figure 3.12). The photo-cathode material is K-Cs-Sb. This is designed so that it can observe scintillation light of liquid xenon directly while immersed in it.

For MEG experiment, the PMTs must work in low-temperature LXe and be sensitive to the VUV LXe scintillation light. The window of PMT is made of synthetic quartz with an 80% transparency around 178nm wavelength. We chose Bialkali (K-Cs-Sb) for the VUV sensitive photo-cathode. Aluminum strips are attached on the photo-cathode to avoid from the increase in the sheet resistance at a low temperature. The properties of the PMT are shown in Table 3.2.



**Figure 3.12:** PMT for the LXe detector.

#### 3.4.3 Design of LXe Detector

The schematic view of MEG LXe gamma-ray detector is shown in Figure 3.13. It is shaped to fit the outer radius of COBRA. The LXe detector has 900 liters of liquid xenon and 846 PMTs (Figure 3.15). The PMTs are placed on all six faces of the detector and are immersed in liquid xenon (Figure 3.16). Definition of six faces of the PMT holders (inner, outer, upstream, downstream, top, bottom) are shown in the Figure 3.13. PMTs are most closely arranged on the inner face and its coverage of active photo-cathode is about 35%. The arrangement and density of PMTs is shown in Figure 3.14. The active volume of the detector is 800 liters and it covers 11% of the



### 3. MEG EXPERIMENT

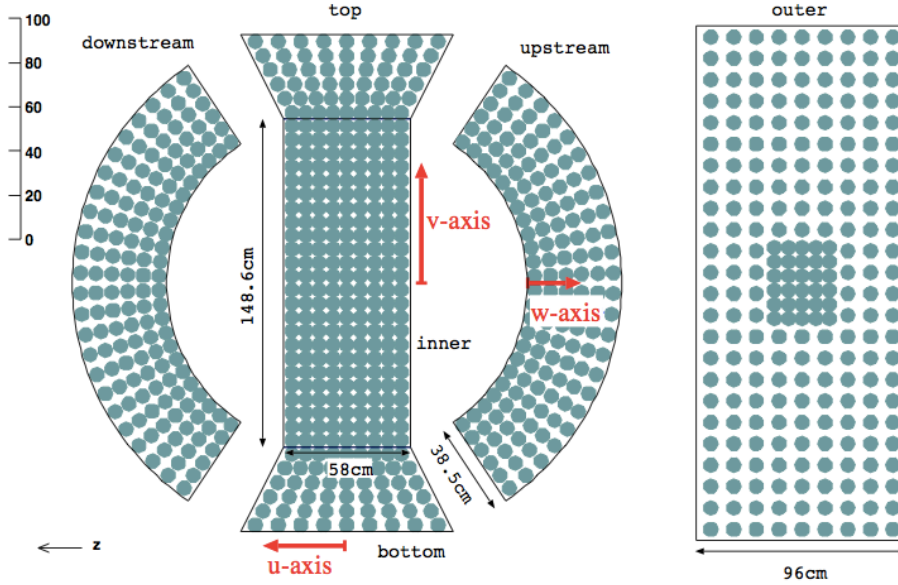


**Figure 3.14:** Development view of the faces of liquid xenon detector. Each face is equipped with 216, 234,  $144 \times 2$  and  $54 \times 2$  PMTs for inner, outer, lateral and top or bottom.

#### 3.4.4 Cryogenic System

A powerful and stable cryogenic system is needed for the operation of the LXe detector. LXe is filled in a cryostat consisting of two layers of vacuum-tight vessels. The outer layer makes a thermal insulation. The gamma-ray entrance window is designed to be as thin as possible to maximize light penetration. The window of the outer vessel is made of a 0.7 mm thick stainless steel plate, while that of the inner vessel is made of aluminum honeycomb panels covered with carbon fiber plates. The total thickness of the window is  $0.075 X_0$ . A turbo-molecular pump is directly attached to each vessel to evacuate with high conductance. In addition, a cryo-pump is installed to the inner vessel to efficiently remove water. A 200 W pulse-tube refrigerator[46], which was developed for this LXe detector, is mounted on top of the cryostat and controls the temperature of LXe. In addition, cooling pipes of  $LN_2$  are also available when necessary.

There are two storages for xenon outside the detector (Figure 3.17). One is a 1000-liter dewar (Figure 3.18) with a refrigerator to keep xenon as liquid. The other storage system consists eight high-pressure gas tanks (Figure 3.19).

### 3.4 Liquid Xenon Gamma-ray Detector

---



**Figure 3.15:** Liquid xenon detector



**Figure 3.16:** PMTs mounted inside the LXe detector.

### 3. MEG EXPERIMENT

---

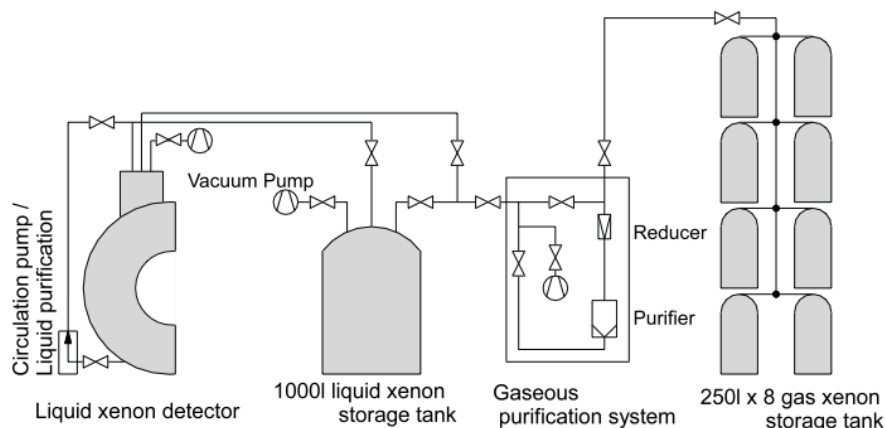


**Figure 3.17:** Cryogenic system of the LXe detector.

#### 3.4.5 Purification System

In order to purify xenon, two types of purification system[47] in liquid and gaseous phase were developed. The liquid purifier system has oxidization reduction filter made of copper and molecular sieves, which removes oxygen and water with 180 liter/h circulation by piston-type liquid pump. Another purification system in gas phase uses metal-heated getter to remove  $H_2O$ ,  $O_2$ ,  $CO$ ,  $CO_2$ ,  $N_2$ ,  $H_2$  and hydro-carbon molecules from gaseous xenon.

### 3.4 Liquid Xenon Gamma-ray Detector

---



**Figure 3.18:** Liquid xenon tank and gaseous purification system.



**Figure 3.19:** Gas xenon storage tanks.

### 3. MEG EXPERIMENT

---

## 3.5 Positron Spectrometer

The positron spectrometer consists of a magnet specially designed to form a gradient field, a drift chamber system to measure the positron track and scintillation counters to measure the positron timing.

### 3.5.1 COBRA Magnet

We constructed a superconducting magnet specially designed to form a highly graded magnetic field[48]. It consists of five coils with three different radii: one central coil, two gradient coils and two end coils. (Pictured in Figure 3.20). The magnetic field ranges from 1.27 T at  $z = 0$  to 0.49 T at  $|z| = 1.25$  m, as shown in Figure 3.23.



**Figure 3.20:** A photograph of COBRA magnet.

As shown in Figure 3.21, compared with a simple uniform solenoidal field, it has the following advantages:

- Positrons are swept away much more quickly, which contributes to the minimization of backgrounds.(Figure 3.22)

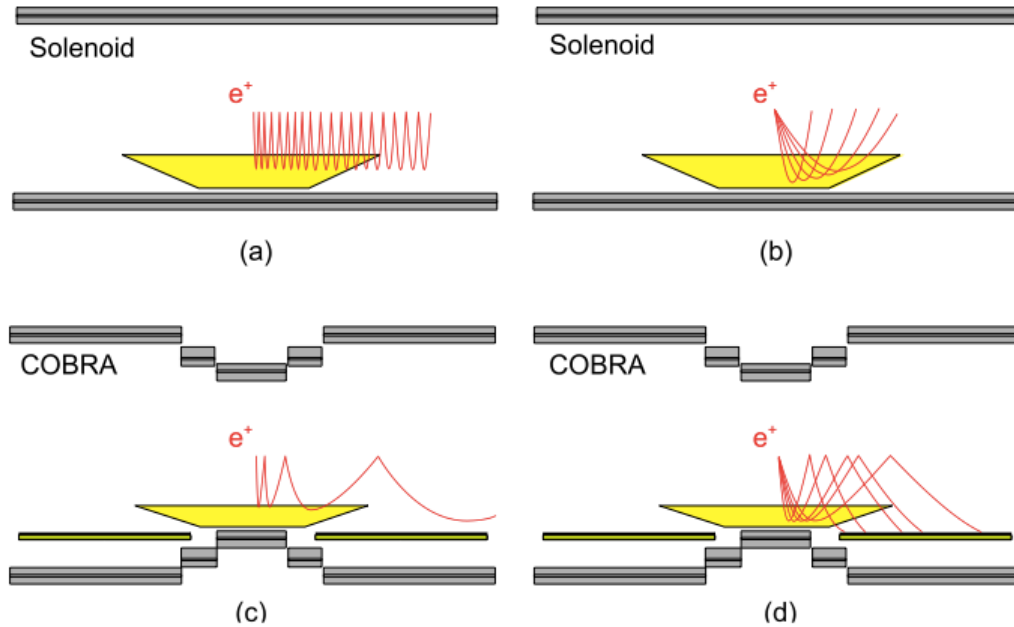


**Figure 3.21:** Comparison between COBRA spectrometer and uniform magnetic field. (a) and (c) show trajectories of positrons emitted transverse to the field. The uniform field makes many turns inside the detector, whereas the gradient field sweep the positron out of the detector much more quickly. (b) and (d) show trajectories of mono-energetic positrons emitted at various angles. In the uniform field, the bending radius depends on the emission angle, whereas it is independent in the gradient field.

- The positrons follow trajectories with a constant projected bending radius independent of the emission angle. This allows us to define the absolute momentum window of positrons to be detected.

Gamma rays must travel through the magnet structure before reaching the LXe detector and it causes signal inefficient when they interact with materials in front of the detector. Therefore the cable and wall of the magnet are made very thin. The total thickness of the superconducting coil, support structure, and cryostat amounts to  $0.197X_0$ .

### 3. MEG EXPERIMENT

---

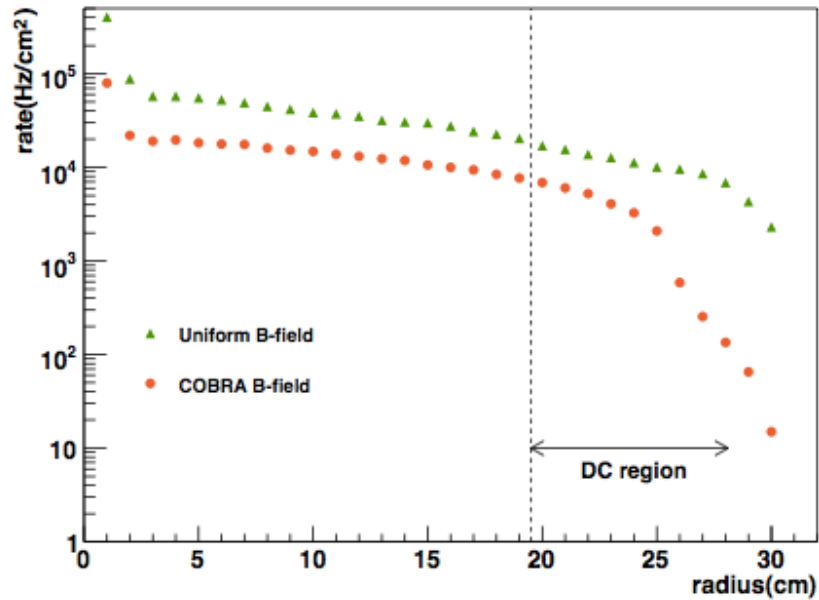


Figure 3.22: Rate of Michel positrons per  $cm^2$  per second as a function of radius assuming muon decay rate of  $3 \times 10^7/sec$ .

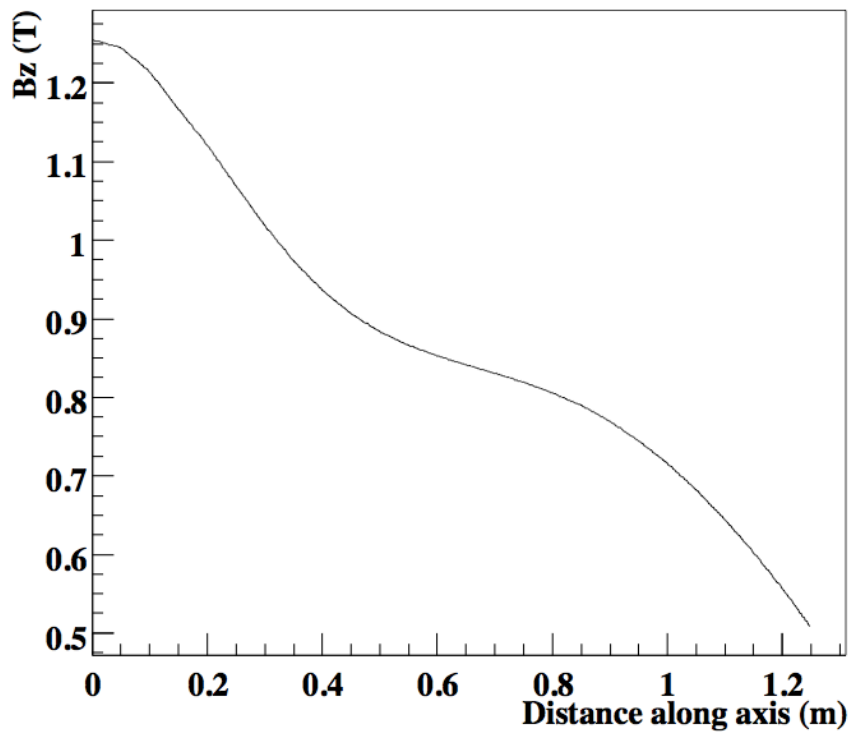


Figure 3.23: Magnetic field ( $B_z$ ) along beam axis ( $x = y = 0$ ).

### 3.5 Positron Spectrometer

The magnetic field produced by COBRA can deteriorate the performance of PMTs in the LXe detector. In order to reduce the fringe field at the position of the LXe detector, compensation coils are placed at both ends of the solenoid. With the compensation coils we successfully reduced the magnetic field at the position of the gamma-ray detector to 50 Gauss, as shown in Figure 3.24.

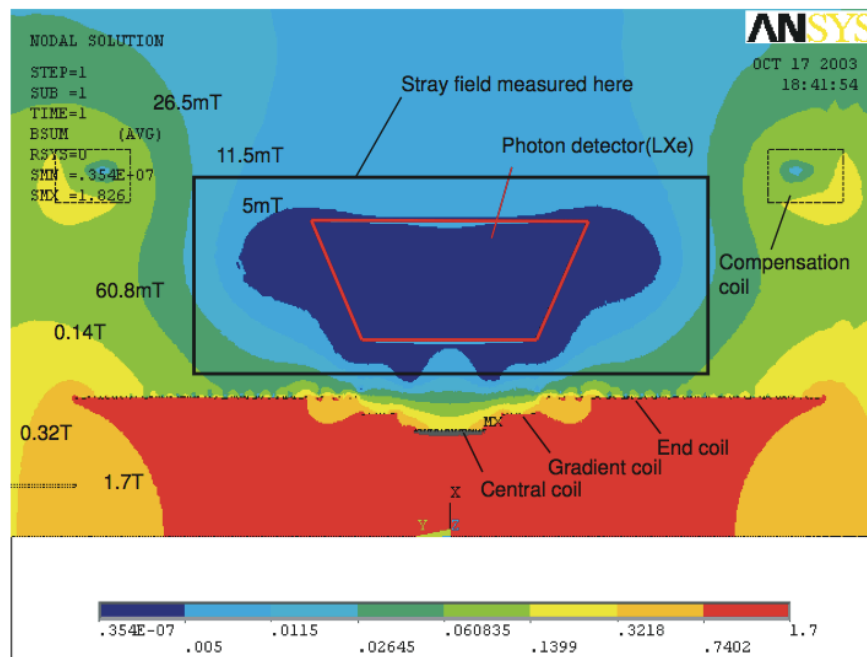


Figure 3.24: Map of COBRA magnetic field.

### 3. MEG EXPERIMENT

---

#### 3.5.2 Drift Chamber

The drift chamber (DCH) measures a momentum, a decay vertex and an emission angle of a positron. It consists of 16 chamber sectors aligned radially at  $10.5^\circ$  intervals in azimuthal angle. The radial position ranges from 19.3 to 27.9 cm to measure only high momentum positron ( $> 40$  MeV). Figure 3.25 shows a fully installed drift chamber system.

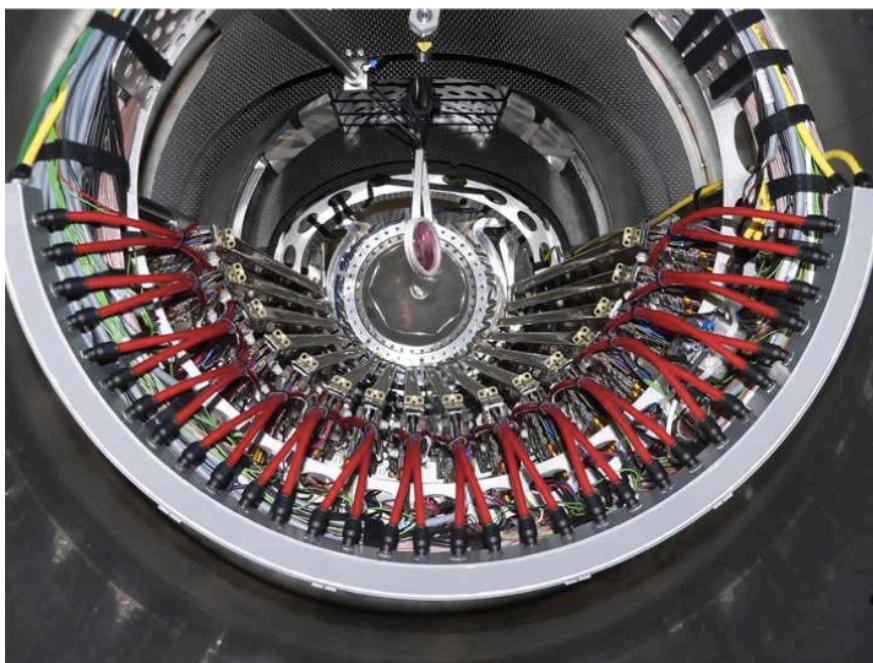


**Figure 3.25:** A photograph of the 16 drift chamber modules mounted on the support structure.

Each module of the chamber consists of a support frame, a foil with a cathode pattern and anode wires as shown in Figure 3.26, and is made up from 2 staggered arrays of drift cells which measure the time and r-coordinate of positrons simultaneously (Figure 3.27). Each layer containing nine drift cells is shifted by one-half cell each other to resolve left-right ambiguity. The two layers are separated by two inner cathode foils and also enclosed by a outer one.

The chamber walls are made of thin plastic foils. A thin layer of aluminum deposit on the four cathode foils is shaped to make a Vernier pattern, as shown in Figure 3.28.

The  $z$  position is first determined by the charge division on the anode wire at an accuracy of 1 cm, and later with more accuracy from the Vernier pads.

The chamber sectors and the volumes between them are filled with mixture of equal parts helium ( $\text{He}_2$ ) and ethane ( $\text{C}_2\text{H}_6$ ) by volume, which provides a substantial amount of ionization with little additional scattering[49]. A support frame made of carbon fiber supports the wires and foils. This structure helps to reduce amount of material in positron trajectories at a cost of a difficulty in the construction. The mean of total radiation length along the signal positron inside the tracking volume is  $2 \times 10^{-3} X_0$ .



**Figure 3.26:** Drift chamber module.

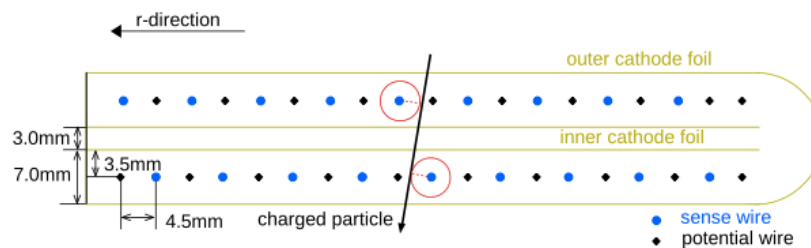


**Figure 3.27:** Section of wires in two layers.

A map of the field lines within a cell and the resulting arrival times are simulated by the GARFIELD[50] program. Figure 3.29 displays an example Garfield simulation.

### 3. MEG EXPERIMENT

---

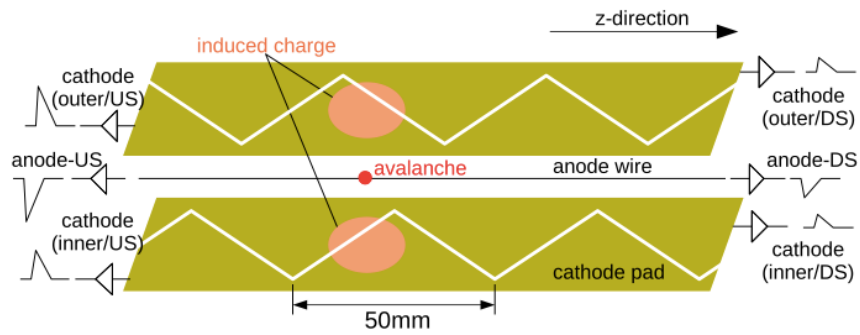
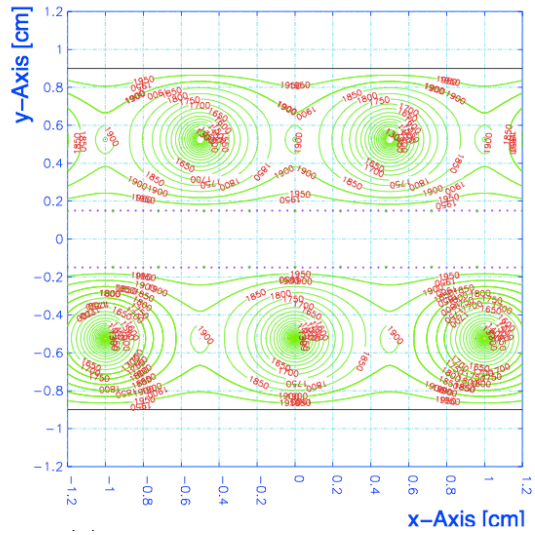
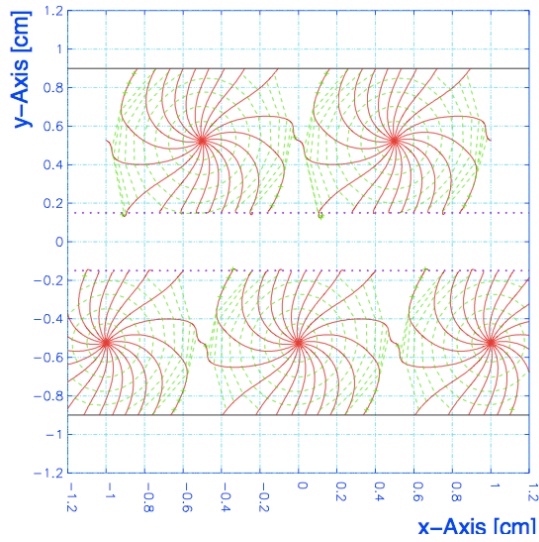


**Figure 3.28:** Schematic of vernier pattern on the cathode pads.



(a) Contour plot of the potential.



(b) Drift lines with isochrone map.

**Figure 3.29:** Field map and drift lines of drift chamber calculated by the GARFIELD simulation

## 3. MEG EXPERIMENT

---

### 3.5.3 Timing Counter

A pair of timing counters (TIC) are placed at the both sides of the drift chamber system. Each timing counter comprises two layers of plastic scintillators along  $z$  and  $\phi$  direction. The outer layer along  $z$  direction, called  $\phi$ -counter (TICP), gives the timing information and fast information of positron  $\phi$  emission angle. The inner layer along  $\phi$  direction, called  $z$ -counter (TICZ), gives precise measurement of  $z$  impact position and fast information of positron  $\theta$  emission angle.

The  $\phi$  counter consists of 15 straight plastic scintillator bars ( $4 \times 4 \times 80$  cm<sup>3</sup>, Bicron BC-404[51]) lying along  $z$  direction as shown in Figure 3.30. They are placed at  $10.5^\circ$  intervals in  $\phi$  direction at a radius of 32 cm and they cover  $-150^\circ < \phi < 10^\circ$ . Two 2-inch fine-mesh PMTs are attached to both ends of each bar. Details of the design is shown in Figure 3.31.

The  $z$  counter consists of 128 scintillating fibers ( $6 \times 6$  mm<sup>2</sup>, Saint-Gobain BCF-20[51]) put perpendicular to  $\phi$  counters as shown in Figure 3.32 . Each fiber is separated optically at the center and read out independently at the both ends by a  $5 \times 5$  mm<sup>2</sup> silicon avalanche photo-diode (APD)[45].



**Figure 3.30:** Picture of timing  $\phi$ -counter.

### 3. MEG EXPERIMENT

---

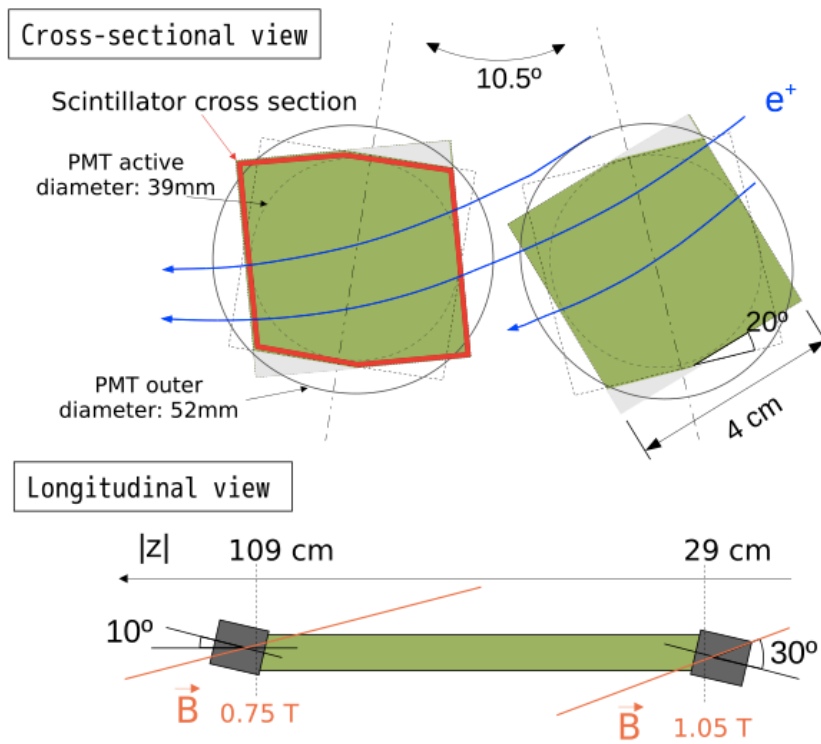


Figure 3.31: Design of timing  $\phi$  counter.

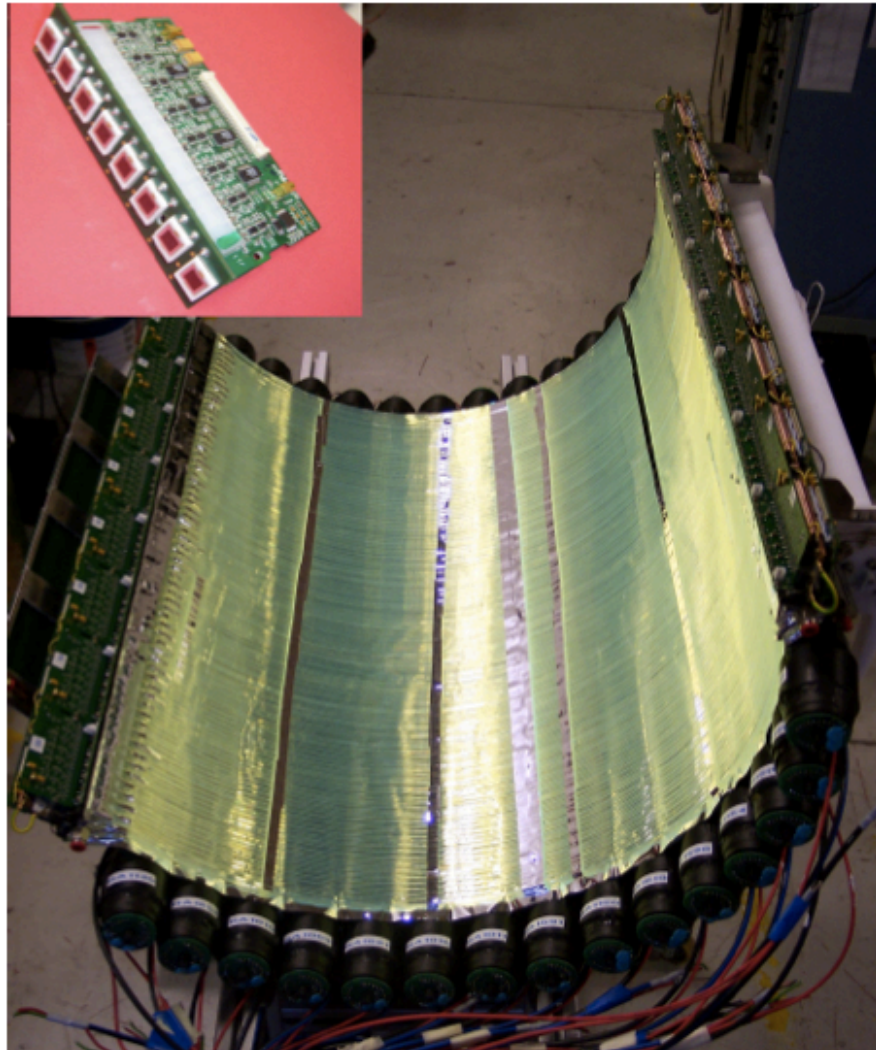


Figure 3.32: Timing z-counter and APDs.

## 3.6 Calibration Apparatus

Various apparatus are used to calibrate gamma energy scale; measure gamma energy, time and position resolutions. Back-to-back gamma pairs from  $\pi^0$  decay, as described in section 3.7.1, are used to calibrate the energy scale and measure the gamma energy, time resolutions, and efficiency. Light yield is monitored during data taking using monochromatic photons from reactions with Li and B, as described in section 3.7.2. Position resolution and relative timing between the LXe detector and timing counter are also checked from those reactions.

### 3.6.1 Setup For $\pi^0$ Run

The gamma ray near signal energy from  $\pi^0$  decay is used to calibrate the absolute energy scale. It is obtained by using the reaction  $\pi^- p \rightarrow \pi^0 n$  at rest followed by  $\pi^0 \rightarrow \gamma\gamma$  decay and selecting events where two gamma rays are in anti-parallel direction.

As shown in Figure 3.33, the  $\pi^0$  momentum is fixed at 28 MeV/c. When the photons are anti-parallel along the  $\pi^0$  flight direction, they have energies of 54.9 and 82.9 MeV. The 54.9 MeV gamma is close to the signal energy of 52.8 MeV and is used to determine energy scale and measure gamma resolution. In addition, a 129.4 MeV gamma from the radiative capture of negative pion ( $\pi^- n \rightarrow \gamma n$ ) is available. The Dalitz decay of neutral pion ( $\pi^0 \rightarrow \gamma e^+ e^-$ ) is also used to calibrate drift chamber.

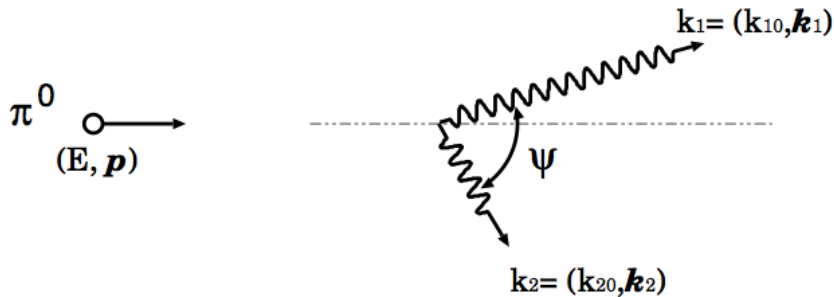


**Figure 3.33:** Kinematics of the  $\pi^0 \rightarrow \gamma\gamma$  decay.

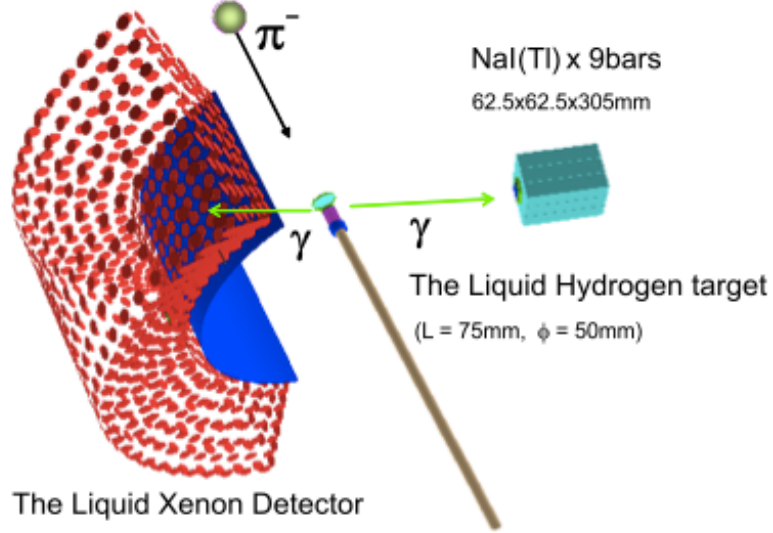


**Figure 3.34:** Overview of the setup in  $\pi^0$  run.

### Beam and Target Setup

The  $\pi E5$  channel provides a  $70.5 \text{ MeV}/c$   $\pi^-$  beam. During  $\pi^0$  run, the traditional muon target is replaced with a cylindrical target filled with about 150 cc of liquid hydrogen, pictured in Figure 3.35. It is 50 mm in diameter, and 75 mm in length. The window of the target cell is made of a thin  $135 \mu\text{m}$  Mylar film. The target is inserted from down stream side with a two meter long pipe. The setup of the  $\text{LH}_2$  target takes about three days, and the  $\pi^0$  run is usually only taken once a year.

### NaI Detector

To obtain monochromatic gamma rays from the back-to-back decays, another calorimeter is installed at opposite side of the LXe detector as pictured in Figure 3.36. It consists of nine crystals of NaI(Tl) scintillator with each coupled to an APD for energy measurement. To measure the time, a 5 mm-thick lead plate and two plastic scintillators are placed in front of the central NaI crystal. The  $e^+e^-$  pairs produced in the lead plate are collected by the two plastic scintillators. In order to scan the whole acceptance of the LXe detector, the NaI detector is mounted on a mover that can get

### 3. MEG EXPERIMENT

---

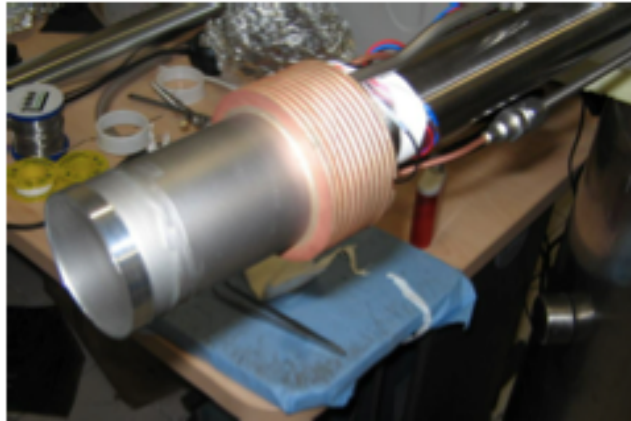


**Figure 3.35:** Liquid hydrogen target.

the same coverage of the LXe detector.



**Figure 3.36:** NaI detector.

### 3.6.2 Cockcroft-Walton Proton Accelerator

A Cockcroft-Walton (CW) proton accelerator (Figure 3.37) is installed at the downstream side of the MEG detector for the calibration of the LXe detector. Gamma rays in various targets are used to monitor the light yield of the LXe detector.

The normal target made of lithium tetraborate ( $\text{Li}_2\text{B}_4\text{O}_7$ ) provides reactions from lithium and boron. The peak at 17.7 MeV is obtained from  ${}^7_3\text{Li}(p, \gamma){}_4^8\text{Be}$  and can be used as a precise light yield monitor within 1%. CW calibration runs are taken twice a week to monitor the light yield of the LXe detector throughout the MEG data taking.

Another reaction  ${}^{11}_5\text{B}(p, \gamma){}_6^{12}\text{C}$ , with a resonance of 163 keV, produces a 16.1 MeV photon when the  ${}^{12}_6\text{C}$  is in ground state, or an 11.7 MeV photon when the  ${}^{12}_6\text{C}$  is in excited state, and a 4.4 MeV photon from the transition to the ground state. It allows the timing measurement between timing counter and the LXe detector, as well as the confirmation of the energy scale or the light yield monitor. Figure 3.38 shows the peaks in CW run.

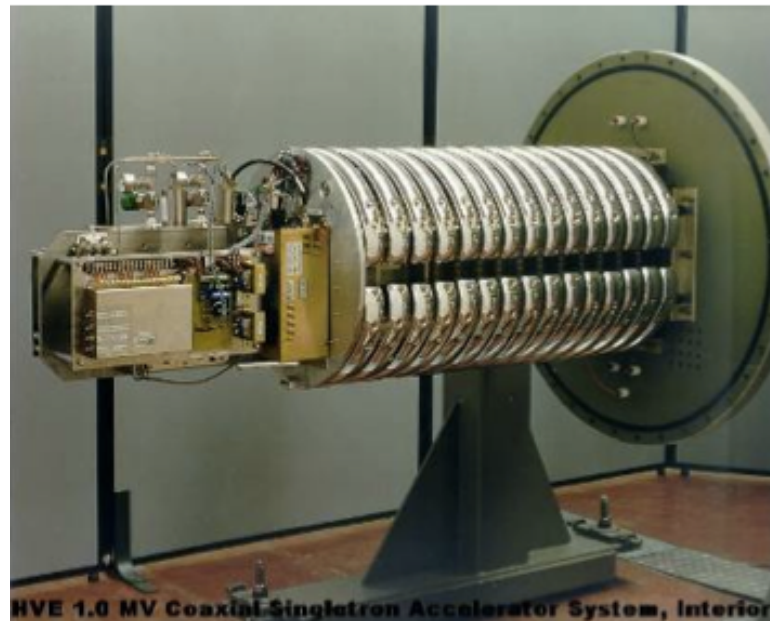


Figure 3.37: CW accelerator.

### 3. MEG EXPERIMENT

---

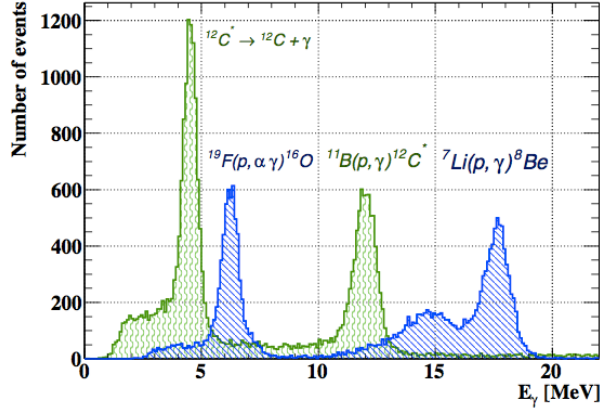


Figure 3.38: Energy peaks in the LXe detector with CW accelerator.

## 3.7 Electronics and Data Acquisition

### 3.7.1 Electronics Chain

The data flow from detectors to digitizers is schematically summarized in Figure 3.39. The outputs from detectors pass through several devices and finally acquired as waveform digitized by a fast waveform digitizer. Signals are also sent to a trigger system to decide whether the event is of interest or not, and those that fit the trigger criteria would be stored in software file.

PMT signals from the LXe detector are split into three outputs. One is a wide-band (1.9 GHz) fully differential output that goes to the waveform digitizer, the Domino Ring Sampler (DRS). The other outputs are a 320 MHz-bandwidth differential output, which is used for inner PMTs, and a four-to-one sum output that is used for the other PMTs. Both go to trigger through a 2 m-long low-density cable.

Signals from the timing counter bars are divided into three outputs in an 8:1:1 ratio. The largest output goes through a double threshold discriminator (DTD), to discriminate a positron hit from noise or low energy delta ray hits. The discriminator outputs 50 ns-wide standard NIM pulses that go to waveform digitizers. One of the smaller outputs is sent through another splitter where one output is coupled to the waveform digitizer and the other is coupled to the trigger system. The remaining 10% output is used for online current monitoring.

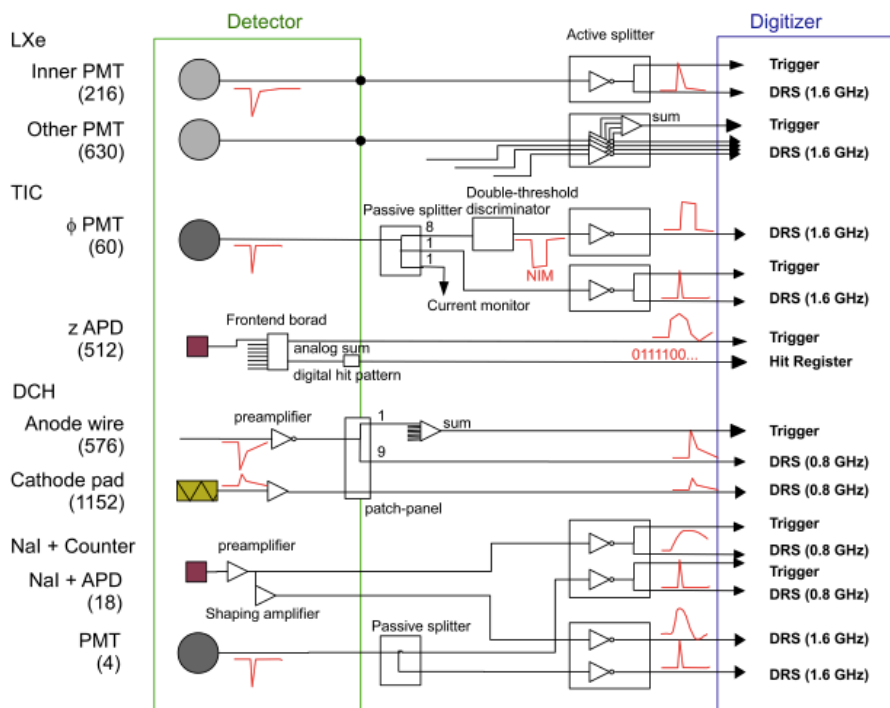


Figure 3.39: Schematic of data flow and electronics.

We get six waveforms for each cell of the drift chamber: two from the both ends of a anode wire and four from the vernier-pattern cathode pads. Signals from the anode wires are divided into ratio 9:1 with the largest output going to the waveform digitizer and the small output amplified then used in trigger. Signals from vernier pads are sent to waveform digitizers.

### 3.7.2 Data Acquisition System with MIDAS

An overview of the data acquisition (DAQ) system is shown in Figure 3.40. The MEG experiment uses MIDAS[52] (Maximum Integration Data Acquisition System) developed at PSI as a DAQ system. There are mainly nine frontend sub-systems: four for trigger and five for DRS. The MIDAS system provides the control of frontend processes as well as the logging system, the online database system for the parameters of DAQ and trigger, the slow control system, the alarm system, the history monitoring

### 3. MEG EXPERIMENT

system, and web interfaces.

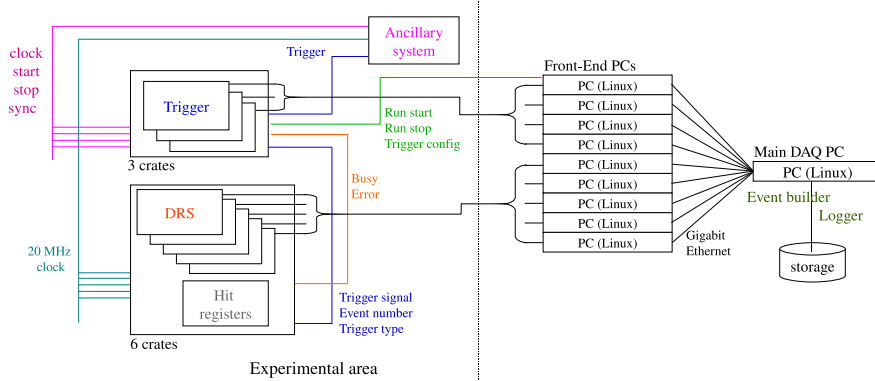


Figure 3.40: Schematic of DAQ system.

#### 3.7.3 Waveform Digitization with DRS

All waveform digitization in the MEG experiment is performed by a switched capacitor array called DRS (Domino Ring Sampler) developed at PSI[53, 54, 55]. A DRS chip has eight sampling channels, a channel to accept trigger signals, and a channel to accept a clock signal. Each of the eight sampling channels can store waveforms in a ring of 1024 capacitors. During operation, a sampling frequency is generated on a series of inverters and is running continuously in circular fashion (domino wave) until a trigger signal causes it to stop and the sampled waveform is read out by a shift register and digitized by a commercial FADC (fast analog-to-digital converter). This process is illustrated in Figure 3.41.

For the 2010 run, all detectors used version DRS4[55] with a sampling rate of 1.6 GHz, except for the timing counter, which used DRS3[54].

#### 3.7.4 Trigger System

The trigger system consists of flash analog to digital converters (FADC)[56], which digitize the waveforms received from the detectors, and field programmable gate arrays (FPGA)[57], which analyze the digitized waveforms.

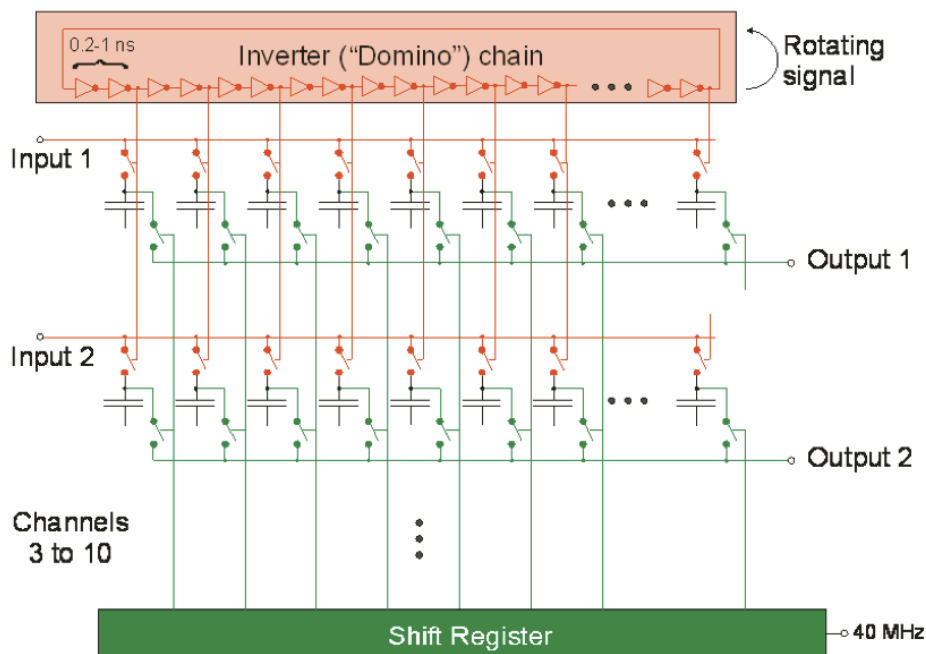


**Figure 3.41:** Schematic of DRS principle.

The whole system is arranged in a tree structure on three layers with two different types of boards. The first layer consists of the Type1 boards compliant with the 6U VME standard. The Type1 board receives and digitizes analog input signals with FADCs, implements some reconstruction algorithms on a large size FPGA, and sends the information to the successive trigger layer. The two remaining trigger layers consist of a second type of boards (Type2) compliant with the 9U VME standard. The second layer determines trigger conditions of sub-systems, and finally the third layer makes a trigger decision.

The trigger for  $\mu^+ \rightarrow e^+\gamma$  event (MEG trigger) is determined by three conditions: the gamma energy, positron-gamma time coincidence, and positron-gamma direction match. The online algorithm estimates the gamma energy by a global sum of PMT waveforms, and the threshold is set to 44 MeV. The online resolution is measured to be 8% in FWHM. The time coincidence is checked using the time difference between the PMTs from the gamma-ray detector and the timing  $\phi$ -counter. Both the positron and gamma emission times are taken from a linear interpolation of PMT pulse leading

### 3. MEG EXPERIMENT

---

edges. The resolution of the positron-gamma time difference is 3.3 ns ( $\sigma$ ), and the MEG trigger requires this to be within 10 ns of zero. The direction match is checked with the most illuminated inner face PMT. There is a correlation between the emission angle of a positron on the target and the hit position on the timing counter for the signal energy positron. This correlation is investigated using Monte Carlo simulation and a lookup table is formed in advance. The trigger rate for events that satisfy these three conditions was 6Hz.

#### 3.8 Simulation and Analysis

The MEG software is composed of three packages; MEGMC, MEGBartender, and MEGAnalyzer. The structure is shown in Figure 3.42. MEGMC and MEGBartender generate simulation data and MEGAnalyzer analyzes data from both experiment and simulation.

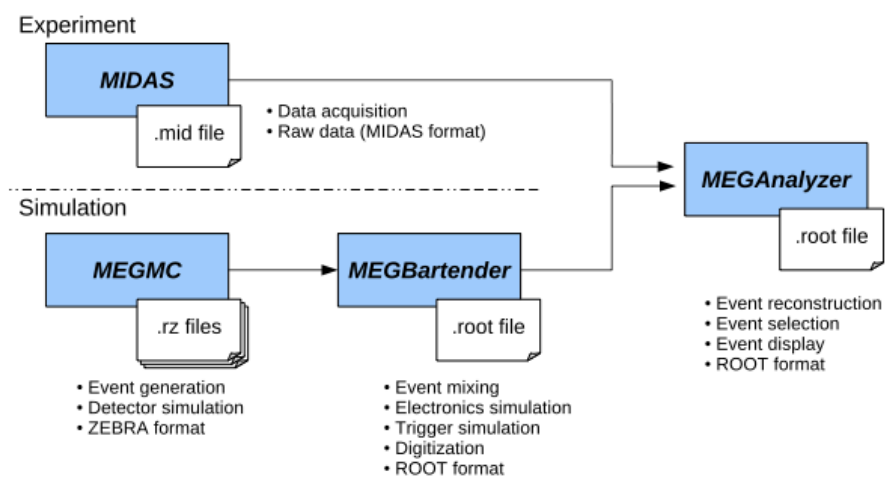


Figure 3.42: Structure of MEG software.

#### Event Generation and Detector Response

MEGMC is a GEANT3.21[58] based Monte Carlo simulation (MC). It processes the event generation and the detector simulation. The event can be generated for the

signal, Michel decay, radiative muon decay and separated positron or gamma ray of each decay as well as other backgrounds such as annihilation in flight of positron. Various calibration events are also simulated. Detector geometry and materials are implemented in the standard GEANT3 manner.

### Event Mixing and Electronics Simulation

After all event kinematics and response of the detector are simulated, the MEGBartender, can read multiple events generated by MEGMC and mix simulated events. Events are randomly or sequentially picked up from the input files and placed randomly in time according to the Poisson distribution.

Electronics simulation is also done by MEGBartender. To generate waveforms of the DCH and LXe detector, actual measured responses are used. The signal in timing counter is generated with digital filters in software and random fluctuations.

### Analysis Framework

We analyze all processes from raw data to physics analysis in MEGAnalyzer. It can handle both experimental and simulated data. Analysis and monitor framework in the MEG experiment base on the Root based Object oriented Midas Extension (ROME)[59] developed at PSI.

### 3. MEG EXPERIMENT

---

## 4

# Run 2010

MEG experiment was approved at Paul Scherrer Institut in 1999 and the construction and installation of detectors was finished at the end of 2007. In 2008 we took the first data for three months from September.

Before the physics run started in 2009, the waveform digitizer chip (DRS) was upgraded and light yield of liquid xenon scintillation light recovered. The physics data taking was performed for two months in 2009, 55% shorter than 2008, but with twice the data thanks to improved positron efficiency. Two setups of muon momentum degraders of  $200\mu$  m and  $300\mu$  m were used for the first and second half of the data taking.

In 2009, to shift the stopping distribution inside of target to the center, the thickness of the Mylar degrader was changed to  $200\mu$  m, but later reverted to  $300\mu$  m since it was found that the event distribution had a larger asymmetry along beam axis. The stopping efficiency of the muon target is estimated to be about 56% and 82% for  $200\mu$  m and  $300\mu$  m degrader, respectively. New version of DRS waveform digitizer was installed for the LXe detector and drift chamber. The new version has less effect of temperature drifts, a good linearity up to 1 Volt, no ghost pulses due to residual charge, better timing accuracy with 20 MHz global synchronization between boards and ability of faster sampling up to 6 GHz.

Before the 2010 run, we upgraded the waveform digitizer to improve timing resolution. There was some ambiguity in the alignment among the LXe detector, magnet,

## 4. RUN 2010

---

and target, therefore alignment measurement with cosmic rays was conducted. The physics data taking started in August and ended in November, more than one month earlier than scheduled, due to the BTS problem (see Section 4.5). Evolution of the number of muon stops on target is shown in Figure 4.1.

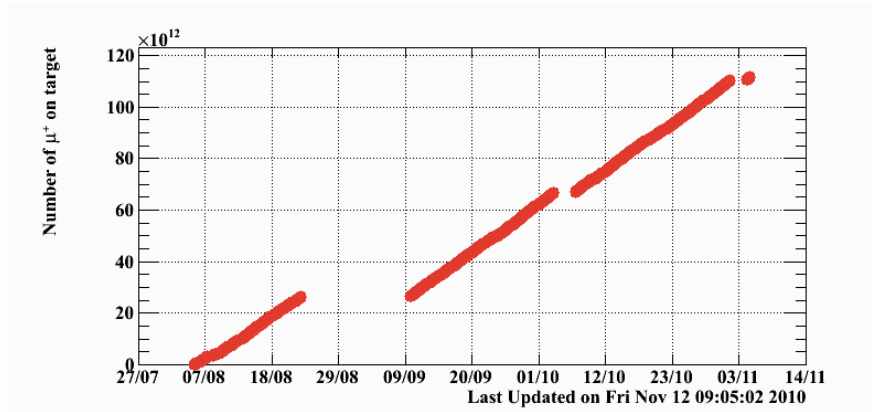


Figure 4.1: Integrated muons during the MEG data taking in 2010.

### 4.1 Physics Run

Muon stopping rate at proton current of 2.2 mA is  $3 \times 10^7 \mu^+ s^{-1}$ . Eleven types of trigger are mixed in the physics run. The total data taking time was 67 days. LED monitoring was performed everyday during data taking and full sets of calibration data including LED data with beam on and off, LED gain calibration, alpha and CW data were taken twice a week. 12169 runs were taken and in total 345 TB data was collected by November.

### 4.2 $\pi^0$ Run

We conducted a  $\pi^0$  run for 12 days in August. Details of  $\pi^0$  run setup are described in Section 3.6.1. We took several kinds of data in order to evaluate energy, time and position resolutions of the liquid xenon detector as well as calibrate energy scale.

$\pi^0 \rightarrow \gamma\gamma$  **patch scan** We did a full scan of the inner face with  $\pi^0 \rightarrow \gamma\gamma$  reaction in order to evaluate energy and time response. The inner face of the LXe detector was divided into 24 parts and trigger was prepared for each part. NaI was moved to the opposite of the patch to collect back-to-back events. Coincidence trigger between the LXe patch and reference counter was used for time performance and that between LXe patch and NaI was used for energy performance.

$\pi^0 \rightarrow \gamma\gamma$  **reference run** For reference we took data everyday at the same patch and the result is used to determine energy scale.

**Dalitz decay** We collected  $\pi^0$  Dalitz decay data for relative time measurement between the timing counter and the LXe detector.

## 4.3 Calibration Runs

The full set of calibration runs include LED data with beam on and off, LED gain calibration, alpha and CW data. They were taken three times a week. The details of calibration are described in Chapter 6.

## 4.4 Run Condition

The target was set at a similar slanting angle  $\beta$  as 2009 ( $\beta \approx 21^\circ$ ). The degrader was set to 300  $\mu\text{m}$  Mylar and in air doped at 5% He to ensure the stable operation of the drift chamber. Beam rate was set to  $3.7 \times 10^7 \mu^+ s^{-1}$  at the COBRA center which corresponds to a stopping rate of  $3 \times 10^7 \mu^+ s^{-1}$ .

### Degrader Optimization

The Mylar degrader (pictured at Figure 4.2) at the center of the BTS magnet has a thickness range of 200-400  $\mu\text{m}$ . It was changed from 200  $\mu\text{m}$  to 300  $\mu\text{m}$  during the 2009 run due to larger asymmetry in event distribution along the beam axis. A study on degrader optimization was carried out before the start of 2010 run in order to maximize the number of good positron tracks while minimizing backgrounds. In

## 4. RUN 2010

---

conclusion the thickness of the degrader was set to 300  $\mu\text{m}$ .



**Figure 4.2:** Degradation system.

### **The LXe detector**

Before the 2010 run, we did calibrations of liquid xenon detector to confirm light yield to be the same level as 2009. Bad channels of PMTs were also checked and marked. In total 8 bad channels were found, but the effect was minimal since none of them was on the inner face.

### **Waveform digitizer upgrade**

DRS4 (Figure 4.3) was introduced in 2009 for faster sampling rate and better linearity. However it was found that the timing resolution worsened due to noise from electronics.

Before the start of 2010 run we applied fine tuning of DRS4 to reduce noise and minimize time jitter. As a result contribution to timing resolution from electronics improved to 50ps compared to 130ps in 2009.

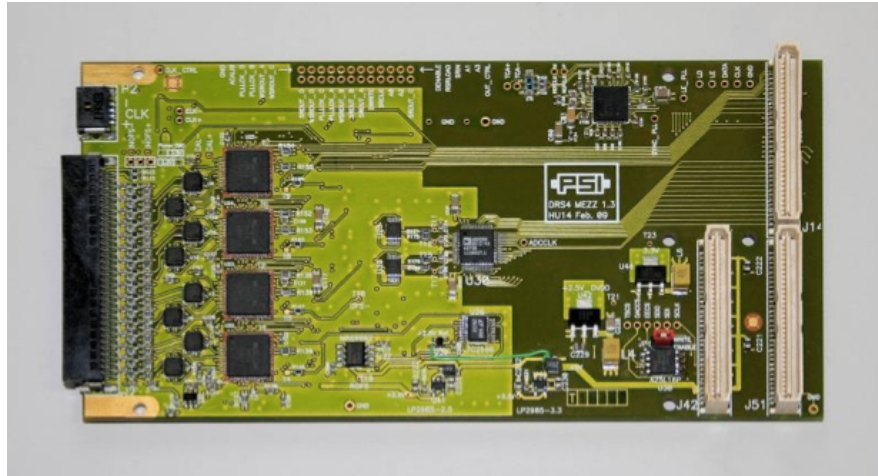


**Figure 4.3:** DRS4 board.

### DAQ

DAQ live time in 2010 was  $\sim 84\%$  and dead time was 6% less than 2009.

### Alignment

Optical survey was carried out to determine all DCH modules positions and directions[60]. Relative alignment between LXe detector and drift chamber was calculated using cosmic ray, CW and AmBe data[61]. Combining all the results, the average difference between measured and reconstructed position was  $\Delta z = -6.2 \pm 2.3$  mm, where  $z$  is the position along the beam line. This result was applied in physics analysis.

## 4. RUN 2010

---

### 4.5 BTS problem

In November there was a BTS quench which ended the run prematurely. We still managed 67 real time days for data taking and gathered 1.9 times more data than 2009. The incident was investigated and repair work was done to ensure the running of experiment in the next year.

# 5

## Event Reconstruction

An event recorded by the experiment consists of waveforms that are analyzed to reconstruct the kinematics of the detected particles. This chapter describes the methods to reconstruct energy, time and angle of the photon and positron. We first look at each detector separately and then discuss the combined analysis to reconstruct the angle and time between positron and gamma.

### 5.1 Drift Chamber

The waveform of a charged particle passing through the drift chamber is used to calculate the position and momentum of the particle, a decay vertex and set of emission angles from the projection to the target, a projected impact location at the timing counter, and the overall path length of the trajectory.

We measure the arrival time and charge on each wire and pad on the passage of the particle through a cell. The information from each cell, called a hit, is checked with other hits on the same chamber and groups of hits from the same particle are collected into clusters, which are then collected into tracks. A global fit is made to the track trajectory to estimate the track momentum, the interception at the timing counter and target plane, and the total path length from the target to the timing counter.

## 5. EVENT RECONSTRUCTION

### 5.1.1 Waveform Analysis

We get six waveforms from a drift cell: two from both ends of an anode wire and four from cathode pads, as shown in Figure 5.1. We begin by searching for pulses. A pulse and its width are identified by a maximum peak over a threshold and pursuing the pulse in both directions above another given threshold. We extract time of each pulse by a single-threshold crossing time and charge of the pulse is integrated over 50 ns in order to optimize the signal-to-noise ratio.

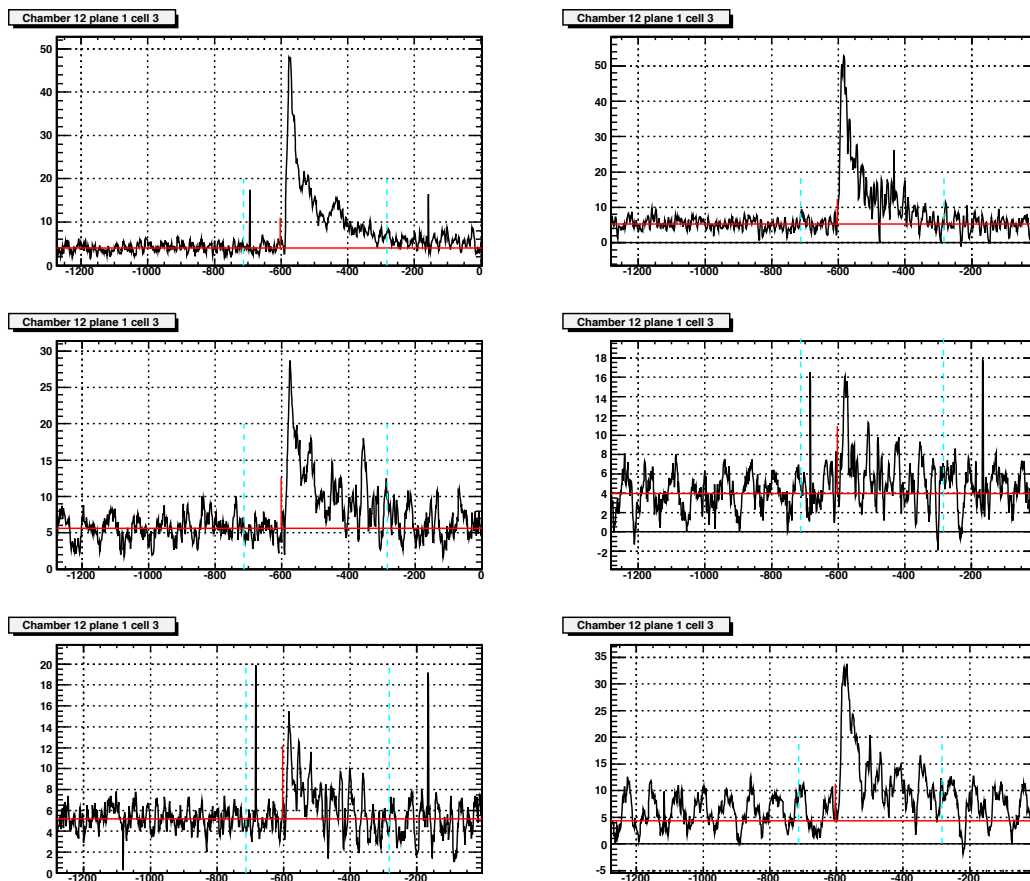


**Figure 5.1:** The six waveforms associated with a hit. The horizontal red lines are the calculated baselines, the vertical red lines are the leading edge time, and the region between the two dashed blue lines is the expected region where triggered signal appear.

### 5.1.2 Hit Reconstruction

We measure the  $z$ -coordinate of drift-chamber hit by a combination of anode charge division and cathode-vernier-pad. Assuming equal preamplifier input impedance,  $R$ , at each end of the anode, and a uniform resistance per unit length,  $\rho$ , the  $z$  coordinate along a wire of length  $L$  can be roughly calculated as

$$z = \left( \frac{R}{\rho} + \frac{L}{2} \right) \cdot \epsilon_a \quad (5.1)$$

where charge division  $\epsilon_a$  is defined as

$$\epsilon_a \equiv \frac{Q_u - Q_d}{Q_u + Q_d} \quad (5.2)$$

Here  $Q_u$  and  $Q_d$  are the charges on upstream and downstream end respectively.

Then we reconstruct is more precisely using vernier pattern. The charge division for the vernier pads can be similarly defined for inner side cathode ( $\epsilon_i$ ) and outer side cathode ( $\epsilon_o$ ) respectively. The phase of the vernier pattern is defined as

$$\alpha = \tan^{-1} \frac{\epsilon_o}{\epsilon_i} \quad (5.3)$$

Then the  $z$  coordinate can be calculated as

$$z = \frac{l}{2\pi} \cdot \alpha + n \cdot l \quad (5.4)$$

where  $l$  is the the length of a pad cycle, equal to 5 cm. Figure 5.2 shows the vernier circle and relation between anode charge division and vernier circle.

### 5.1.3 Track Reconstruction

To find tracks, we first group hits into clusters if they are consistent with coming from the same positron, using the  $z$  and time information. The clusters are selected with requirements on number of cells between hits, and their deviations from  $z$ .

Next, we connect the clusters that resemble one turn of a positron trajectory. If we find a combination of three clusters, called seeds, we roughly reconstruct the trajectory

## 5. EVENT RECONSTRUCTION

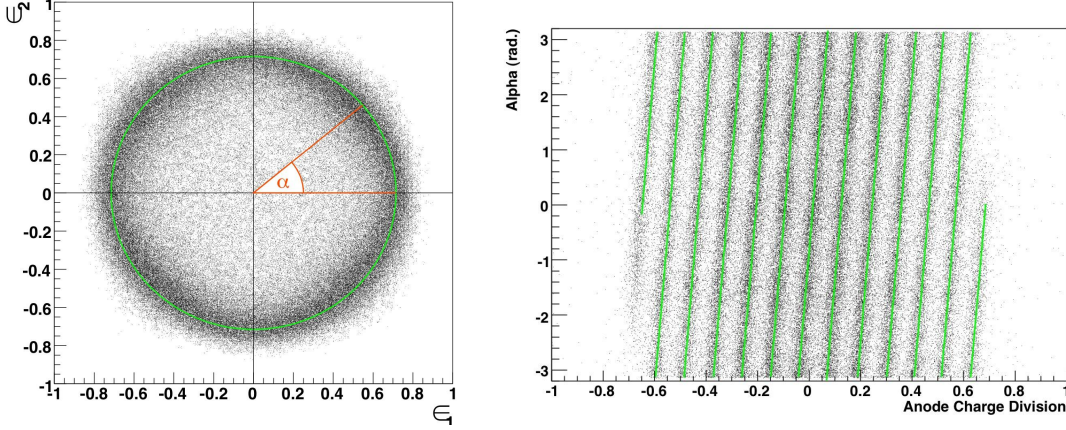


**Figure 5.2:**  $z$  reconstruction of the drift chamber hit. (a) shows the vernier circle. One turn corresponds to a period of vernier pattern (5 cm). (b) shows relation of the vernier phase with anode charge division.

with a circle. Once we find a track candidate by connecting clusters associated with a positron, we can estimate the time of the track by using the timing of all hits belonging to the track.

The drift time of each hit, which is the time elapsed between a primary ionization event and the arrival of the earliest part of the subsequent avalanche, is calculated by  $t_{drift}^i = t_{hit}^i - t_{track}$ , where  $t_{hit}^i$  is arrival time of  $i$ -th hit, and  $t_{track}$  is the track time, which is calculated by correcting the TIC time by the average time of flight between the DCH and the TIC.

The drift distance can be calculated from drift time, incident angle, left-right solution, and B-field strength.

### 5.1.4 Track Fitting

All track candidates with at least 4 clusters are sent to a Kalman filter [62] to fit a trajectory to the set of hits. The Kalman filter is effective for tracks with small number of hits or noise, thus suited to tracking in MEG experiment.

The Kalman filter recursively estimates parameters by each measurement in order. The track of a positron can be described by a vector of five parameters: two for the

position, two for the direction and one for the momentum. A fit example is shown in Figure 5.3.

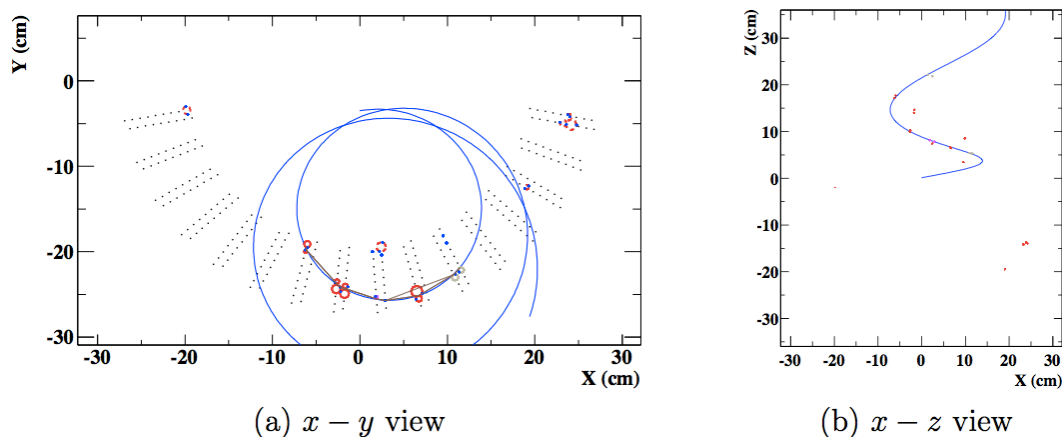


**Figure 5.3:** Event display of positron tracking. Fitting is performed with Kalman filter.

## 5.2 Timing Counter

After passing through the drift chamber, positrons reach the timing counter and deposit energy in scintillating bars. The waveforms read out at the end of each bar is used to measure impact time and position, which are used to match a TIC hit with a DCH hit.

### 5.2.1 Waveform Analysis

The output of a PMT is divided into three outputs with fraction of 1:1:8. 10% of the output is digitized by DRS directly (PMT pulse) while 80% of the output goes to the double-threshold-discriminator (DTD) and digitized (NIM pulse). Figure 5.4 shows an example of a PMT waveform.

A template waveform is prepared by averaging many pulses channel-by-channel. This is then fitted to the NIM pulse to get the baseline and leading edge time.

Charge and amplitude are measured with PMT pulses. The charge is estimated by integrating the pulse over 30 ns, and the amplitude is measured as the difference

## 5. EVENT RECONSTRUCTION

---

between the estimated baseline and the peak voltage of the pulse.

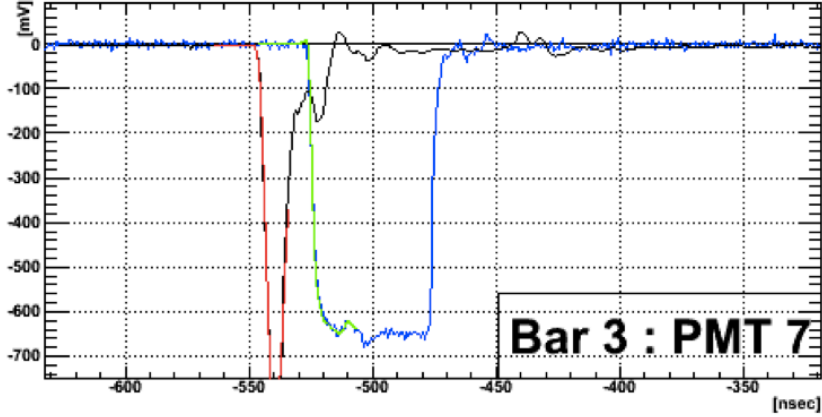


**Figure 5.4:** Figure 5.10: An example of the waveforms used in the timing counter reconstruction. The black line is a DRS output, which is fitted to a template (red). The blue line is the NIM pulse output, which is fitted to another template (green). The time delay of the NIM pulse with respect to the DRS waveform is due to an electronic delay in the double threshold discriminator.

### 5.2.2 Hit Reconstruction

The leading edge time of each PMT is corrected for time walk effects, and the difference between the two times is used to calculate the  $z$  coordinate. We reconstruct the hit time by averaging two PMT times corrected for photon propagation time in the bar based on the  $z$  coordinate.

High momentum positrons often penetrate a few bars. For these events, hits associated with one positron are clustered by closeness in time and  $z$  location. Multi-hit clusters take the time of the first hit bar as the cluster time.

## 5.3 DCH-TIC Interconnection

First reconstructions of the tracking and timing counter are done independently. Then DCH tracks and TIC clusters that belong to a single trajectory are selected.

The time of flight of the trajectory from the muon decay vertex to the impact location

in the TIC is computed by dividing the total path length by the speed of light. The projection from the last chamber to TIC is complicated by the length and materials such as cables and preamplifiers in its path. The accuracy is thus limited by scattering and energy loss. We use an additional correction,  $|\Delta z_{DCH-TIC}|$  to time of flight. It is measured with Daliz data from  $\pi^0$  runs.

In the events with more than two hits, the trajectory length and hit time measurements are used to estimate the impact time at the first bar. In this case the TIC time estimator is the average of the two measurements. The best estimate of the hit time at the first bar is then corrected by the best estimate of the time of flight to get the time of emission from the decay vertex.

## 5.4 LXe Detector

Waveforms measured by the PMTs inside the liquid xenon detector gives the information of photon energy, time, and position. We first reconstruct the number of detected scintillation photons and arrival time in each PMT, then the energy, time, and first conversion position of the detected photon.

### 5.4.1 Waveform Analysis

Typical waveform of LXe interacting with a photon is shown in Figure 5.5. The time of each PMT waveform is extracted with the digital-constant-fraction method, namely, the time at which the waveform reaches 30% of full pulse height. By this method, we can determine the pulse time independently of the amplitude (no time walk effect). In order to reduce noise and statistical fluctuations, the pulse height is measured indirectly from the charge assuming a linear scaling relationship.

The pulse charge is estimated by integrating the waveform, and is later converted to number of photoelectrons observed by the PMT. In order to reduce noise of  $\sim 1$  MHz, we apply a high-pass filter. We do not need to filter the high frequency noise as integration itself works as a low pass filter. A high-pass filter is applied by subtracting a moving average of the waveform. The number of points in the moving average is set

## 5. EVENT RECONSTRUCTION

---

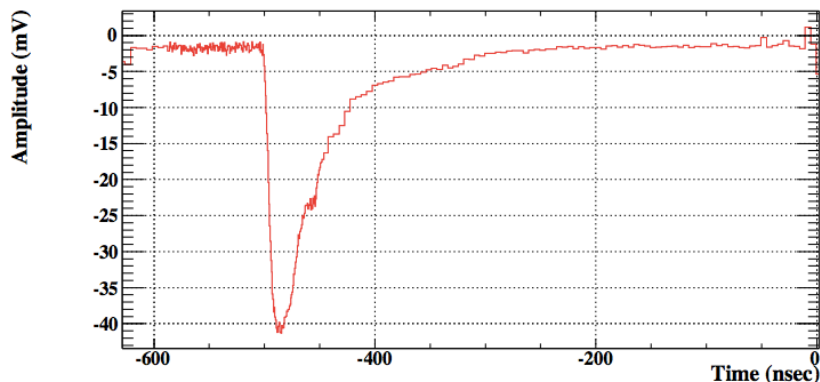


Figure 5.5: Typical waveform of a PMT in LXe detector.

to 89, corresponding to a cutoff frequency of 11 MHz. A filtered waveform is shown in Figure 5.6. The integration range is determined by the zero-crossing time of the sum of waveform and is applied to all PMTs. The range of the integration is 48 ns, which acts as a low-pass filter with a 21MHz cut-off frequency.

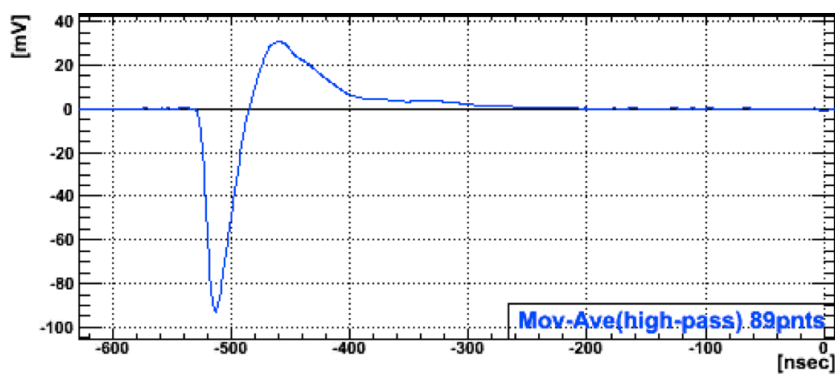


Figure 5.6: A high-pass filtered waveform.

Sometimes when a photon interacts at a close point to a PMT, the signal is large enough to saturate the electronics. Figure 5.7 shows a saturated waveform. In these cases, the charge is estimated with a time-over-threshold (ToT) method. The time span during which the waveform is above a threshold, 150 mV, is related to the expected charge based on the average pulse shape of photon interaction events (shown in Figure 5.8 as "template waveform"). In cases of PMT saturation, the charge is

calculated directly from the ToT value. The recovery is important because about 15% of the photons interact within 1 cm of a PMT and most of them have at least one saturated channel.

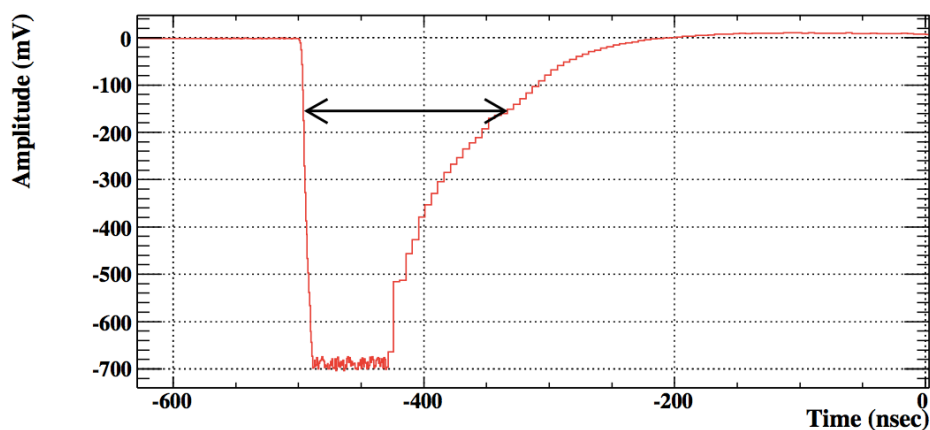


Figure 5.7: A saturated waveform.

### 5.4.2 Photon Reconstruction

We reconstruct the position of the shower by treating it like a point-like interaction. First we convert PMT charge to number of photoelectrons with

$$N_{pe,i} = Q_i / (e \cdot G_i) \quad (5.5)$$

where  $Q_i$  is a pulse charge of the  $i$ -th PMT,  $e$  is the elementary charge, and  $G_i$  is the gain. The number of scintillation photons can also be written as

$$N_{pho,i} = N_{pe,i} / QE_i \quad (5.6)$$

where  $QE_i$  is the quantum efficiency of the PMT. The calibration of PMTs is described in Section 6.4.1.

## 5. EVENT RECONSTRUCTION

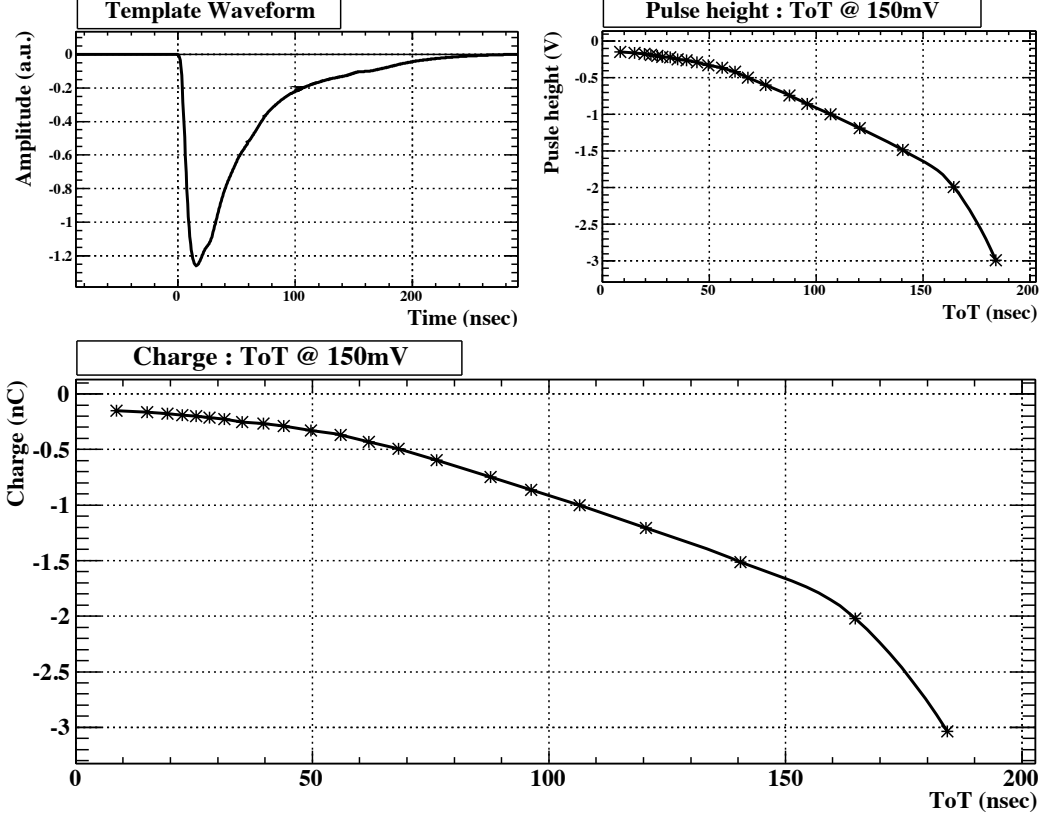


**Figure 5.8:** Charge estimation with ToT. Pulse shape of template waveform is used to get the conversion factor from ToT to charge.

### Position

A photon interaction point is reconstructed by fitting the PMT output distribution. At each point  $(x_\gamma, y_\gamma, z_\gamma)$ , the solid angle of a photon-cathode,  $\Omega_i(x_\gamma, y_\gamma, z_\gamma)$ , is calculated numerically. The interaction position  $(x_\gamma, y_\gamma, z_\gamma)$  is calculated by minimizing

$$\chi_{pos}^2 = \sum_i \frac{N_{pho,i} - c \times \Omega_i(x_\gamma, y_\gamma, z_\gamma)}{\sigma_{pho,i}(N_{pho,i})} \quad (5.7)$$

where  $c$  is a free parameter of the fitting, and  $\sigma_{pho,i}(N_{pho,i})$  is the statistical uncertainty of the PMT charge and is calculated by

$$\sigma_{pho,i}(N_{pho,i}) = \frac{1}{QE_i} \times \sigma_{pe,i}(N_{pe,i}) = \frac{\sqrt{N_{pe,i}}}{QE_i} = \sqrt{\frac{N_{pho,i}}{QE_i}} \quad (5.8)$$

The position fit is performed twice to smooth effects of non-point like shower development. Only inner face PMTs are used because they are closest to most of the energy deposition and thus the least sensitive to the scattering and absorption. First fitting uses PMTs whose center lie within a 3.5-PMT radius around one with maximum light. Second fitting is then performed with PMTs whose whose center lie within a 2-PMT radius around the result of the first fitting. Typically, 45 and 15 PMTs are used in the first and second fit, respectively.

The final fitted position can be written in the  $(u, v, w)$  coordinate system as

$$u = z, v = r_0 \tan^{-1}(-y/x), w = \sqrt{x^2 + y^2} - r_0 \quad (5.9)$$

where  $r_0 = 67.85$  cm, the radius of the inner face.

Based on Monte Carlo, no bias is observed in  $v$ , while  $|u|$  and  $w$  have larger values than the true position. The photon comes into the detector with incident angle with respect to the PMT direction, which causes a bias in  $u$  towards outside direction because the shower usually develops in the original photon direction. The bias in  $w$  is towards deeper direction for the same reason. Corrections deduced from MC are applied to  $u$  and  $w$ . In addition, corrections for fluctuations in the shape of the shower are applied, based on the difference between two fitting results.

### Energy

Gamma rays around 50 MeV converted in LXe detector usually deposit all of their energy in the active volume. Our energy reconstruction is on the idea that the total number of collected photons is proportional to the original gamma energy regardless of position and shape of the shower. In that case, the deposited photon energy is proportional to the weighted sum of the scintillation photons:

$$N_{sum} = \sum_i w_i \times N_{pho,i} \quad (5.10)$$

where  $w_i$  is the inverse photocathode coverage of the  $i$ -th PMT.

## 5. EVENT RECONSTRUCTION

---

This estimation works well when the first interaction point is deep enough, i.e.  $w > 2 - 3$  cm. For shallow events however the solid angle of PMT varies strongly with shower position and the coverage can no longer assumed to be uniform. 55 MeV photons from  $\pi^0$  decay are used to study the dependence of  $N_{sum}$  on the conversion depth and solid angle of the PMT with maximum light. The result is shown in Figure 5.9 and it is used to correct for events with  $w < 3$  cm. We apply a correction of  $N_{sum}$  with  $\Sigma_{in,max}$  for such events. The correction function is a linear function, whose coefficients are extracted by the 55 MeV photons in the  $\pi^0$  calibration.

The remaining position dependence is corrected globally after the reconstruction. The details of calibration of position dependence and correction are described in Section 6.4.2.

A position-dependent correction factor,  $F(u, v, w)$ , is estimated from the 17.6 MeV peaks in the CW- Li data. Thus the photon energy is given by

$$E_\gamma = \alpha F(u, v, w) N_{sum} \quad (5.11)$$

where  $\alpha$  is the correction factor from the 55 MeV calibration. The linearity of  $N_{sum}$  to gamma energy  $E_\gamma$  was checked with several calibration methods[6] as shown in Figure 5.10.

### Time

Each PMT has a first interaction time of

$$t_{hit,i} = t_{PMT,i} - t_{delay,i} - t_{offset,i} \quad (5.12)$$

where  $t_{PMT,i}$  is the leading edge time of the  $i$ -th PMT.  $t_{delay,i}$  is the time delay during scintillation light propagation in LXe, and constant electronic delays are in the last term.

The second term  $t_{delay,i}$  comes from three contributions:

$$t_{delay} = t_{prop}(d, v_{eff}) - t_{indir}(\lambda) - t_{walk}(N_{pe}) \quad (5.13)$$

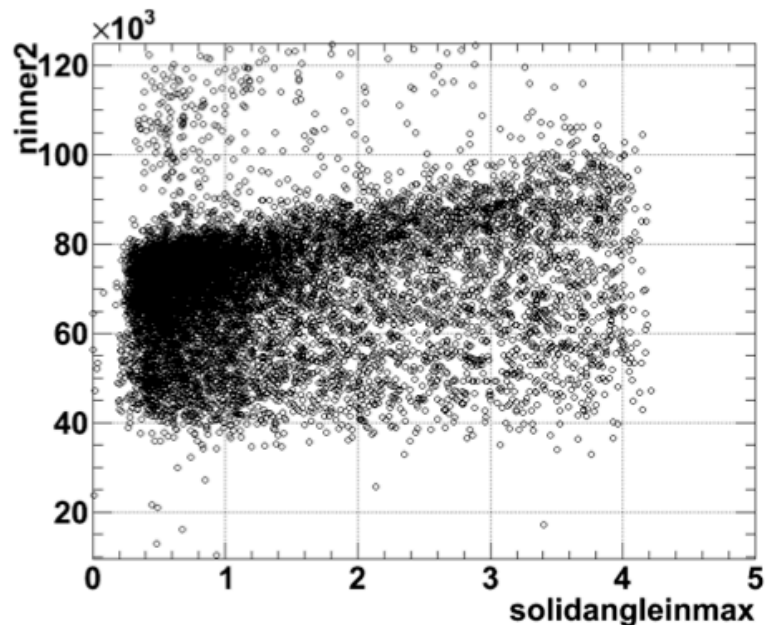


**Figure 5.9:** Correlation between  $in, max$  and sum of inner PMT  $N_{pho}$  for  $w < 3$  cm.

$t_{prop}$  is the propagation time in LXe, and it depends on distance between the source and PMT,  $d$ , and the speed of scintillation light,  $v_{eff}$ .  $t_{indir}$  comes from photons reaching a PMT after reflection off walls or scattering in xenon. It depends on the incident angle  $\lambda$ . And  $t_{walk}$  is the time walk effect of time extraction method, which is correlated to the number of observed photoelectrons,  $N_{pe}$ .

Then we can determine the hit time,  $t_{LXe}$  by minimizing

$$\chi_{time}^2 = \sum_i \frac{(t_{hit,i} - t_{LXe})^2}{\sigma_{t,i}(N_{pe})^2} \quad (5.14)$$

where  $\sigma_{t,i}(N_{pe})$  is the time resolution of  $i$ -th PMT as a function of  $N_{pe}$ .  $\sigma_{t,i}(N_{pe})$  is calculated with PMTs that collect over 50 photoelectrons, typically about 150 of them.

### 5.4.3 Pileup

With the high muon rates in the experiment, LXe detector is susceptible to events with multiple gamma rays. Such pileup events are identified spatially by light distribution

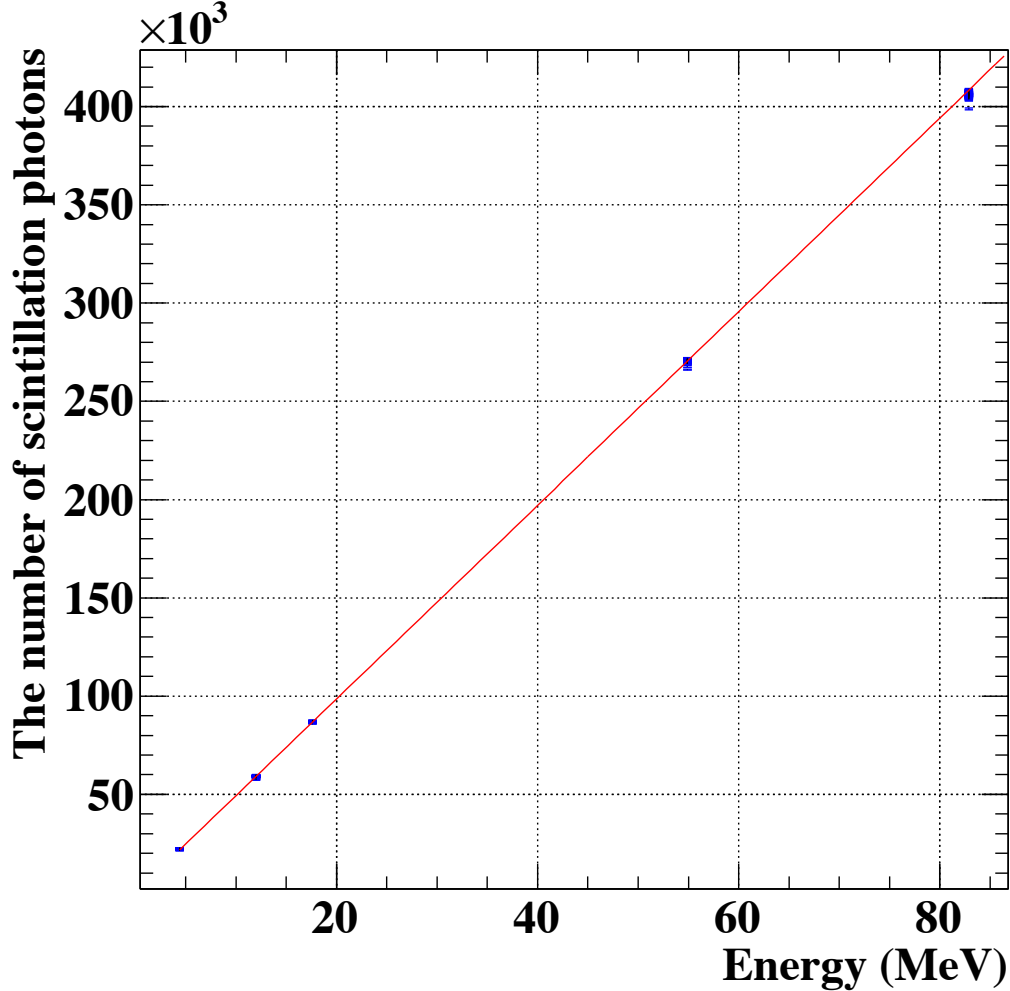


**Figure 5.10:** Linearity plot of  $E_\gamma$  vs  $N_{sum}$ . The five points are given from 4.4 and 11.7 MeV from CW-B run, 17.6 MeV from CW-Li run, and 54.9 and 82.9 MeV from  $\pi^0$  run. Red line is the best-fit linear function whose intercept is fixed to zero.

in both inner and outer face PMTs, and temporally by the distribution in PMT times.

For the first method, we perform a peak search. More than one peak in the PMTs would indicate pileup. Secondary peaks are distinguished by locating PMTs with  $N_{pho} > 200$  at positions isolated from the primary peak.

For the second method, we use the normalized  $\chi^2$  value of the time fitting,  $\hat{\chi}_{time}^2$ .

Usually large  $\hat{\chi}_{time}^2$  occurs when different groups of PMTs have different interaction times of different photons. The threshold for pileup recognition is  $\hat{\chi}_{time}^2 > 3$ , as deduced from MC (Figure 5.11).

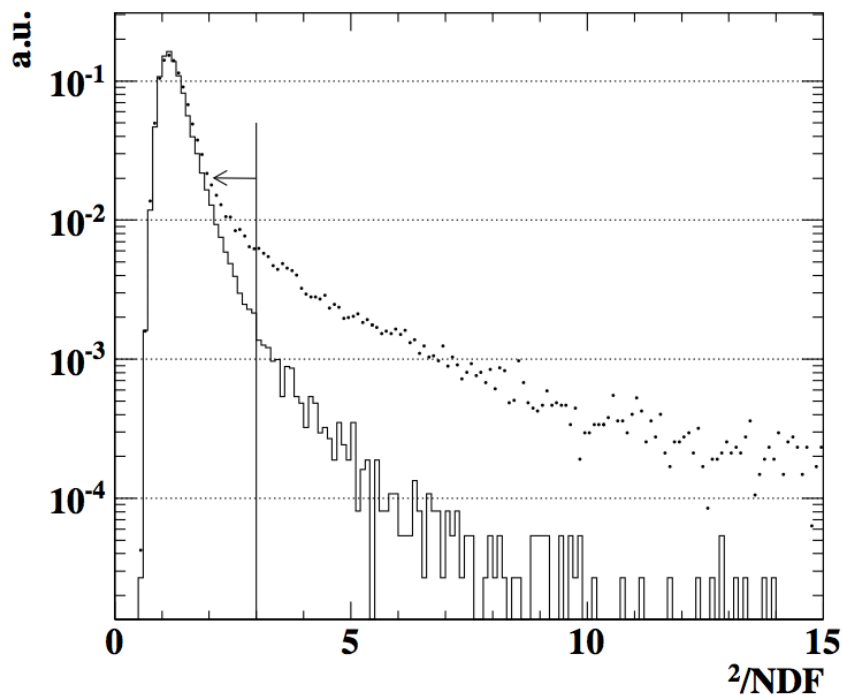


**Figure 5.11:** Distribution of normalized  $\chi^2$  of the time fitting on data (dotted line) and signal MC without pileup (solid line).

Since the probability of pileup is as large as 15%, it is important to reconstruct pileup events rather than simply discarding them. First a look-up table of expected PMT outputs is prepared with the 17.7 MeV gamma-ray in CW run. The table has average output of each PMT for each mesh ( $1.55 \times 1.55 \times 1.55 \text{cm}^3$ ) for the reconstructed position. If a pileup is found, the elimination is done in the following procedure:

1. Estimate energy by fitting PMT charges with the expected distribution stored in the table except for those around the pileup gamma.
2. Calculate the expectation of PMT outputs around the pileup region using the table and replace them with the expectation.

## 5. EVENT RECONSTRUCTION

---

3. Reconstruct energy again with the replaced PMT outputs.

Figure 5.12 shows light distribution before and after eliminating pileup events. Pileup events identified only by time distribution but not spastically separated are not recovered.

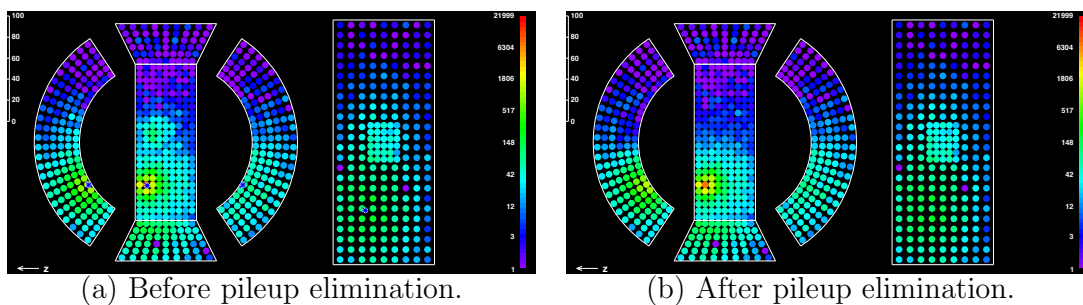


**Figure 5.12:** Photon distribution before and after pileup elimination.

Dead PMT channels are also recovered using the same table. Replacement number of photons are estimated from the average of three PMTs at symmetric locations along  $u$  and  $v$  direction.

# 6

## Calibration

Calibrations are crucial to the precise measurement required by MEG experiment. In addition, one needs a considerable running stability of all detectors. We developed various calibration and monitoring methods to fulfill these requirements. Some of them are complementary and some are redundant in order to obtain optimized performance of the experiment. Some instabilities and deviations are corrected by calibration data.

### 6.1 DRS

#### 6.1.1 Voltage Calibration

Every cell of every DRS chip has a different and non-linear response to voltage. We prepare detailed response curves in advance by looking at the response for different input voltages from internal DC voltage generator on DRS boards. The calibration is done online so the data written in the disk is already calibrated for voltage response.

#### 6.1.2 Time Calibration

A sampling frequency is generated by a series of inverters in a DRS chip. The sampling interval of each cell in a DRS chip can vary due to characteristics of each individual inverter. Sampling intervals of cells between the zero-crossing period were adjusted so that the measured zero-crossing period become that of input sine wave. This regulations were repeated until sampling intervals of all cells got converged. A global common clock

## 6. CALIBRATION

---

is distributed to all DRS boards from the trigger system and used to synchronize the phase among chips.

### 6.2 Drift Chamber

#### 6.2.1 z-coordinate Calibration

The z-coordinate calibration of drift chamber means the relative gain correction on each ends and is done by using the known pattern of vernier pad. We calibrate the relative gains so that the reconstructed length of a vernier circle is the pitch length of 5cm. We calibrate the relative gain correction for cathode pad based on the fact that the mean charge collected on one cathode pad should be a quarter of total charge induced on the anode.

#### 6.2.2 Time Offset Calibration

It is necessary to determine the time offset for each channel in order to measure the drift time precisely. Several sources of difference, such as differences of cable length of both the signal and the trigger electronics, transition-time spread of electronics devices contribute to the intrinsic timing jitter and it can be determined by fitting the distribution with a polynomial function, empirically given as fifth-order one. The offset is determined by the time that the height of distribution reaches 15% of maximum.

#### 6.2.3 Time-to-Distance Calibration

Time-to-distance functions are calculated by GARFIELD[50] and the calibration is done with simple iterative procedure[6].

1. Calculate a difference between obtained drift distance and closest approach from the wire to the track, called residual
2. Put a corrective offset to the drift distance so that the residual is minimized.
3. Perform above for many events with similar incident angle and closed field strength, and build a new time-to-distance plot.

4. Fit the plot and form a new time-to-distance function.

The procedure is repeated until convergence is achieved.

## 6.3 Timing Counter

### 6.3.1 z-coordinate Calibration

The time offset between two PMTs is adjusted because  $z$  hit position is reconstructed by the time difference between the two. Reconstructed positron tracks are used as a reference of  $z$  hit position. The relative time offset is calibrated so that the mean of  $\Delta z_{DCH-TIC}$  distribution is zero.

### 6.3.2 Inter-Bar Time Offset Calibration

The relative time offsets between bars is calibrated with CW-B data.  ${}^{11}_5B(p, \gamma){}^{12}_6C$  reaction produces gamma rays at 11.7 and 4.4 MeV. We use the 4.4 MeV gamma ray at xenon detector as a time reference and measure the 11.7 MeV one on each bar. Relative offsets are determined by the distribution of time difference after time-of-flight correction.

## 6.4 LXe Gamma-ray Detector

### 6.4.1 PMT calibration

Alpha sources and LEDs are used for the monitor and calibration of PMTs. Figure 6.1 shows the placement of LED and  $\alpha$  wires inside the LXe detector and Figure 6.2 shows the closeup of  ${}^{241}\text{Am}$  source on wire.

### Gain

LEDs attached to the lateral faces of the LXe detector are used as light sources to monitor PMT outputs and calculate PMT gains.

We calculate gains by means of statistic number of photoelectrons,  $N_{pe}$ . Observed

## 6. CALIBRATION

---

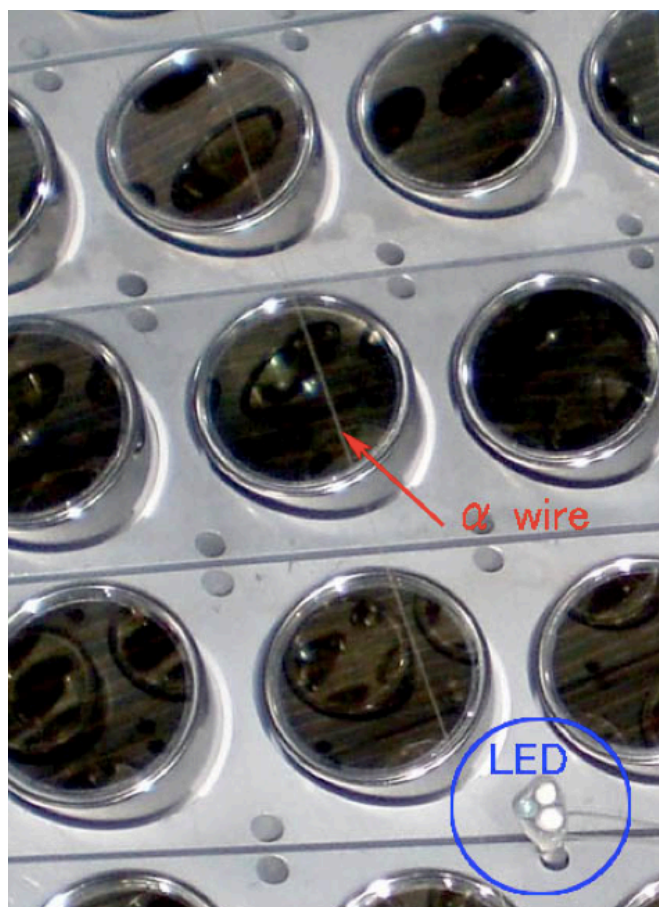


**Figure 6.1:** Inside view of LXe detector shows  $^{241}\text{Am}$  source on wire and LED on the wall. Three LEDs with different attenuations are mounted on lateral faces.



**Figure 6.2:** Closeup of  $^{241}\text{Am}$  source on wire. Diameter is  $100\ \mu\text{m}$  and length is about 2 mm.

charge,  $q$ , can be expressed in an equation with gain  $G$ , and a conversion constant  $e$ ,

$$q = G \cdot e \cdot N_{pe} \quad (6.1)$$

We assume the output of LED is constant and follows the Poisson distribution. Let  $N_{pho}$  be the number of photon from LED to the PMT, which is constant in our assumption. The average number of photonelectrons is given by  $\bar{N}_{pe} = N_{pho} \cdot QE$  where QE is quantum efficiency.

If we take many LED events, the mean and variance of the distribution becomes

$$\bar{q} = G \cdot e \cdot \bar{N}_{pe}, \quad (6.2)$$

and

$$\delta_q^2 = (Ge \cdot \delta_{pe})^2 + \delta_{noise}^2 \quad (6.3)$$

respectively. And we obtain the relation,

$$\delta_q^2 = Ge \cdot \bar{q} + \delta_{noise}^2 \quad (6.4)$$

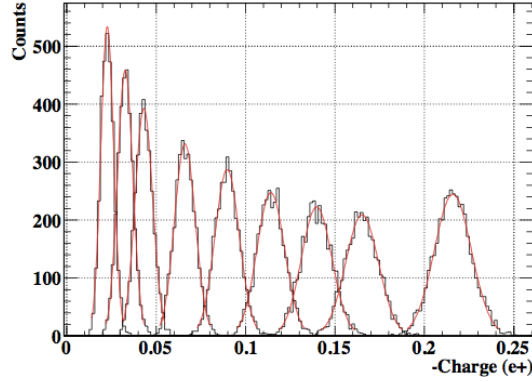
By taking LED events at different intensities we can calculate the gain as a slope of variance-mean plot and it is insensitive to contribution from noise. We take nine steps with different LED intensities without beam. Each step has 3000 events and we can obtain a relation between charge and variation as shown in Figure 6.3. The slope of the plot is then calculated as gain.

Gain calibration is taken everyday or twice a week depending on the detector situation. Additionally the most intense step was taken everyday and every time when we start or stop using beam to monitor the variation of PMT gains. LEDs are flashed with 100 Hz during the usual calibration and LED data with 1 Hz are mixed in MEG physics data taking.

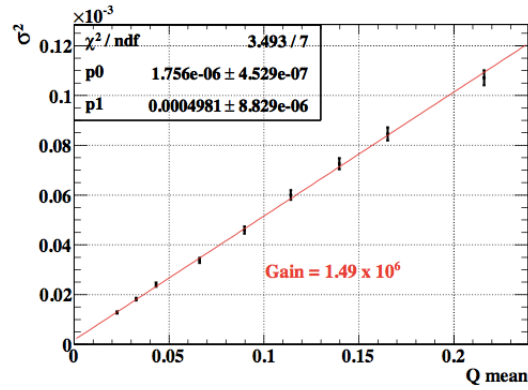
### Gain Shift

The long term stability of PMT gains is checked during the experiment. We noticed that there is temporary gain change depending on beam intensity. This is called

## 6. CALIBRATION



(a) Nine LED peaks by various intensities.



(b) Gain estimation from the slope on charge mean and variance plane.

**Figure 6.3:** Gain calculation.

'gain shift' and it has been confirmed using different methods such as LED and alpha peaks. This comes from the PMT themselves since our calculation relies on statistics of photoelectrons. Shift values are different for each PMT, and are dependent on the beam rate.

Since the shift is correlated to beam intensity we can correct it by constant monitoring. In normal beam rate condition the shift value is  $\sim 2\%$ . LED data shown in Figure 6.4 are used for the correction[3]. Gains are corrected using the variation of the peak value of LED events. Results indicate that gain shift is stabilized within 5 minutes of opening beam blocker and 20 minutes of closing beam blocker. Therefore during the experiment we wait 15 minutes after opening or closing beam

blocker before taking regular physics runs, and we wait 30 minutes to take calibrations. LED flashing runs are taken during the waiting period to monitor and correct gain shift.

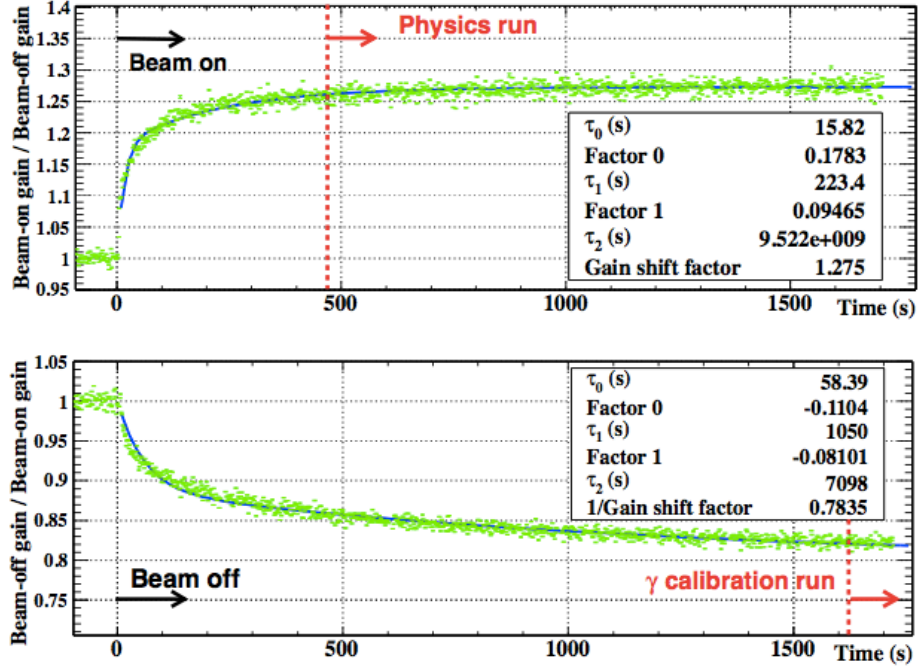


Figure 6.4: Gain shift of a worst PMT after beam blocker opened in upper figure and closed in lower.

### Gain Adjustment

Before physics data taking start, gains are adjusted to equalize each PMT performance and to keep the pulse height within a certain range.

Normally the gain of a PMT with same resistive divider is proportional to  $V^{kn}$ , where  $V$  is a bias voltage,  $n$  is the number of dynode stage and  $k$  is a factor determined by material of dynodes. The PMTs for MEG experiment however use two Zener diodes, hence the equation is approximately modified as,

$$Gain \propto (V - 0.95Z - V_0)^{11k}, \quad (6.5)$$

## 6. CALIBRATION

---

$$Z = Z_1 + Z_2 = 130\text{Volt}, \quad (6.6)$$

where  $Z$  is the total voltage at two diodes, and  $V_0$  is an offset of loss in cables. Figure 6.5 shows the relation between HV and PMT gain as well as fit result with Equation 6.5.

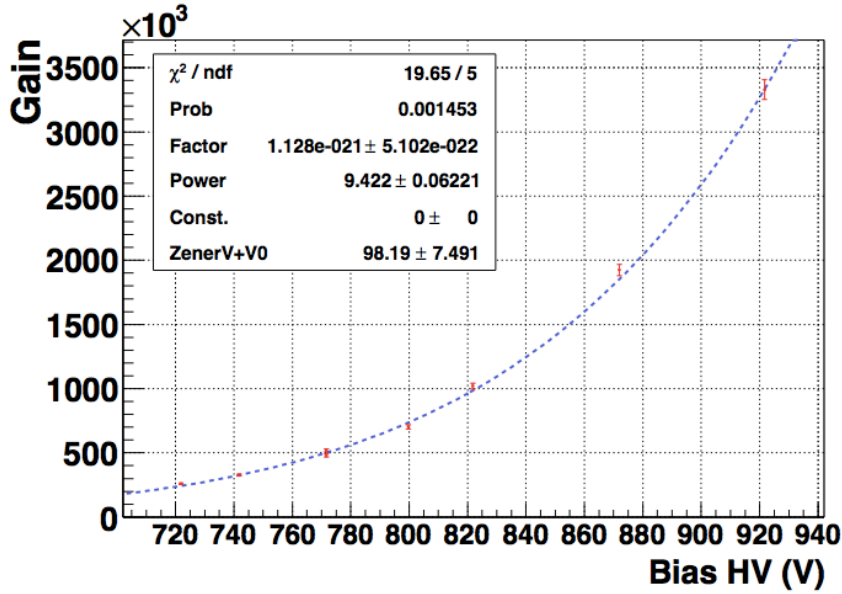


Figure 6.5: Gain - HV curve and fit.

### Gain Monitor

We noticed that gains are in a slow decrease over a large time scale, as shown in Figure 6.6. This is due to the effect of aging PMTs in large current. On average during MEG run we observe 0.1 – 0.2% decrease per day. However we can adjust the gain by increasing HV for the next several years since the applied HV is still sufficiently lower than maximum value.

### Quantum Efficiency

The quantum efficiency of PMTs can be calculated using alpha events. The point like alpha sources on wires are mounted in the detector. Since we know the positions of alpha sources and spectrum of the alpha particles, we can estimate the amount of

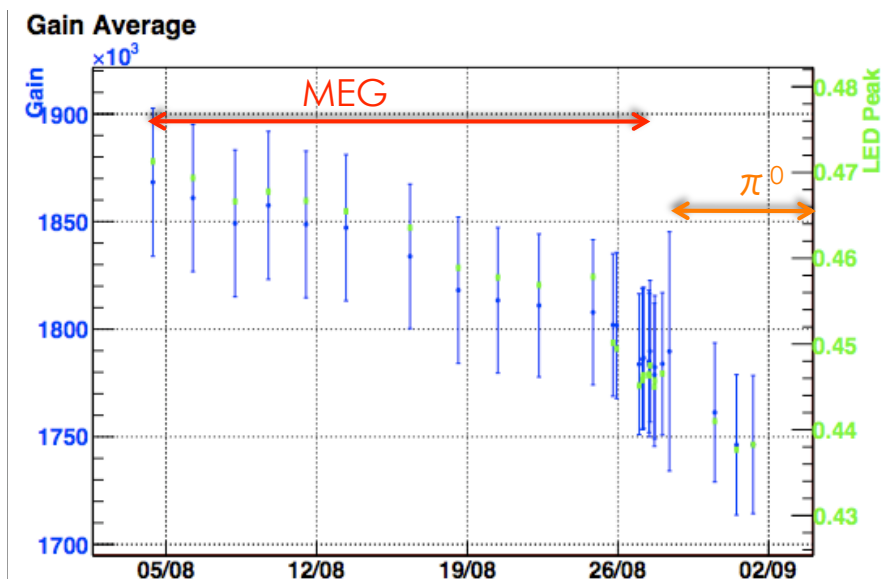


**Figure 6.6:** History of gain during MEG and  $\pi^0$  run.

light observed by a given PMT. We can then calculate QE by comparing the measured number of photoelectrons with the estimation from MC, since gains are calculated from LED data.

In liquid xenon the reconstructed positions from alpha sources make rings around the wires as shown in Figure 6.7. This is because the range of alpha particle of about  $40\mu\text{m}$  from the wire is close to the  $100\mu\text{m}$  diameter of the wire and the wire makes a shadow.

The MC-data correlation of peaks from observed photons by each source are shown in Figure 6.8 and the slope indicates QE. The events are selected for each PMT to avoid shadow positions behind the wires and sources with a large incident angle to the PMT. QE is calculated by averaging some sets of estimations to reduce statistical fluctuations. The calculated QE is then normalized so the mean of all QE is equal to 0.16.

A fine tuning for the MC such as reflection, attenuation lengths and light speed improved agreement with actual data, however the MC for the QE estimation is

## 6. CALIBRATION

---

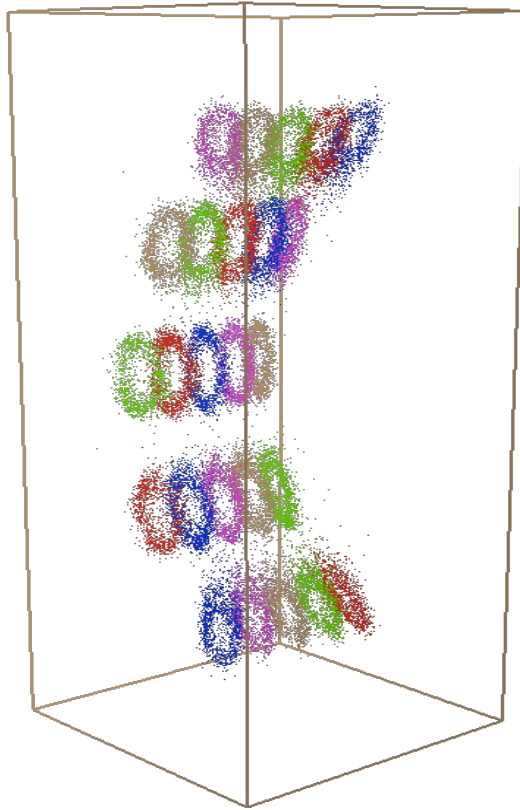


Figure 6.7: Reconstructed positions of alpha wires.

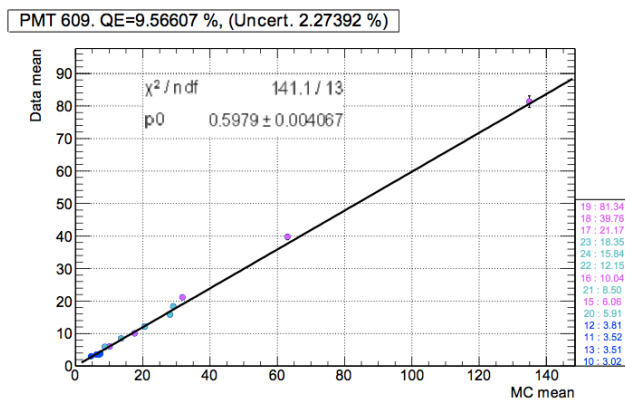


Figure 6.8: Comparison of alpha peaks between MC and data.

sensitive to these parameters and a small discrepancy between the data and the MC remains and makes it difficult to estimate QE. The effect of QE estimation on energy

resolution was studied by randomly fluctuating QE from the measured value. The effect is found to be small compared to the current energy resolution.

In addition a global bias is observed as difference of non-uniformity between data and MC. We use 17.7 MeV gamma ray from  ${}^7_3\text{Li}{}^8_4\text{Be}$  to correct the asymmetries observed from PMTs at symmetric positions. After correction the stability of QE is within  $\sim 0.2\%$  (Figure 6.9).

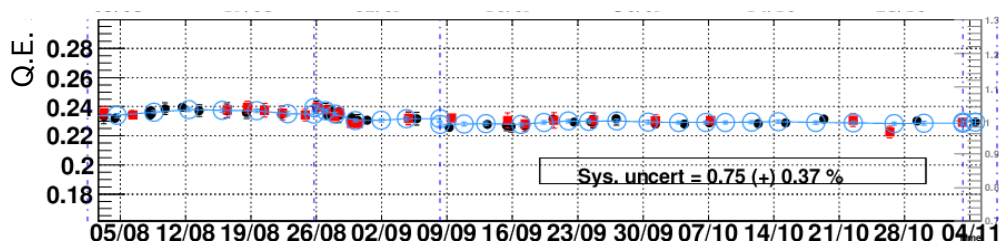


Figure 6.9: Stability of averaged QE.

#### 6.4.2 Non-Uniformity

The reconstructed scintillation photons has a non-uniform response due to geometrical effect of different effective coverage and finite absorption length. Such position dependent response can be corrected by non-uniform correction based on measurement in calibration runs. Correction factors along  $u$  and  $v$  are made with 17.7 MeV peaks in CW runs while depth correction alongside  $w$  is made with 55 MeV  $\gamma$ -ray peaks in  $\pi^0$  runs. The correction factor is estimated with two dimensional relation on  $u - v$  plane and one dimensional relation along depth,  $w$ . The peak transition along  $w$  depends both on the energy scale and on the position on  $(u, v)$ . Therefore, the depth correction is made with three separated  $u$  positions. The lateral walls are closer to each other than the top and bottom faces, hence peaks have larger dependence along  $u$  direction than  $v$  direction. Figure 6.10 shows factors of depth correction.

The remained  $u - v$  non-uniformity is estimated after the depth dependence is corrected. Figure 6.11 shows the correction on  $u - v$  plane. The total non-uniformity after correction is less than 0.3%.

## 6. CALIBRATION

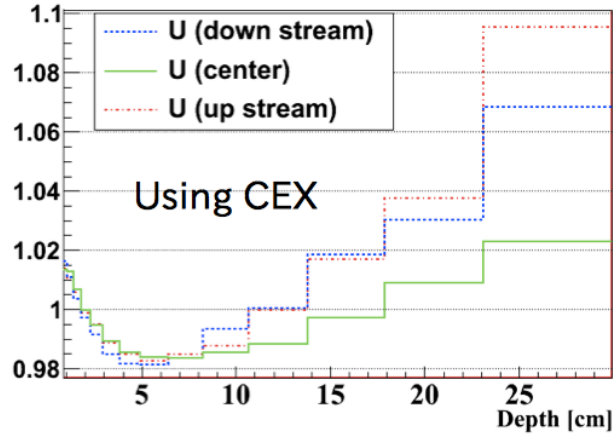


Figure 6.10: Non-uniformity correction on  $u - v$  plane.

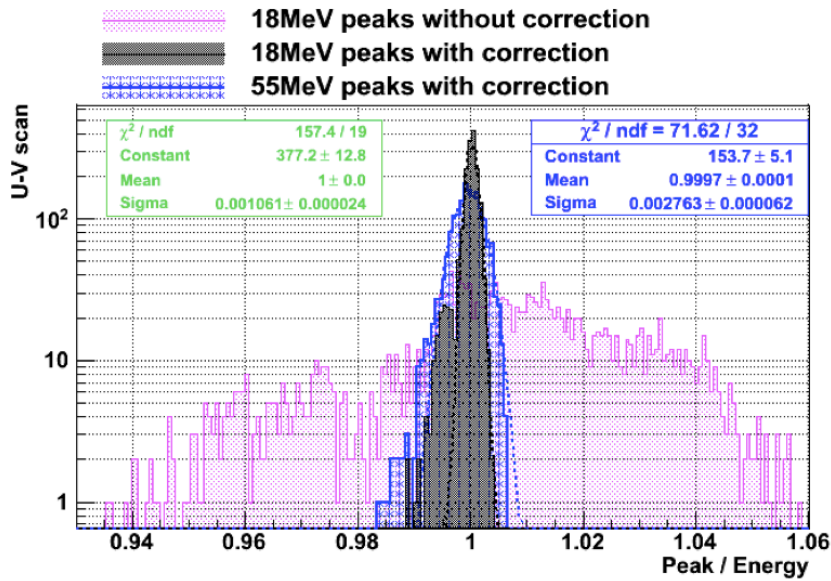


Figure 6.11: Non-uniformity correction on  $u - v$  plane.

### 6.4.3 Energy Scale and Light yield

Light yield monitoring is important because it relates to energy scale that is determined by the 54.9 MeV peak in  $\pi^0$  runs. We monitor light yield with various sources during beam-off periods. Details on the energy scale is described in Section 7.2.

$\pi^0$  run

We use the 54.9 MeV near signal energy from  $\pi^0$  run to determine the energy scale. Details of the reaction is described in Section 3.6.1.

## CW run

The CW calibration run around 30k events was taken to collect 17.7 MeV lithium peaks once per a few days during physics run. Details of the CW accelerator was described in Section 3.6.2.

## Cosmic ray

The Landau distribution from cosmic rays is obtained by selecting muons penetrating outer face and inner face, as shown in Figure 6.12.

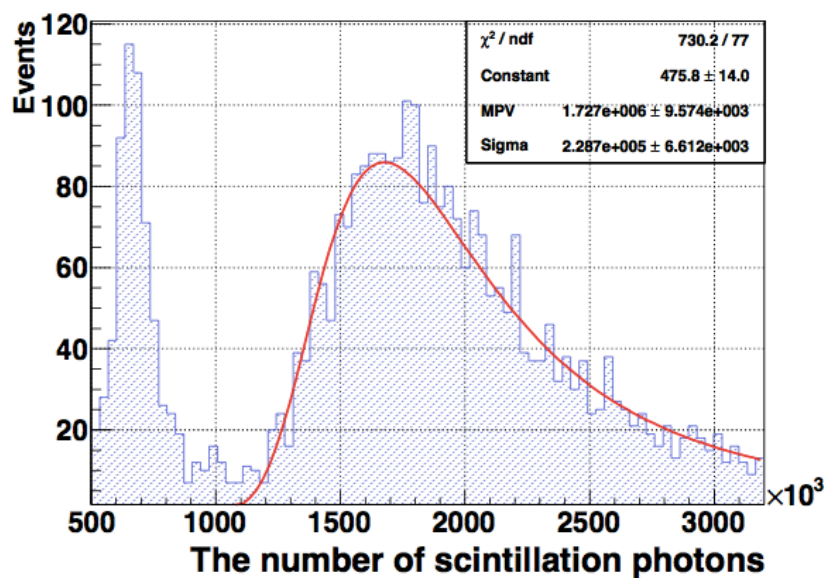


Figure 6.12: Cosmic ray peak.

## 6. CALIBRATION

### AmBe source

The  $^{241}\text{Am}^9\text{Be}$  source provides a 4.4MeV  $\gamma$  from  $^{12}\text{C}^*$  that is produced in the  $^9_4\text{Be}(\alpha, n)^{12}_6\text{C}^*$  reaction. Peaks with AmBe source are shown in Figure 6.13.

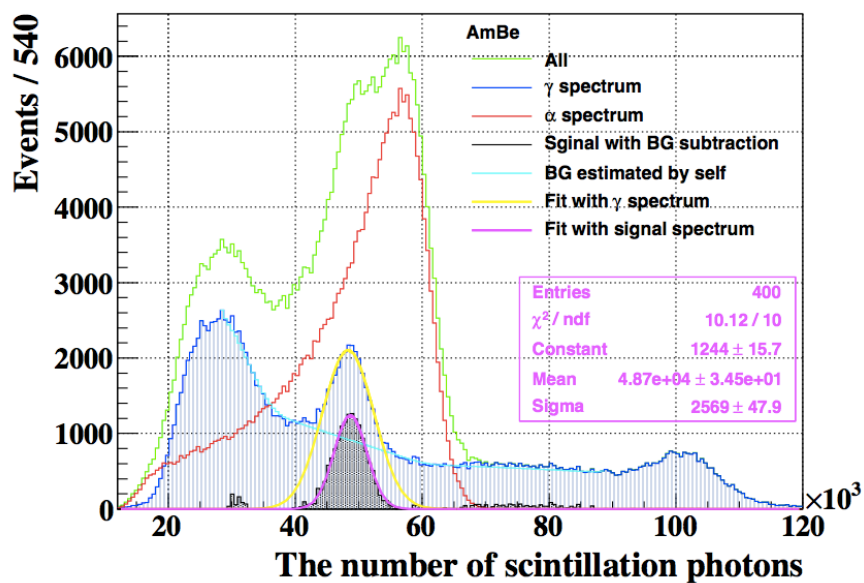


Figure 6.13: Gamma ray peaks from AmBe sources.

### Alpha source

The alpha peaks are taken with LED runs to estimate QE. The monitor of alpha peaks is important to monitor the purity of xenon and stability of the detector. Alpha peaks are shown in Figure 6.14.

### Neutron capture by Ni

Another calibration source is the 9 MeV gamma peak from thermal neutron capture reaction  $\text{Ni}(n, \gamma)\text{Ni}^*$ . The neutron generator can be used when beam is on. Peak from Ni is shown in Figure 6.15.

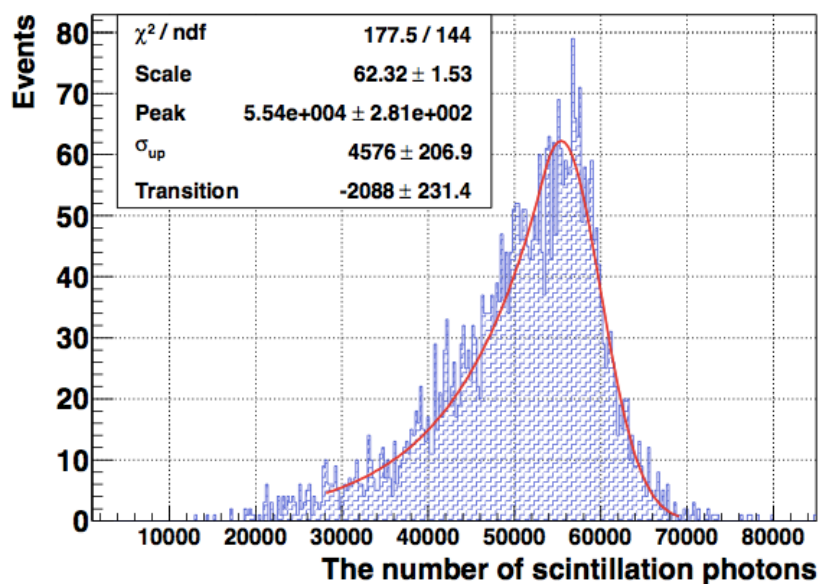


Figure 6.14: Alpha peak of all sources.

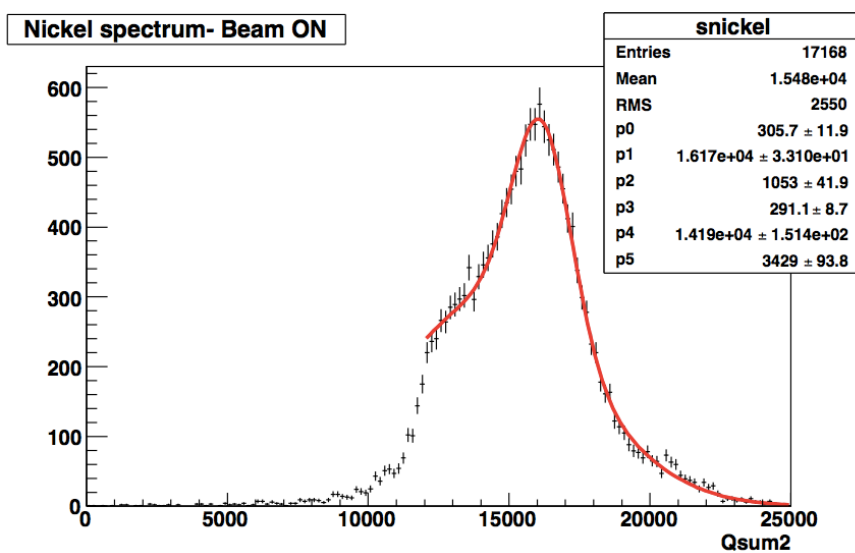


Figure 6.15: Ni peak during beam time.

## 6. CALIBRATION

---

# 7

## Performance

### 7.1 Event Selection

Here we describe selection criteria for the performance evaluation. These criteria are also applied in the final analysis. However we apply likelihood analysis with event-by-event PDFs, which take into account the quality of each event. Thus, our policy of event selection is to select events with minimum quality cuts and evaluate performance in detail.

#### 7.1.1 Photon Cuts

##### 7.1.1.1 Fiducial Volume and Acceptance

The fiducial volume is defined as:

$$|u| < 25, |v| < 71, 0 < w < 38.5cm \quad (7.1)$$

The acceptance is shown in Figure 7.1.

##### 7.1.1.2 Pileup Rejection

Details of pileup elimination is described in Section 5.4.3. In case of pileup events where two peaks of light distribution are identified, we apply an additional cut on these events so that the eliminated energy is positive and no larger than 10% of the total energy.

$$0 < \frac{E_{\gamma}^{normal} - E_{\gamma}^{pileupcorrected}}{E_{\gamma}^{normal}} < 0.1 \quad (7.2)$$

## 7. PERFORMANCE

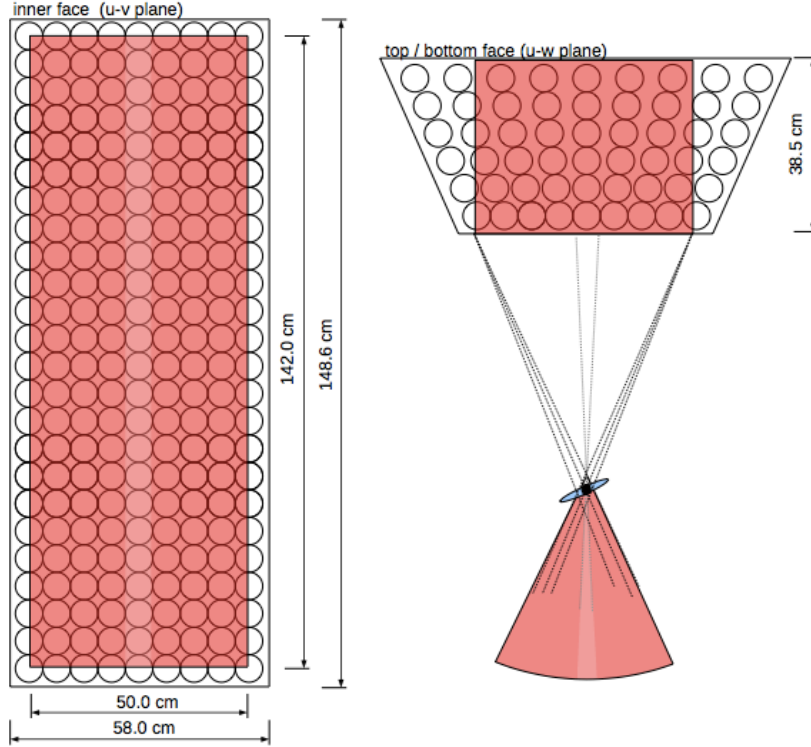


**Figure 7.1:** The accepted regions of the LXe detector are shown in red in the u-v plane on the left and the u-w plane on the right.

where  $E_{\gamma}^{normal}$  is the total deposited energy and  $E_{\gamma}^{pileupcorrected}$  is energy after removing the secondary peak. Pileup events identified only by  $\hat{\chi}_{time}^2$  are also rejected. Figure 7.2 shows the rejected events in red-filled region. The inefficiency by this selection is evaluated to be  $\sim 8\%$ .

### 7.1.1.3 Cosmic Ray Veto

Photons from the stopping target tend to interact close to the inner face and deeper events are more likely to be cosmic rays entering through outer shell. Hence we can make a cut on the ratio between inner face and outer face as well as conversion depth to get rid of these events. The criteria to keep the event is set as

$$(w < 15 \times \frac{N_{inner}}{N_{outer}} + 15) \wedge (w > -400 \times \frac{N_{inner}}{N_{outer}} + 120) \quad (7.3)$$

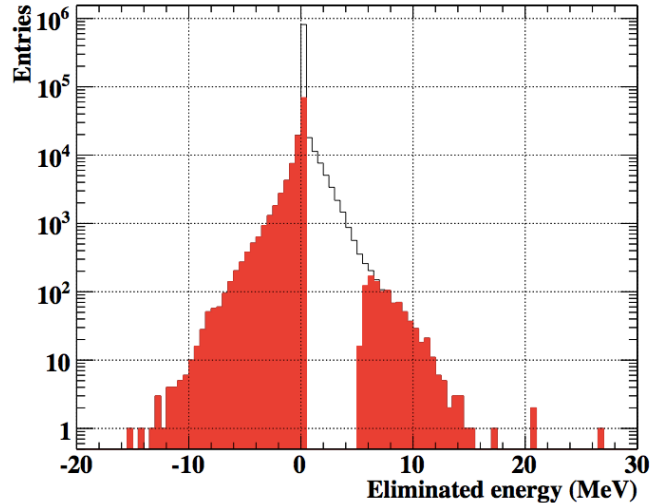


**Figure 7.2:** Distribution of the subtracted energy in the pileup elimination. Red filled entries are rejected by the selection criteria.

where  $w$  is the conversion depth. We apply another cut using information of pulse shape,

$$55 < \text{PulseWidth} < 500 \text{ nsec} \quad (7.4)$$

The remaining contribution of cosmic is about 1% of the total background in the signal region and 56% of cosmic rays are rejected. Figure 7.3 shows the event distribution of measured and MC events.

## 7.1.2 Positron Cuts

### 7.1.2.1 Fiducial Volume

The positron acceptance is defined so that the inverse of the positron direction goes into the gamma-ray detector fiducial volume.

### 7.1.2.2 Drift Chamber Hit Pattern

To select positrons reconstructed with reliable tracking, we have the following requirements: the total number of hits  $\geq 7$ ; the number of chambers that have hits  $\geq 3$ ; the

## 7. PERFORMANCE

---

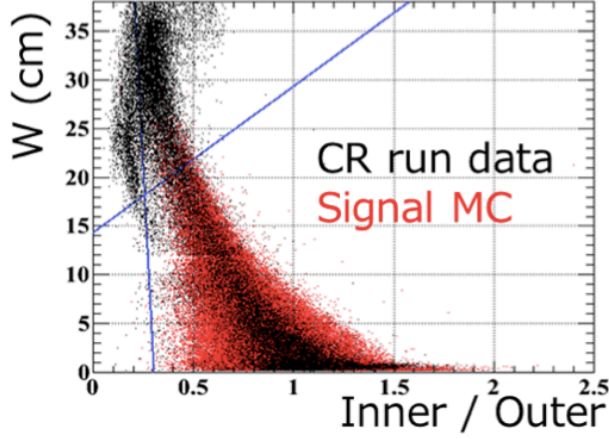


**Figure 7.3:** Cosmic ray cut. Black plot shows the events in the acceptance taken without beam. Red one shows MC signal events. Blue lines show the selection criteria.

span of the track  $\geq 4$  chambers; the number of multi-hit chambers  $\geq 1$ .

### 7.1.2.3 Quality of Track Fit

We apply several criteria on the fitted tracks to select events with good fitting quality. The Kalman filter provides several indicators on the quality of the track fit. One requirement is that the normalized  $\chi^2$  is smaller than 12. Cuts on energy and angle uncertainties are:  $\delta E_e < 1.1$  MeV,  $\delta\theta_e < 0.6^\circ$ , and  $\delta\phi_e < 1.5^\circ$ .

### 7.1.2.4 Vertex Cut

To guarantee that the positron comes from a muon decay on target, we require the reconstructed muon decay vertex to be within an ellipse that excludes the target frame by 5 mm.

### 7.1.2.5 DCH-TIC Matching Cut

To select well-matched events between the drift chamber and timing counter, we apply cuts on the qualities  $|\Delta Z_{DCH-TIC}| < 12$  cm and  $|\Delta r_{DC-TC} - 1.8| < 5$  cm.

### 7.1.2.6 Ghost Track Selection

Because the tracking algorithm attempts to reconstruct all possible tracks in a high rate environment, more than one manifestation of the same track may be identified in a single event. If there are two clusters of hits, it may be possible to place either of them and fit an otherwise identical track. We call these tracks associating with a single positron ghost tracks. A procedure is developed to classify ghost tracks and to select among them. All of the fitted tracks in an event are compared with one another and any two are considered to be ghosts of the same track if the following conditions are met:

1. They both share a common timing counter hit.
2. The number of chambers with at least one hit in common is more than half the total number of hit chambers on the shorter of the two tracks.

Each track in a set of ghost tracks is then ranked to indicate its quality of reconstruction. The rank  $G_{rank}$  is based on the chamber span ( $S$ ) which is the number of chambers that the span of a track covers, and the normalized  $\chi^2$  of track fitting,  $\hat{\chi}^2$ :

$$G_{rank} = \frac{1}{S} + \alpha \hat{\chi}^2 \quad (7.5)$$

$\alpha = 0.025$  is chosen so that the first term dominates the ranking when tracks have similar  $\hat{\chi}^2$  and the second term dominates when tracks have very different  $\hat{\chi}^2$ .

If more than one ghosts of the same track passes the aforementioned cut criteria, the one with the smallest ranking is selected.

The inefficiencies of each cut is summarized in Table 7.1.

## 7.2 Gamma Energy

The energy resolution and scale of the gamma-ray detector are determined at 54.9MeV peak in  $\pi^0$  data (Figure 7.4). The energy peak is estimated with a combination of

## 7. PERFORMANCE

---

Selections	Inefficiency
$\gamma$ Fiducial Volume	3.0%
Pileup Rejection	8%
Cosmic Ray Veto	1%
$e^+$ Fiducial Volume	26.1%
DCH Hit Pattern	8.6%
Track Fit Quality	15.9%
Vertex Cut	15.9%
DCH-TIC Matching	9.2%

**Table 7.1:** A table of inefficiencies for each cut. The inefficiencies are calculated as the fraction of events rejected by making only the cut with respect to making no cuts. The  $\gamma$  acceptance cut inefficiency is calculated when positron cuts, pileup cut, and cosmic ray cut are already applied.

Gaussian function for higher energy part and exponential function for a tail. These two functions are smoothly connected at transition point lower than the peak energy.

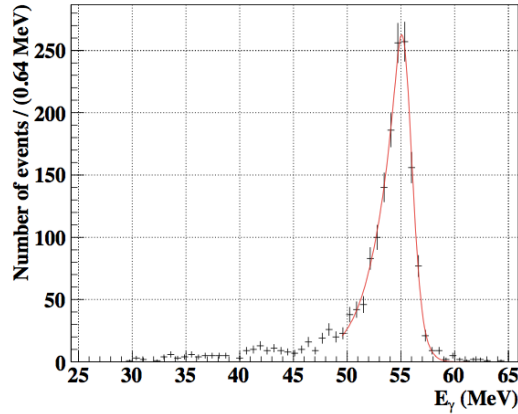


**Figure 7.4:** Energy peak of 54.9 MeV in  $\pi^0$  run.

Since the resolution is position dependent, the response was extracted for each position. Figure 7.5 shows resolution maps for various positions of the gamma ray interaction for  $w \geq 2$  cm. The averaged resolution is  $\sigma_{wp} = 1.9\%$  for  $w \geq 2$  cm. The relative uncertainties of resolution evaluation are estimated to be 10 ~ 14% from the errors of fitting and the variation of the resolutions in close positions. The resolutions

are measured separately for the events with  $w < 2$  cm because the resolution depends heavily on the depth of interaction in shallow region. The averaged resolution for  $w < 2$  cm is 2.4%.

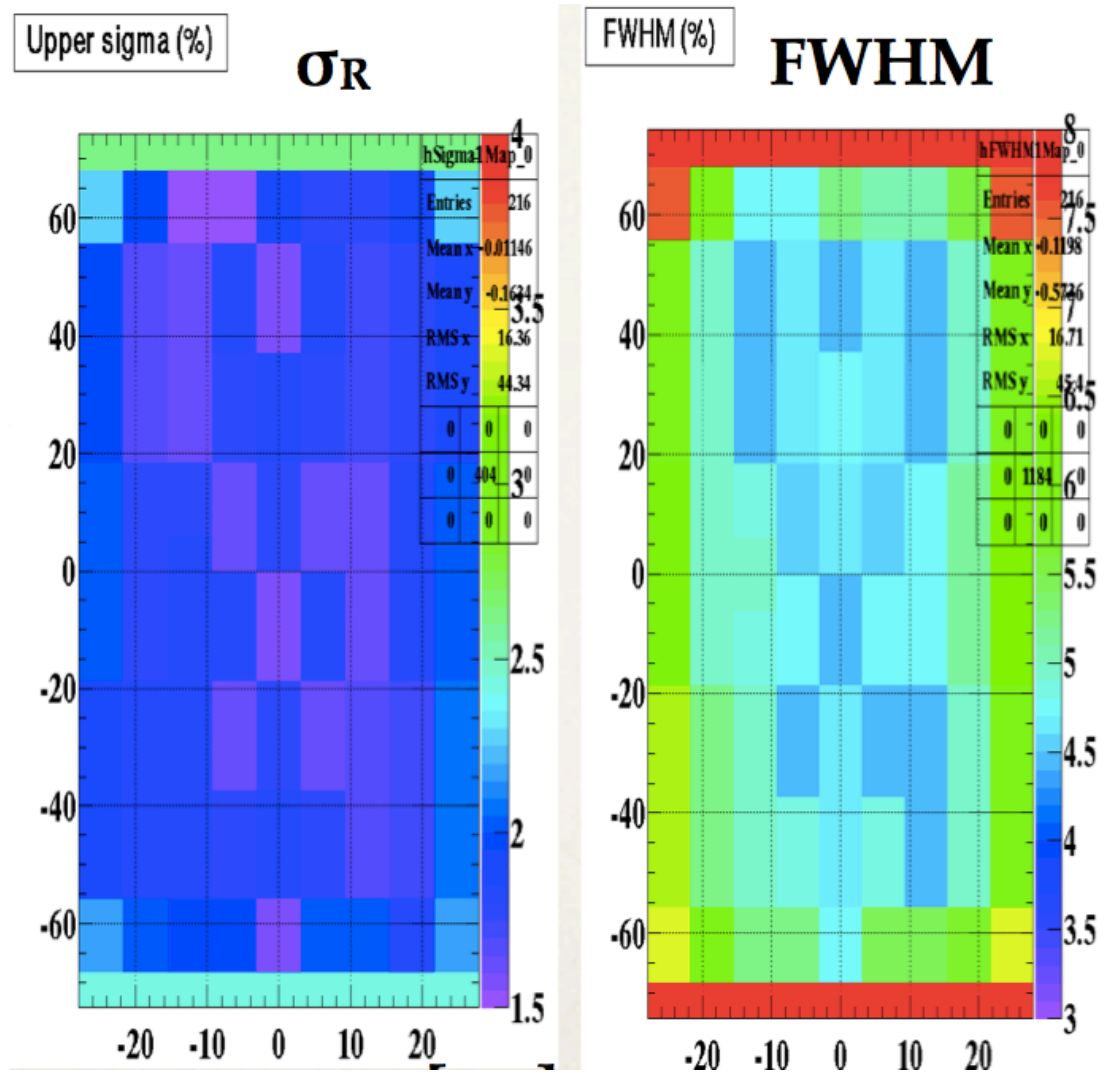


Figure 7.5: Energy resolution at 54.9 MeV on inner face ( $w \geq 2$  cm).

### Systematic Uncertainty on Energy Scale

We calibrate the energy scale of the detector using peaks from  $\pi^0$  decay. Energy scale in 2010 using various calibration methods is shown in Figure 7.6. Sources of

## 7. PERFORMANCE

---

uncertainties come from difference between 55 MeV and 83 MeV peak (0.3%), position dependence (0.3%), gain uncertainty (0.09%) and statistic uncertainty in 55 MeV peak fit (0.03%).

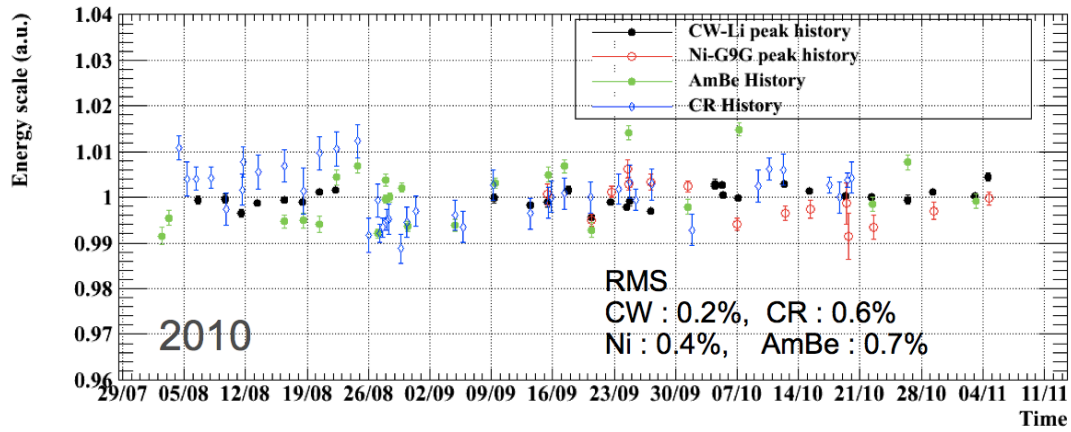


Figure 7.6: Energy Scale.

## 7.3 Positron Energy

We calculate the resolution of positron energy by fitting the energy distribution of normal muon decay,  $\mu^+ \rightarrow e^+ \nu_e \bar{\nu}_\mu$ , with a convolved function of a theoretical prediction in the SM and three Gaussian functions as the resolution contribution of a core and a tail:

$$\text{Probability density}(E_e^{\text{measured}}) = (\text{Michel} * \text{Acceptance})(E_e^{\text{true}}) \otimes \text{Resolution} \quad (7.6)$$

Both the acceptance and resolution functions are based on Monte Carlo simulation. The acceptance function is taken as

$$\text{Acceptance}(E_e^{\text{true}}) = \frac{1 + \text{erf}\left(\frac{E_e^{\text{true}} - \mu_{\text{acc}}}{\sqrt{2}\sigma_{\text{acc}}}\right)}{2} \quad (7.7)$$

and the resolution function is assumed to be a double Gaussian. The parameters are extracted from the fit, as shown in Figure 7.7. This gives an average resolution of  $\sigma_{E_e} = 330 \pm 16$  keV in the core (82% of the events) and  $\sigma_{E_e} = 1.13 \pm 0.12$  MeV in the tail. There is also a 60 keV systematic underestimation of the energy, which is associated with a 25 keV uncertainty from Monte Carlo.

A complementary approach to measure the positron energy resolution is using double turn events. Figure 7.8 shows the energy difference between the two turns, which is fit to the convolution of a double Gaussian function with itself. This gives an average resolution of  $\sigma_{E_e} = 330$  keV in the core (79% of the events) and  $\sigma_{E_e} = 1.56$  MeV in the tail, which are consistent with the results obtained from the fit of Michel spectrum. There is a systematic offset of 108 keV between the energies of the two turns as the energy of the first turn is systematically larger than the energy of the second turn.

## 7.4 Relative Angle

### 7.4.1 Positron Emission Angle

The resolutions of emission angle  $\theta_e$  and  $\phi_e$  are taken from data by using events that where a positron makes two turns in the drift chamber. The resolution in each turn is assumed to be the same and these distributions are fit to the convolution of a sum

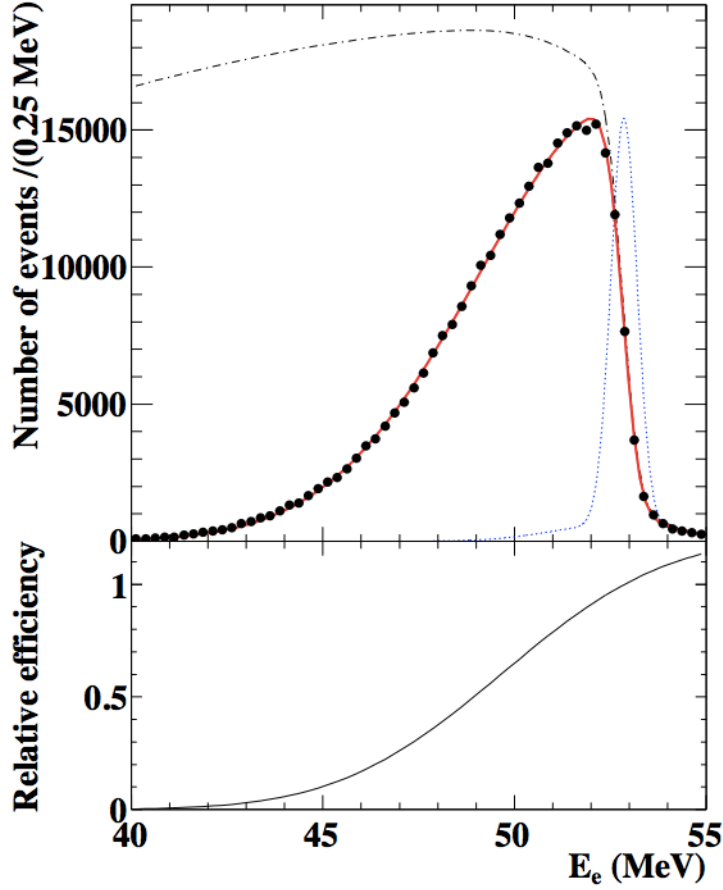


**Figure 7.7:** Fitting of a Michel spectrum. The dashed black line is the theoretical spectrum and the dashed blue line is the resolution function. The acceptance curve is shown in the bottom plot.

of two Gaussians with itself. The resolutions are Vertex  $z/y = 2.0/1.1$  mm,  $\sigma_{\theta_e} = 11$  mrad, and  $\sigma_{\phi_e} = 7.2$  mrad.

#### 7.4.2 Muon Decay Vertex

The position of the decay vertex is determined by the extrapolated positron tracking. We can estimate the position resolution with holes on the target. The vertex resolutions in 2010 along minor axis(Z) and major axis on the plane(Y) are  $\sigma_Z = 3.78$  mm,  $\sigma_Y^{core} = 0.97$  mm,  $\sigma_Y^{tail} = 3.8$  mm.

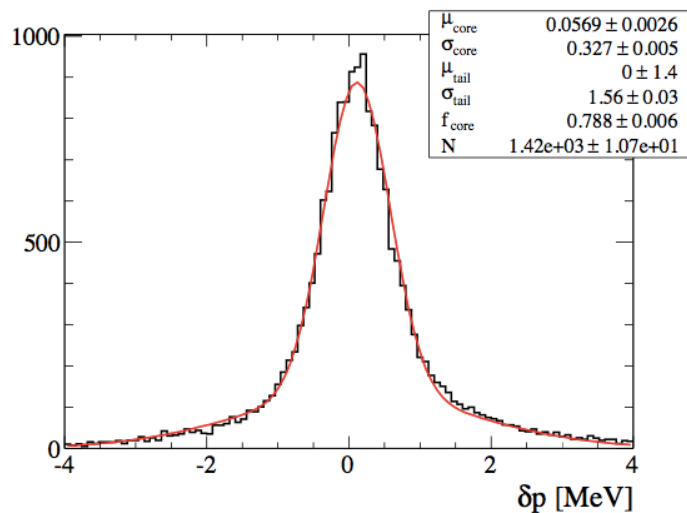


**Figure 7.8:** A fit to the distribution of energy difference between two turns.

### 7.4.3 Gamma ray Position

We measured position with CW run in 2010. Several small lead cubes (approximately  $15 \times 15 \times 13$  mm) were put in front of the LXe detector, as pictured in Figure 7.9.

The resolutions are  $\sigma_{u,v} = 5$  mm,  $\sigma_w = 6$ mm.

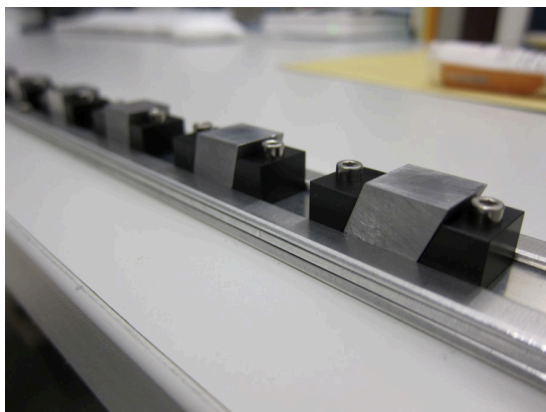


**Figure 7.9:** Lead cubes and the support.

## 7. PERFORMANCE

---

### 7.4.4 Combined Resolution

The resolutions of relative angle in  $\theta$  and  $\phi$  directions were then obtained by combining the angular resolutions of the two particles. They are evaluated to be  $\sigma_{\theta_{e\gamma}} = 17.1$  mrad and  $\sigma_{\phi_{e\gamma}} = 14.0$  mrad.

## 7.5 Relative Timing

### 7.5.1 Positron Time

We measure the resolutions of the timing counter bars by looking at the distributions of time difference between two consecutive bar hits. The width of the time difference distribution of the two hits gives the time resolution. For a single bar resolution, the width is divided by squared root of two assuming that the two have the same resolution. The average resolution is 75 ps. Path length and DRS jitters also contribute to the performance.

### 7.5.2 Gamma-ray Time

#### Intrinsic Resolution

In order to measure the intrinsic time resolution of gamma-ray detector, we divide PMTs into two groups, even and odd groups, as shown in figure 7.10. The intrinsic time resolution is evaluated by the distribution of half of time difference between the two reconstructed time,

$$\frac{\Delta t^{int}}{2} = \frac{t_{odd} - t_{even}}{2} \quad (7.8)$$

The intrinsic resolution proportional to  $\sqrt{E}$  and dominated by photoelectronic statistics. It is about 36.4 ps at 55 MeV and 28.4 ps at 83 MeV.

#### Practical Resolution

We measure the practical time resolution of gamma ray detector using  $\pi^0 \rightarrow \gamma\gamma$  data with scintillation counters that were mounted on the NaI detector as a reference counter.

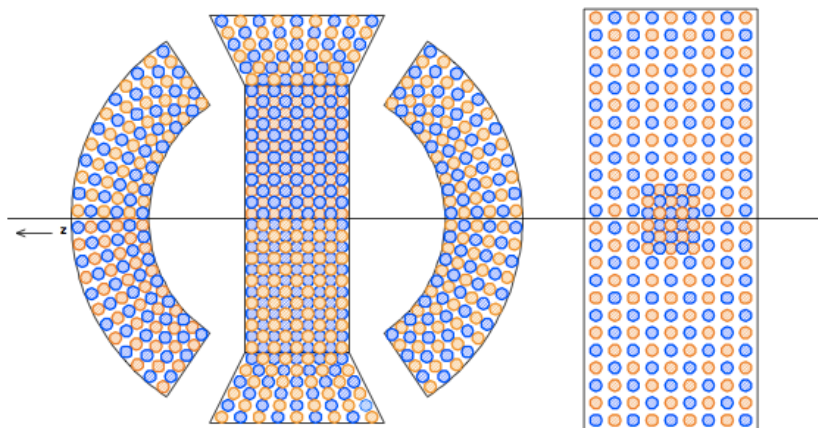


**Figure 7.10:** PMT grouping. Blue circles belong to the 'odd' group while orange circles belong to the 'even' group.

Figure 7.11 shows the distribution of the time difference between the 55MeV  $\gamma$  ray at the gamma-ray detector and the 83MeV one at the reference counter,

$$\Delta t^{abs} = t_{\gamma} - t_{ref} \quad (7.9)$$

The resolutions are 119ps at 55 MeV, which includes contributions from beam spread (58 ps), resolution of the reference counter (81 ps), and time resolution of LXe. By subtracting the other elements, we can estimate the time resolution of LXe to be  $\sigma_{XEC} = 67$  ps. This includes intrinsic resolution, time-of-flight (20 ps), contribution from DRS (24 ps) and effects of position uncertainty and shower fluctuation.

### 7.5.3 Gamma-Positron Relative Time

Radiative muon decays provide a means to measure the relative timing resolution under the same experimental conditions of a signal. The time resolution from radiative decay includes all contributions from the LXe detector, positron tracking and electronics. Figure 7.12 shows the peak in  $E_{\gamma}$  sideband in a range of  $50MeV \leq E_e \leq 55MeV$ ,  $40MeV \leq E_{\gamma} \leq 48MeV$  and within 300 mrad opening angle. The peak is fitted with double Gaussian and the resolution is  $\sigma_{e\gamma} = 122$  ps.

## 7. PERFORMANCE

---

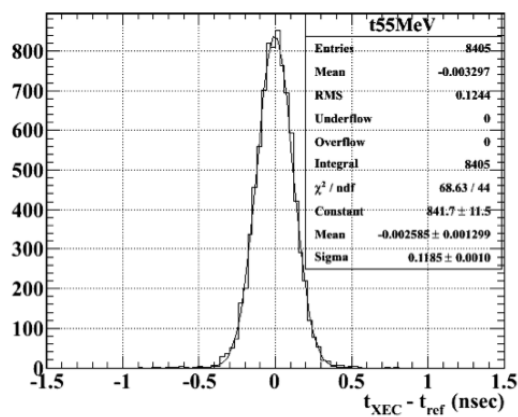


Figure 7.11: timing difference between LXe detector and reference counter

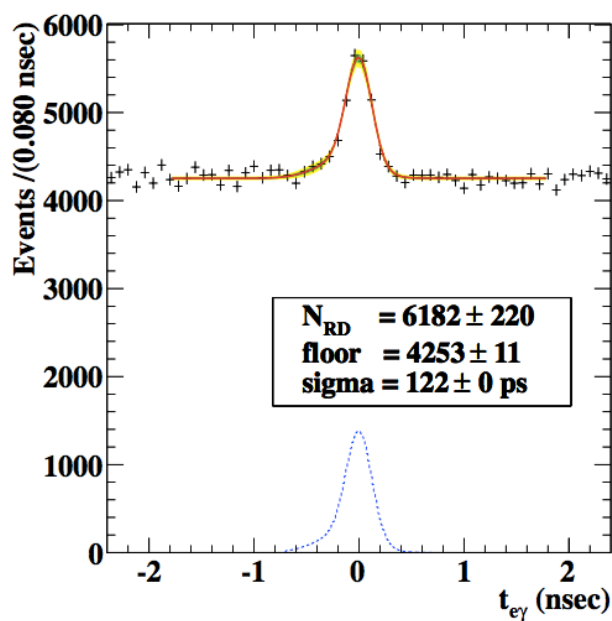


Figure 7.12: Time difference between positron and gamma ray in 2010.

## 7.6 Efficiency

### 7.6.1 Positron Detection Efficiency

For normalizing purpose, the absolute positron detection efficiency is not needed. Only the ratio of signal positron to Michel positron detection efficiency is required. This is calculated by evaluating the fitted acceptance function at the signal energy in Michel spectrum and dividing it with weighted average of the acceptance function in the interval  $50 < E_e < 52.8$  MeV. The uncertainty is estimated by refitting the Michel spectrum with Gaussian and recalculating the efficiency ratio. The result is  $\epsilon_{e^+} = 34\%$ .

The positron detection efficiency is actually the product of the drift chamber detection efficiency and the conditional timing counter detection efficiency given a reconstructed positron. The conditional timing counter efficiency can be measured using data from DCH-self trigger and selecting events with a positron in the drift chamber passing the drift chamber-related selection cuts.

### 7.6.2 Gamma ray Efficiency

Gamma ray detection efficiency is a crucial part of the LXe detector performance and is required for normalizing the experiment. Inefficiency comes from several sources: failure to penetrate the magnet wall and cryostat, pile-up cuts and energy cuts. The detection efficiency is estimated with signal Monte Carlo. It is defined as the conditional probability to reconstruct a signal photon that passes energy and pile-up cuts, given a reconstructed signal positron. The uncertainty is measured using NaI self trigger data in  $\pi^0$  run. We can get the condition that a photon around 55 MeV is emitted to the LXe detector by tagging a photon around 83 MeV.

We start by counting number of events in low energy part, where effects of pileup and AIF is smaller. We calculate the efficiency by dividing the number of signal events mixed with pileup gamma rays with the number of radiative decay events mixed with pileup gamma rays. Energy cuts  $48 \text{ MeV} < E < 58 \text{ MeV}$  are applied to both counts as well as acceptance cuts. The analysis efficiency is estimated to be 91.1%. The detection efficiency which is the weighted average of efficiencies taking into account

## 7. PERFORMANCE

---

the angle distribution of positron detection, is estimated to be 64.7%. Thus the conditional probability to detect and reconstruct a photon once a positron is detected, is  $64.7\% \times 91.1\% = (59 \pm 3)\%$ .

### 7.7 Summary of Performance

The detector performance in 2010 is summarized in Table 7.2.

Gamma energy (%)	1.9 ( $w > 2\text{cm}$ ), 2.4 ( $w < 2\text{cm}$ )
Gamma timing (ps)	67
Gamma position (mm)	5 (u,v)/6(w)
Positron timing (ps)	107
Positron energy (MeV)	0.32 (core 79%)
Positron angle (mrad)	7.2 ( $\phi$ , core), 11.0 ( $\theta$ )
Vertex position (mm)	2.0 (Z), 1.1 (Y)
Positron-gamma timing (ps)	122(core)
Gamma efficiency (%)	59
Positron efficiency (%)	34
Trigger efficiency(%)	92
Positron-gamma angle (mrad)	14.0 ( $\phi$ , core), 17.1 ( $\theta$ )
Stopping $\mu$ rate	$2.9 \times 10^{-7} s^{-1}$
DAQ time/Real time	56 days/67days
Total $\mu$ stops on target	$1.1 \times 10^{14}$
Data statistics (k-factor)	$2.1 \times 10^{12}$

**Table 7.2:** Performance in 2010.

# 8

## Improvements for 2010 Data

For the analysis of 2010 data, we improved several aspects of calibration and analysis such as detector alignment, implementation of correlations in position observables, improved magnetic field map and improved likelihood analysis. Such improvements were subsequently also applied to the 2009 data.

### 8.1 Alignment

#### 8.1.1 DC Alignment

The alignment procedure for drift chamber consists of two parts, a geometrical alignment and a software alignment using cosmic rays and Michel positrons. First, the position of the drift chamber is measured by an optical survey with the help of reference markers on each module with a precision of 0.2 mm. This allows the determination of the wire positions in the absolute coordinate system. For a better accuracy, a track-based alignment procedure consisting of three steps was developed, based on the Millipede method[63]. The first step is the internal alignment of drift chamber modules, which is done by recording cosmic ray events without the COBRA magnetic field. The displacement of each module from the initial position are obtained with an accuracy of  $150\mu\text{m}$ . The second step is placing the obtained frame in the spectrometer with a fine-tuned DC-target-COBRA position, using a sample of double-turn Michel positron tracks in the magnet volume. The third step is the

## 8. IMPROVEMENTS FOR 2010 DATA

---

alignment of the spectrometer with respect to the LXe detector.

### 8.1.2 Relative Alignment Between DC and LXe

The relative alignment of the sub-detectors is based on the initial alignment of the LXe detector on the detector platform and the position measurements using cosmic ray, CW and AmBe data. Two plates with a reference hole are installed on the inner support structure of the LXe detector and the detector position is adjusted through the position of the hole center. The LXe detector is installed at  $(x, y, z) = (724\text{mm}, 1505 \pm 1.5\text{mm}, 0\text{mm})$ , where  $x$  is the distance from the beamline in parallel,  $y$  is the height of the detector, and  $z$  is the axis along the beamline. There is a systematic uncertainty of  $\pm 1.5$  mm for the placed position.

#### Cosmic Ray

Cosmic rays penetrating both LXe detector and the drift chamber were used to measure their relative position. The data are taken without COBRA magnetic field. By extrapolating the trajectory in drift chamber to the inner face of XEC, we can reconstruct the entrance point, which is then compared with the reconstructed position measured by LXe.

The trajectory of a cosmic ray is reconstructed using hits in drift chamber. The reconstructed incident point is defined as  $(z_{track}, v_{track})$  and the incident angles are  $\eta_{xy}$  and  $\eta_{zx}$ , as shown in Figure 8.1. The results are  $\Delta z = z_{rec} - z_{exp} = (-6.1 \pm -0.7)$  mm,  $\Delta v = -1.9 \pm 0.7$  mm.

#### CW

CW data are taken with several small lead cubes in front of the LXe detector. CW data with a LiB target were taken with dedicated trigger patches as shown in Figure 8.2. An average of differences between measured and reconstructed  $z$ ,  $\Delta z = z_{rec} - z_{exp}$ , using six bars is  $-7.3 \pm 1.4$  mm. An average of  $\Delta\phi$  using Bar-C is  $0.3 \pm 1.1$  mrad.

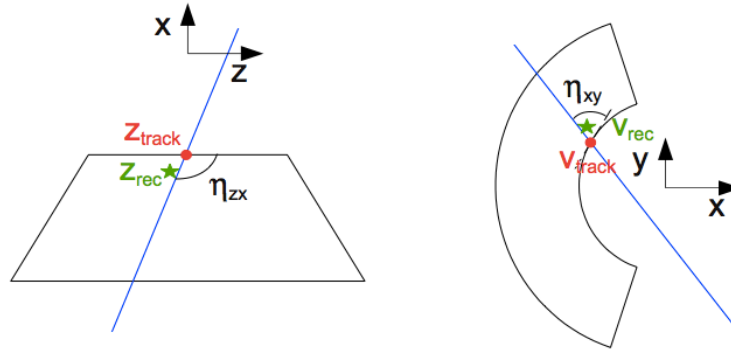


**Figure 8.1:** Definition of variables used in CR analysis. Blue lines are the reconstructed trajectory by DCH.

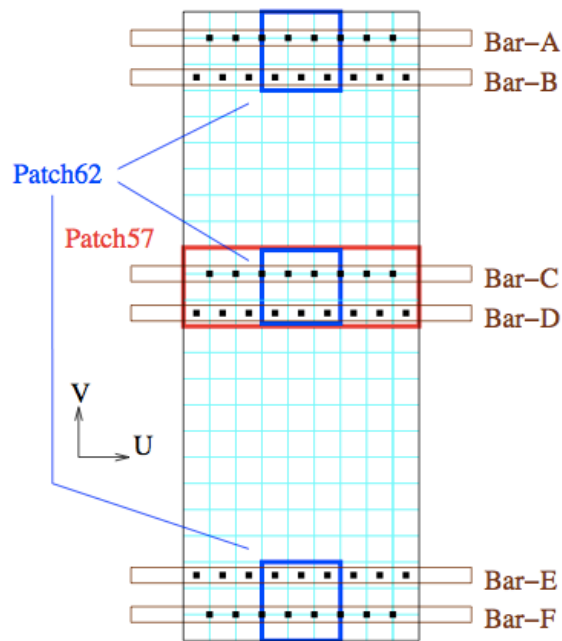


**Figure 8.2:** Trigger patches used in CW runs.

## AmBe

An AmBe source is placed in front of the LXe detector to calculate its absolute position. The reconstructed  $z$ -position of 4.4 MeV  $\gamma$  event is compared with the source position which is measured by an optical survey. The gamma ray from the AmBe

## 8. IMPROVEMENTS FOR 2010 DATA

---

source is collimated with a 20 mm-thick lead collimator with a 10mm  $\phi$  hole. The measurements are taken in front of two PMTs at  $z = 0$  and different  $v$ -positions. The source is moved along  $z$  direction for each measurement. The difference between the reconstructed and the source  $z$  positions is  $-5.5 \pm 1.8$  mm.

### Combining the results

A weighted mean was taken to get a combination of the results. The uncertainty of the drift chamber position is added to that of CW and AmBe results. There is no significant shift in  $\sigma$  however the same uncertainty is applied. The results of the relative alignment are  $\Delta z = -6.2 \pm 2.3$  mm and  $\Delta\phi = 0 \pm 3.4$  mrad. The uncertainty of relative angle(3.4 mrad) is improved compared to 2009 (7.5 mrad).

### 8.1.3 Target Alignment

The alignment of the target is confirmed by the reconstructed positions of several holes on the target, as shown in Figure 8.3. When misalignment happens, the reconstructed position would depend on the incident angle of the positron track as illustrated in Figure 8.4.

The result confirmed the position of optical survey is correct.



Figure 8.3: Target markers.

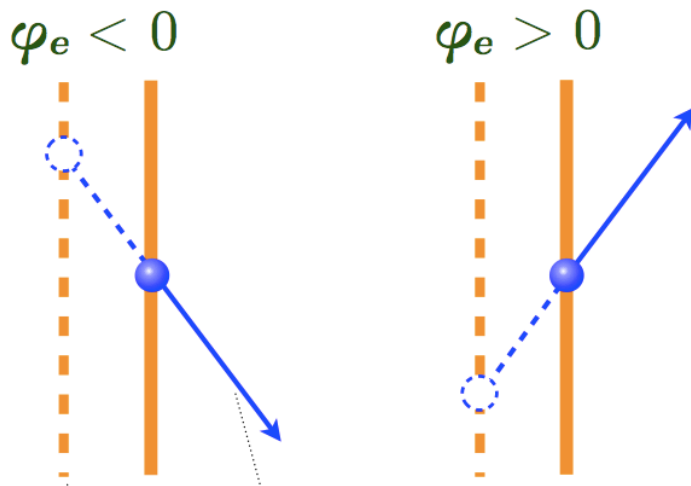


**Figure 8.4:** Position of the holes when misalignment happens. Dotted line shows the assumed target and solid line is the actual target.

## 8.2 Correlations

In principle no strong correlations among the positron variables are expected inside the spectrometer. However since all positrons come from the target plane and the target thickness is  $205 \mu\text{m}$ , it introduces a constraint in track reconstruction, thus creates correlations among all signal positron variables.

To evaluate the correlations introduced by the target plane, we studied how infinitesimal changes of each variable influence the others. We assume the positron track is helicoidal. For the extraction of the  $\delta\phi_e$  vs  $\delta E$  and  $\delta Y$  vs  $\delta E$  correlations, the track is assumed to be a circle when projected on the transverse plane, as shown in Figure 8.5. Target intersection with the transverse plane passing from the muon decay point  $V = (X, Y)$  is shown in red. For the extraction of the  $\delta Z$  vs  $\delta\phi_e$ , the track can be projected on a plane that is parallel to the  $Z$ -axis and tangent to the track helix at the muon vertex, as shown in Fig 8.6.

From this geometrical model we can establish the following relations among infinitesimal changes at the target.

$$\delta\phi_e = -2 \tan \phi \frac{\delta R}{R} = -2 \tan \phi \frac{\delta E}{E} \quad (8.1)$$

## 8. IMPROVEMENTS FOR 2010 DATA

---

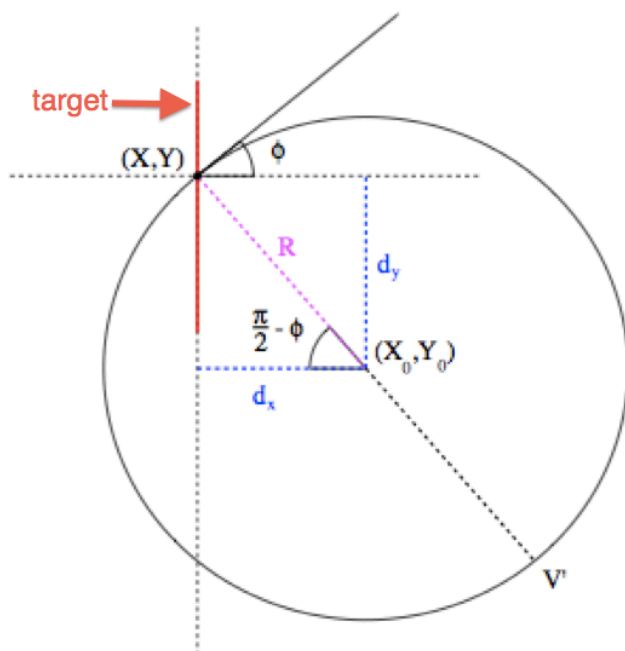


**Figure 8.5:** Extraction of the  $\delta\phi_e$  vs  $\delta E$  and  $\delta Y$  vs  $\delta E$  correlations.

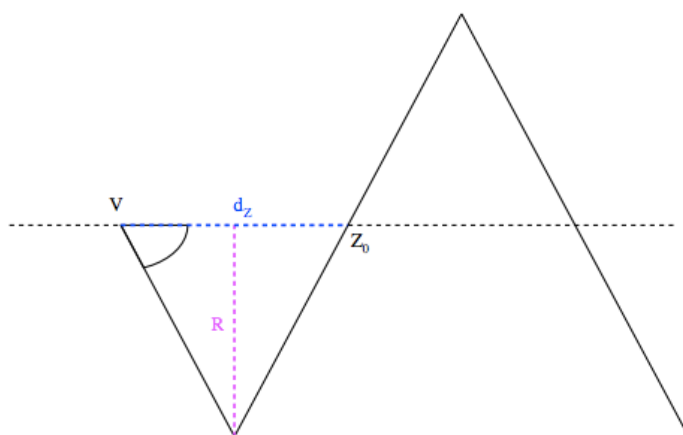


**Figure 8.6:** Extraction of the  $\delta Z$  vs  $\delta\phi_e$  and  $\delta Z$  vs  $\delta E$  correlations.

$$\delta Y = 2\delta R \cos \phi_e + R \sin \phi_e \delta \phi_e = \frac{2R}{\cos \phi_e} \frac{\delta E}{E} \quad (8.2)$$

$$\delta Z = \frac{2R}{\sin^2 \phi_e} \delta \phi_e - 2R \cot \phi_e \frac{\delta E}{E} \quad (8.3)$$

In order to evaluate resolutions and correlations, we use a double turn tracks method where tracks which make two turns inside the drift chambers are used and each turn is reconstructed as an independent pseudo-track. Each pseudo-track is projected onto a plane with the same inclination as the target, as shown in Figure 8.7. The difference of their spatial and directional components is used to measure resolutions.

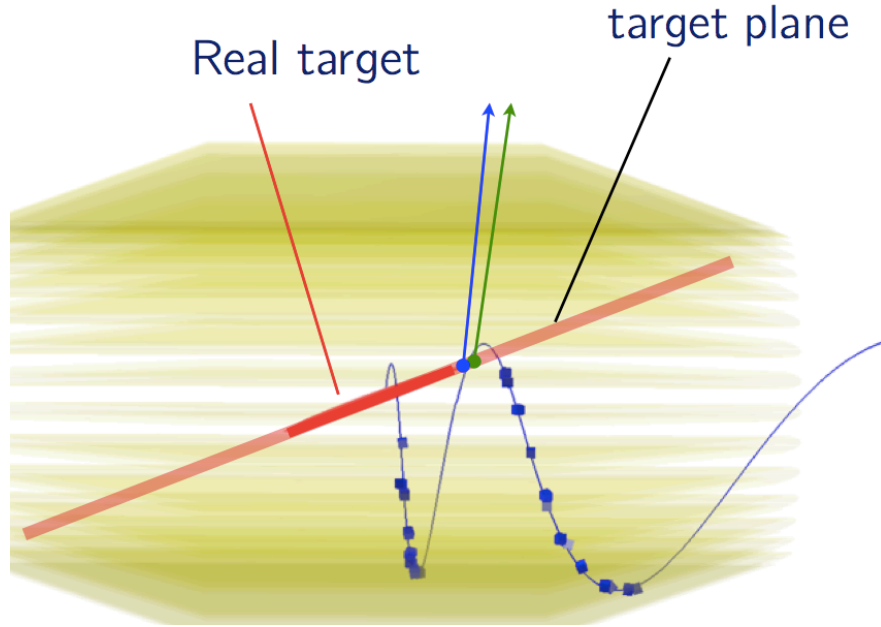


**Figure 8.7:** Illustration of the double turn track method.

We define  $\Delta x^{TURN}$  where  $x = \theta_e, \phi_e, E, Y, Z$  as

$$\Delta x^{TURN} = x^{TURN_0} - x^{TURN_1} \quad (8.4)$$

where  $x^{TURN_0}$  is the value of variable  $x$  for the first turn pseudo-track and  $x^{TURN_1}$  for the second turn pseudo-track. Similarly in MC we can define the true resolution on  $x$  as  $\Delta x^{TRUE}$

$$\Delta x^{TRUE} = x^{MEASURED} - x^{TRUE} \quad (8.5)$$

## 8. IMPROVEMENTS FOR 2010 DATA

---

where  $x^{MEASURED}$  is the measured value of  $x$  and  $x^{TRUE}$  is the true value of  $x$  generated in MC.

For likelihood analysis, correlations are more accurately implemented in signal PDF. In 2009,  $\phi_E$  and  $E_\gamma$  correlation was incorporated as a systematic error of 50% due to lack of method to measure the correlations from data. This corresponds to 0.09 in RMS of difference of likelihood ratio compared to 0.02 in 2010. The details of systematics are described in Chapter 9.5.

### 8.3 Magnetic Field Map

A reconstructed field is used for 2010 data to minimize the uncertainty due to misalignment of Hall sensors.

The magnetic field was measured in 2006 with a commercial three-axis Hall probe. It has three orthogonally aligned Hall sensors on a wagon which moves along  $z$ ,  $r$  and  $\phi$ . The probe was aligned so that it can measure  $B_z$ ,  $B_r$ , and  $B_\phi$  individually. Possible measurement errors come from limited readout accuracy of the Hall sensor and the positioning of the Hall probe, and misalignment of the field measuring machine, the moving wagon, or the Hall probe.

The Hall sensors were calibrated prior to measurement at a precision of 0.05%. The planar Hall effect is less than 0.2% and the effect of the temperature coefficient of the Hall sensor is estimated to be less than 0.6%. The field measuring machine, the moving wagon and the Hall probe are aligned at a precision of a few mrad using the laser tracker. The precision of the relative angle alignment of the three Hall sensors is  $\pm 9$  mrad. Since a small misalignment could cause a large effect on  $B_r$  and  $B_\phi$  from the main component  $B_z$ , only  $B_z$  is used to minimize the influence of misalignment while  $B_r$  and  $B_\phi$  are calculated from Maxwell equation.

The global offset of the field measuring machine from the theoretical magnetic center is measured by comparing the measured  $B_z$  with the calculation. By minimizing the difference at the grid points, the offset is estimated to be  $(x_0, y_0, z_0) = (+0.5 \text{ mm}, -2.9 \text{ mm}, -0.6 \text{ mm})$ .

After the global offset correction,  $B_r$  and  $B_\phi$  are calculated from the measured  $B_z$

using Maxwell equations.

## 8.4 Likelihood Analysis

To improve likelihood analysis, constraints from sideband data are applied and profile likelihood is used, which will be discussed in Chapter 9.

## 8.5 Update on 2009 Result

All the improvements described in the preceding sections were also studied and applied to the 2009 data. The obtained performance in 2009 is summarized in Table 8.1.

$\sigma_{E_\gamma}(\%)$	$\sigma_{(u,v,w)}(mm)$	$\epsilon_\gamma$	$\sigma_{E_e}(\%)$	$\sigma_{\phi_e}(mrad)$	$\sigma_{\theta_e}(mrad)$	Vertex $\sigma_{z,y}(mm)$	$\epsilon_e$	$\sigma_{te\gamma}(ps)$	$\epsilon_{trigger}$
2.1	5,6	0.58	0.74	7.1	11.2	3.4,3.4	0.4	142	0.84

**Table 8.1:** Resolution in 2009.

The preliminary result of the maximum likelihood fit of the 2009 data before applying the improvements was

$$(N_{sig}, N_{RD}, N_{BG}) = (3.0^{+6.9}, 35^{+24}_{-22}, 332^{+38}_{-36}), N_{obs} = 370 \quad (8.6)$$

Figure 8.8 shows the distribution of each observable with average PDFs scaled with the best fit numbers of each type. The estimated sensitivity and the obtained upper limit of branching ratio in the preliminary analysis are

$$S_{2009} = 6.1 \times 10^{-12} \quad (8.7)$$

$$Br(\mu^+ \rightarrow e^+\gamma) < 1.5 \times 10^{-11} \text{ at } 90\% \text{ C.L.} \quad (8.8)$$

The event distributions are shown in Figure 8.9. The events are labeled with the order of the likelihood ratio defined as  $S/(S + R + B)$ .

## 8. IMPROVEMENTS FOR 2010 DATA

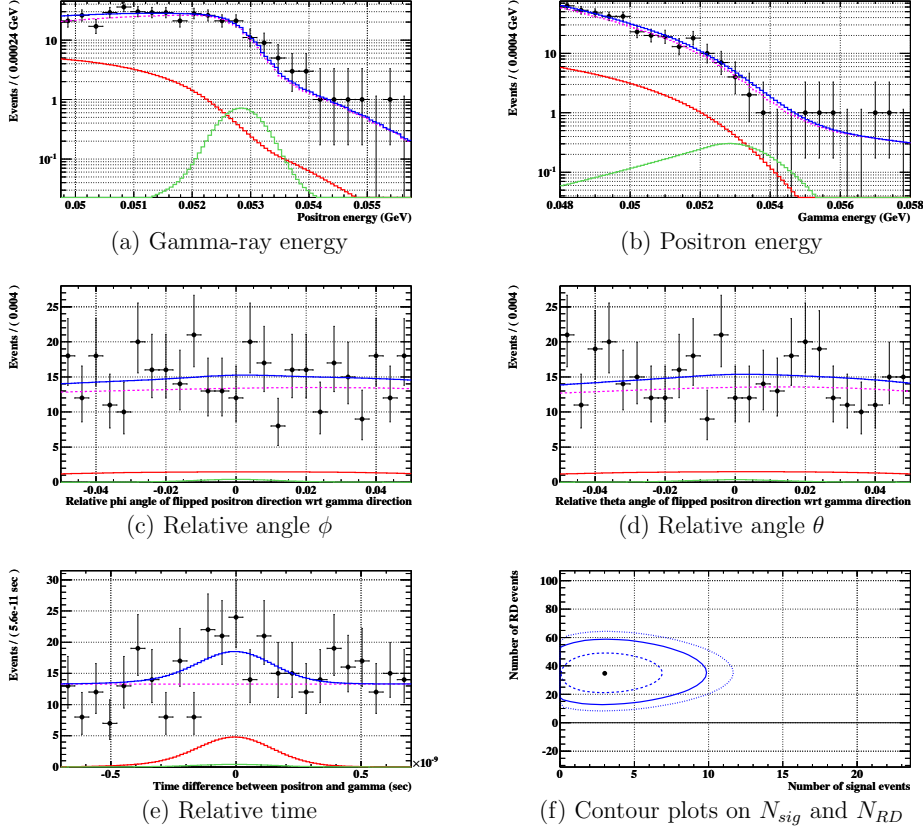


**Figure 8.8:** Preliminary result of 2009 data before applying the improvements. (a)-(e) show the summed PDFs weighted with best fit values of each types. The blue lines are total sums of all PDFs. The green, red, and magenta lines show the signal, RD, and background PDF respectively. The black dots are the best fit values. (f) shows the contour plot on  $N_{sig} - N_{RD}$ . The dashed, solid, and dotted lines show contours of the likelihood function at 1, 1.645, 2 sigma respectively[1][2][3].

After the improvements in calibration and analysis methods discussed above are applied, the estimated sensitivity was improved to be  $3.3 \times 10^{-12}$ , mainly thanks to the profile likelihood analysis, as shown in Figure 9.19.

The best fit result after the improvements is

$$(N_{sig}, N_{RD}, N_{BG}) = (3.4^{+6.6}_{-4.4}, 26.9^{+4.5}_{-4.5}, 273.1^{+12.3}_{-12.3}), N_{obs} = 311 \quad (8.9)$$

Figure 9.22 shows the distribution of each observable with average PDFs scaled

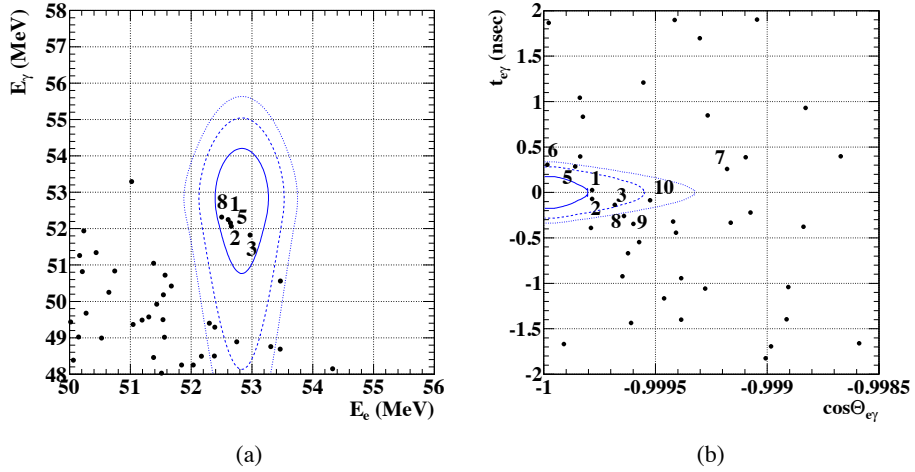


**Figure 8.9:** Event distributions in the analysis region.[2][1][3] The contours show 1, 1.64 and  $2\sigma$  regions of the signal PDF, which cover 39, 74 and 87% of probability, respectively. In the left plot, selections in  $t_{e\gamma}$  and  $\theta_{e\gamma}$ , each of which is 90% efficient on the signal, are applied. In the right plot, a selection in  $E_e$  (90% on the signal) and a selection in  $E_\gamma$  (73% on the signal) are applied.

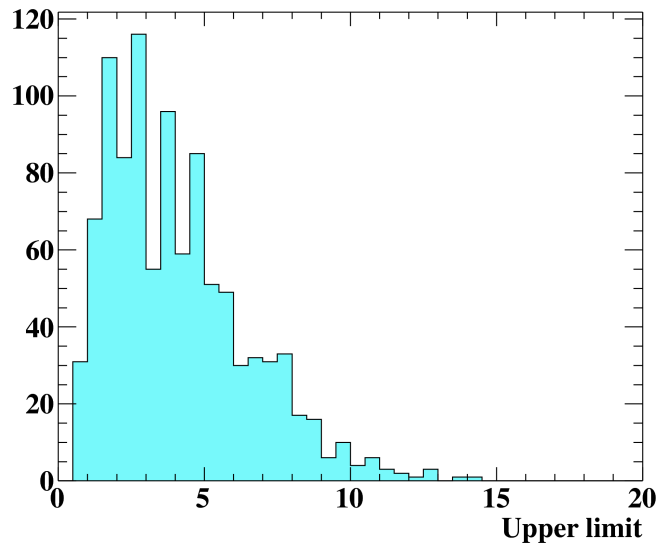


**Figure 8.10:** Updated result of sensitivity in 2009.

with the best fit numbers of each type.

## 8. IMPROVEMENTS FOR 2010 DATA

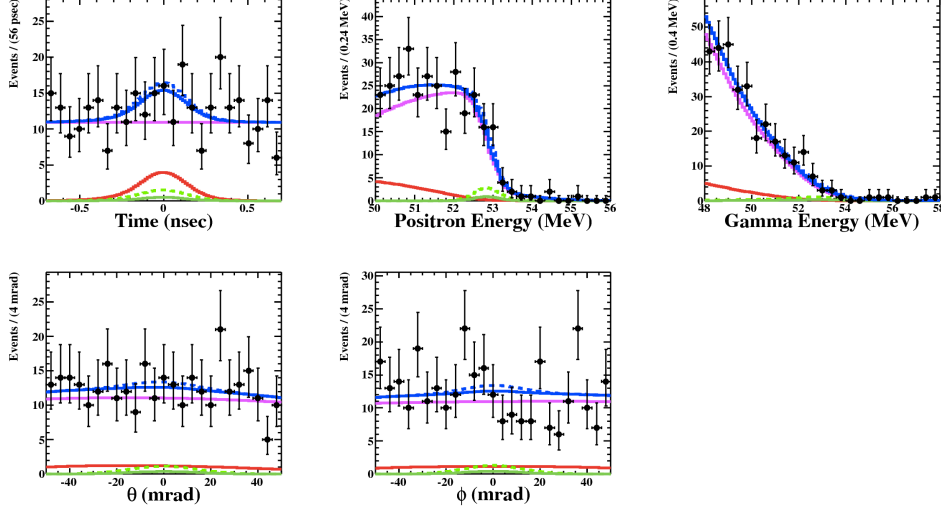


**Figure 8.11:** Updated result of 2009 data. The green, red, magenta and blue lines show the signal, RD, background and total sums of PDF respectively.

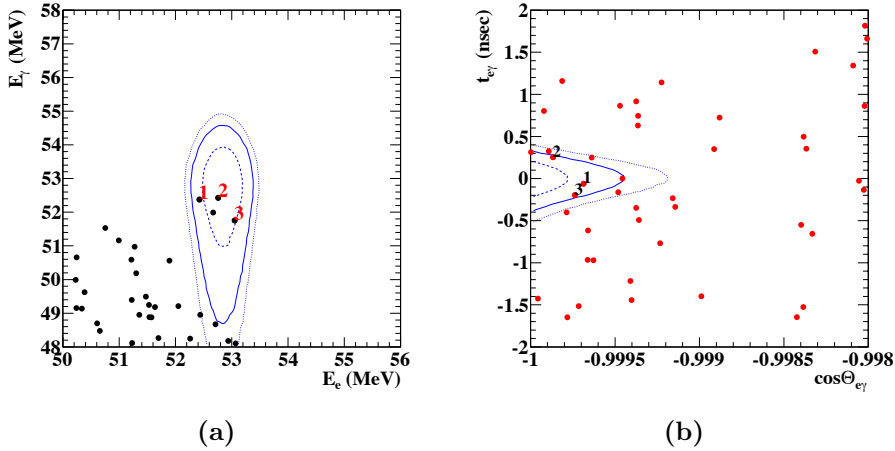


**Figure 8.12:** Updated event distributions in the analysis region for 2009 data. In the left plot, selections in  $t_{e\gamma}$  and  $\theta_{e\gamma}$ , each of which is 90% efficient on the signal, are applied ( $|t_{e\gamma}| < 0.278$  nsec,  $|\theta_{e\gamma}| > 178.34^\circ$ ). In the right plot, a selection in  $E_e$  (90% on the signal) and a selection in  $E_\gamma$  (73% on the signal) are applied ( $51 < E_\gamma < 55$  MeV,  $52.34 < E_e < 55$  MeV).

As shown in Figure 9.26, an excess of events around the signal region still remain. However the sensitivity is much improved compared to the preliminary result. The obtained confidence level curve is shown in Figure 8.13 and the lower and upper limit

in number of signals and branching ratio are summarized in Table 8.2.

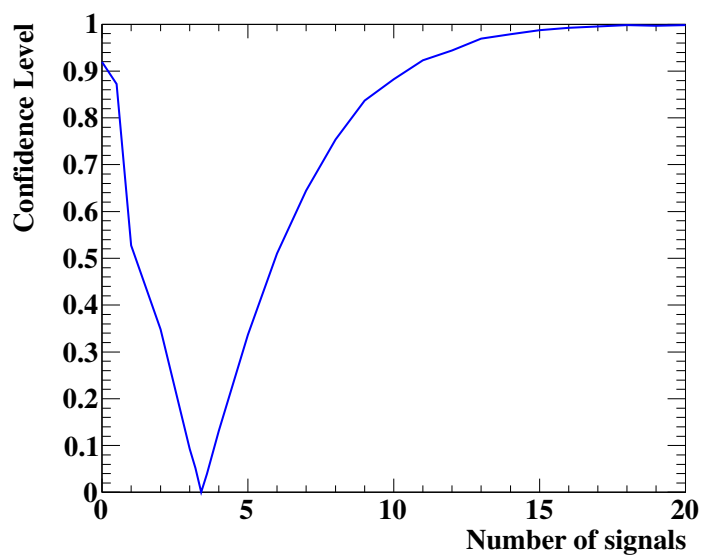


Figure 8.13: Confidence level curve in 2009 data.

	Best fit	LL(90% C.L.)	ULL(90% C.L.)	UL(95% C.L.)	CL@0
$N_{sig}$	3.4	0.2(0.2)	10.4(10.1)	11.9(N/A)	0.92(0.92)
BR	$3.2 \times 10^{-12}$	$1.7 \times 10^{-13}$ ( $1.7 \times 10^{-13}$ )	$9.6 \times 10^{-12}$ ( $9.4 \times 10^{-12}$ )	$1.1 \times 10^{-11}$ (N/A)	0.92(0.92)

Table 8.2: Confidence intervals on 2009 data.

## 8. IMPROVEMENTS FOR 2010 DATA

---

# 9

## Physics Analysis on Data 2010

### 9.1 Overview of Analysis

This chapter shows the analysis to calculate the branching ratio of  $\mu^+ \rightarrow e^+\gamma$  from 2010 data. We perform a maximum likelihood analysis to extract the number of  $\mu^+ \rightarrow e^+\gamma$  events in the data sample. A likelihood function is constructed from probability density functions (PDFs) of distributions in  $E_e$ ,  $E_\gamma$ ,  $t_{e\gamma}$ ,  $\theta_{e\gamma}$  and  $\phi_{e\gamma}$  for signal, radiative muon decay, and accidental background events. A confidence interval of the measured branching ratio is then estimated with a frequentist approach. The sensitivity with null-signal assumption is calculated by averaging the branching ratio upper limits of the generated experiments. To avoid introducing bias in analysis, we blind the region around  $\mu^+ \rightarrow e^+\gamma$  until calibration and analysis have been fixed.

#### 9.1.1 Data Set

There are three data sets discussed in this chapter, the physics data taken in 2009, the physics data taken in 2010, and the combined data of 2009 and 2010. For the combined data set, likelihood fitting is performed at once, with different PDFs of the observables by means of the event-by-event feature. Different normalizations in 2009 and 2010 are taken into account in the generation of toy MC experiments.

The MEG trigger condition is as described in Section 3.7.4. The signal event of  $\mu^+ \rightarrow e^+\gamma$  are back-to-back gamma ray and positron each with an energy of 52.8

MeV. To distinguish signal events from backgrounds, we use the following kinematic parameters: gamma energy  $E_\gamma$ , positron energy  $E_e$ , relative azimuthal angle between positron and photon  $\theta_{e\gamma}$ , relative polar angle between positron and photon  $\phi_{e\gamma}$  and relative timing between positron and photon  $t_{e\gamma}$ . The trigger for  $\mu^+ \rightarrow e^+\gamma$  event requires that  $E_\gamma > 44$  MeV,  $t_{e\gamma} < 10$  ns and direction match between gamma ray and positron.

### 9.1.2 Pre-Selection

To reduce data size and speed up analysis, a pre-selection is performed on all the data taken during the physics run. At first analysis the calibration is not done completely but some fundamental kinematics are already reconstructed. The pre-selection is done loose enough so not to lose any good events.

The selection criteria is defined as

1.  $6.875 \text{ ns} < t_\gamma - t_{TIC} < 4.375 \text{ ns}$
2.  $|t_{track} - t_{TIC}| < 50 \text{ ns}$

where  $t_\gamma$  is the gamma ray emission time reconstructed with an assumption that the muon decay vertex is at the origin;  $t_{TIC}$  is the timing counter hit time and the time-of-flight is not subtracted. Tracking information is not used at pre-selection. The reason for asymmetric window in the first selection cut is to acquire multiple turn events while the second condition requires at least one track associated with the trigger is found. Events are reduced by a factor of 5 with pre-selection

### 9.1.3 Blinding

For the pre-selected events, we apply a blinding process with the following definition for the hidden box.

1.  $48 \text{ MeV} < E_\gamma < 57.6 \text{ MeV}$

$$2. |t_{e\gamma}| < 0.7\text{ns}$$

The box size was decided with the detector resolutions to fully cover the signal region. The blind box is opened after all analysis and calibration is settled upon.

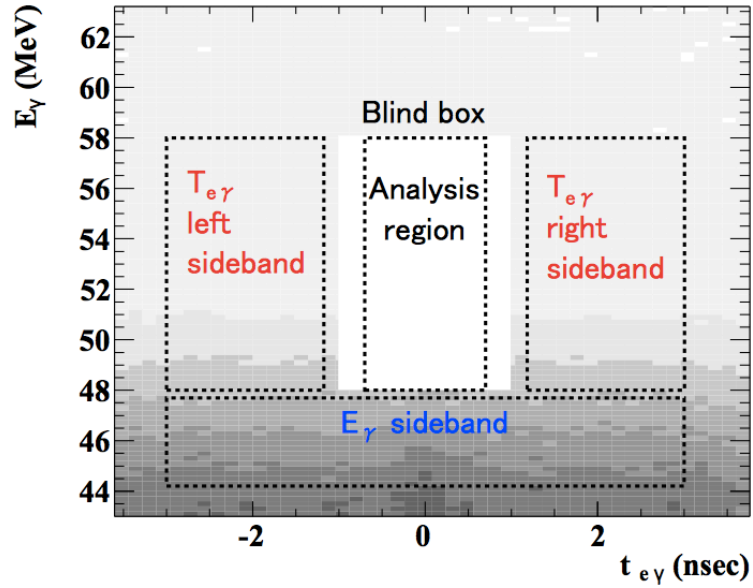


**Figure 9.1:** The blind box, the analysis window, both timing sidebands, and the low gamma energy sideband are shown on the  $(E_\gamma, t_{e\gamma})$  plane.

#### 9.1.4 Definition of Analysis Window

We define the analysis window to which the likelihood analysis is applied as the following:

1.  $|t_{e\gamma}| < 0.7$  ns
2.  $50 \text{ MeV} < E_e < 56 \text{ MeV}$
3.  $48 \text{ MeV} < E_\gamma < 58 \text{ MeV}$
4.  $|\theta_{e\gamma}| < 50$  mrad and  $|\phi_{e\gamma}| < 50$  mrad

The analysis window is wider and includes background events so that we can estimate the signal and backgrounds simultaneously. In addition cuts for acceptance and the

quality of reconstruction as described in Section 7.1 are applied.

As gamma ray position is reconstructed only using PMTs on the inner face of the LXe detector, the acceptance selection is applied as  $|u| < 25$  cm,  $|v| < 71$  cm since the resolutions near the edges worsen quickly. The quality of positron tracking is separated into two groups to apply different PDFs. The analysis region, as well as the blind box and sidebands are shown in Figure 9.1.

## 9.2 Maximum Likelihood Analysis

### 9.2.1 Definition

The goal of maximum likelihood analysis is to estimate the best values of number of  $\mu^+ \rightarrow e^+\gamma$  events, that of RD events ( $\mu^+ \rightarrow \nu_e \bar{\nu}_\mu e^+\gamma$ ) and that of accidental background events ( $N_{BG}$ ).

Let us define the following variables:

1.  $\vec{x}$ : a set of observables
2.  $\vec{X}$ : a data set of  $N_0$  independent observations  $\{\vec{x}_1, \vec{x}_2, \dots, \vec{x}_{N_0}\}$
3.  $\vec{\theta}$ : a set of unknown parameters of the likelihood

The likelihood function is defined as

$$\mathcal{L}(\vec{X}|\vec{\theta}) = \prod_{i=1}^{N_0} p(\vec{x}_i|\vec{\theta}) \quad (9.1)$$

where  $p(\vec{x}_i|\vec{\theta})$  is a conditional probability density function(PDF) which gives the probability density of the observation  $\vec{x}_i$  when the parameter set is equal to  $\vec{\theta}$ . It is a function of  $\vec{x}$  and normalized to 1.  $\mathcal{L}(\vec{X}|\vec{\theta})$  is a function of  $\vec{\theta}$ . The parameters  $\vec{\theta}$  can be determined so that the likelihood is maximized with a given  $\vec{X}$ , which is  $\vec{\theta}_{best}$ .

Since we do not fix the number of measurements in advance, the observed number of events fluctuates statistically in a Poisson distribution. When we regard the observed number of events as one of parameters to be estimated, the likelihood function is

extended to

$$\mathcal{L}_{ext}(\vec{X}|\vec{\theta}) = \frac{N^{N_0} e^{-N}}{N_0!} \prod_{i=1}^{N_0} p(\vec{x}_i|\vec{\theta}) \quad (9.2)$$

where  $N$  is the estimated number of events. This is called the extended likelihood function. We use the extended maximum likelihood fit to estimate the number of events of each event type.

In the MEG experiment we define  $\vec{\theta}$  by the number of event:

$$\vec{\theta} = (N_{sig}, N_{RD}, N_{BG}) \quad (9.3)$$

and

$$N = N_{sig} + N_{RD} + N_{BG} \quad (9.4)$$

The number of each event type obeys the Poisson distribution and the errors are independent one another in the extended maximum likelihood fit.

From a kinematic point of view, four parameters, energies, opening angle and time difference,  $(E_e, E_\gamma, \Theta_{e\gamma}, t_{e\gamma})$  can discriminate signals from backgrounds. However different detector responses of the drift chamber and timing counter means a different position performance between  $z$  and  $\phi$  direction. Therefore we separate the opening angle  $\Theta_{e\gamma}$  to  $\theta_{e\gamma}$  and  $\phi_{e\gamma}$ . Thus, the set of kinematic variables becomes

$$(E_e, E_\gamma, \theta_{e\gamma}, \phi_{e\gamma}, t_{e\gamma}) \quad (9.5)$$

PDF is different for each event as the performance of the detector is position dependent. Therefore we use event-by-event PDF so that we can use a good event with a large weight while also use worse measured events without discarding them.

Resolutions of the parameters are introduced to construct event-by-event PDFs, where we define the observable as

$$\vec{x}_i = (E_e, E_\gamma, \theta_{e\gamma}, \phi_{e\gamma}, t_{e\gamma}, \delta E_e, \delta E_\gamma, \delta \theta_{e\gamma}, \delta \phi_{e\gamma}, \delta t_{e\gamma})_i = (\vec{x}_i, \delta \vec{x}_i) \quad (9.6)$$

## 9. PHYSICS ANALYSIS ON DATA 2010

---

Using Bayes theorem, the probability that an event is observed at  $\vec{x} = \vec{x}_i$  is given by

$$p(\vec{x}_i) = P(sig) \cdot p(\vec{x}_i|sig) + P(RD) \cdot p(\vec{x}_i|RD) + P(BG) \cdot p(\vec{x}_i|BG) \quad (9.7)$$

The PDF can then be written as

$$p(\vec{x}_i|N_{sig}, N_{RD}, N_{BG}) = \frac{N_{sig}}{N} \cdot p(\vec{x}_i|sig) + \frac{N_{RD}}{N} \cdot p(\vec{x}_i|RD) + \frac{N_{BG}}{N} \cdot p(\vec{x}_i|BG) \quad (9.8)$$

If we rewrite PDFs for signal, radiative decay and accidental background defined below,

$$p(\vec{x}_i|sig) = S(\vec{x}_i) = s(\vec{x}_i|\delta\vec{x}_i)p(\vec{\delta x}_i), \quad (9.9)$$

$$p(\vec{x}_i|RD) = R(\vec{x}_i) = r(\vec{x}_i|\delta\vec{x}_i)p(\vec{\delta x}_i), \quad (9.10)$$

$$p(\vec{x}_i|BG) = B(\vec{x}_i) = b(\vec{x}_i|\delta\vec{x}_i)p(\vec{\delta x}_i), \quad (9.11)$$

then the likelihood function can be defined as

$$\begin{aligned} & \mathcal{L}(N_{sig}, N_{RD}, N_{BG}) \\ = & \frac{N^{N_0} e^{-N}}{N_0!} e^{-\frac{(N_{RD} - \langle N_{RD} \rangle)^2}{2\sigma_{RD}^2}} e^{-\frac{(N_{BG} - \langle N_{BG} \rangle)^2}{2\sigma_{BG}^2}} \prod_{i=1}^{N_0} \left( \frac{N_{sig}}{N} \cdot S(\vec{x}_i) + \frac{N_{RD}}{N} \cdot R(\vec{x}_i) + \frac{N_{BG}}{N} \cdot B(\vec{x}_i) \right) \\ = & \frac{N^{N_0} e^{-N}}{N_0!} e^{-\frac{(N_{RD} - \langle N_{RD} \rangle)^2}{2\sigma_{RD}^2}} e^{-\frac{(N_{BG} - \langle N_{BG} \rangle)^2}{2\sigma_{BG}^2}} \prod_{i=1}^{N_0} \left( \frac{N_{sig}}{N} \cdot s(\vec{x}_i|\delta\vec{x}_i)p(\vec{\delta x}_i) + \frac{N_{RD}}{N} \cdot r(\vec{x}_i|\delta\vec{x}_i)p(\vec{\delta x}_i) \right. \\ & \left. + \frac{N_{BG}}{N} \cdot b(\vec{x}_i|\delta\vec{x}_i)p(\vec{\delta x}_i) \right) \end{aligned}$$

Since it is assumed that  $p(\vec{\delta x}_i)$  is common to all event types, the term  $\prod_{i=1}^{N_0} p(\vec{\delta x}_i)$  is omitted in the likelihood fit because it is independent of the fit parameters, while  $p(\vec{\delta x}_i)$  is defined by the measured event distribution for the toy-MC simulation.

The maximization of the likelihood, or the minimization of the negative log likelihood (NLL) is done using the MINUIT package[8].

In the following sections, we discuss the measurement of  $S(\vec{x}_i)$ ,  $R(\vec{x}_i)$  and  $B(\vec{x}_i)$ .

### 9.3 Probability Density Functions

The Probability density functions (PDFs) are based on measured data and we estimate three types of PDFs: S, R and B for a signal, a prompt background from radiative muon decays and accidental background respectively. Figure 9.2 shows averaged PDFs by observables.

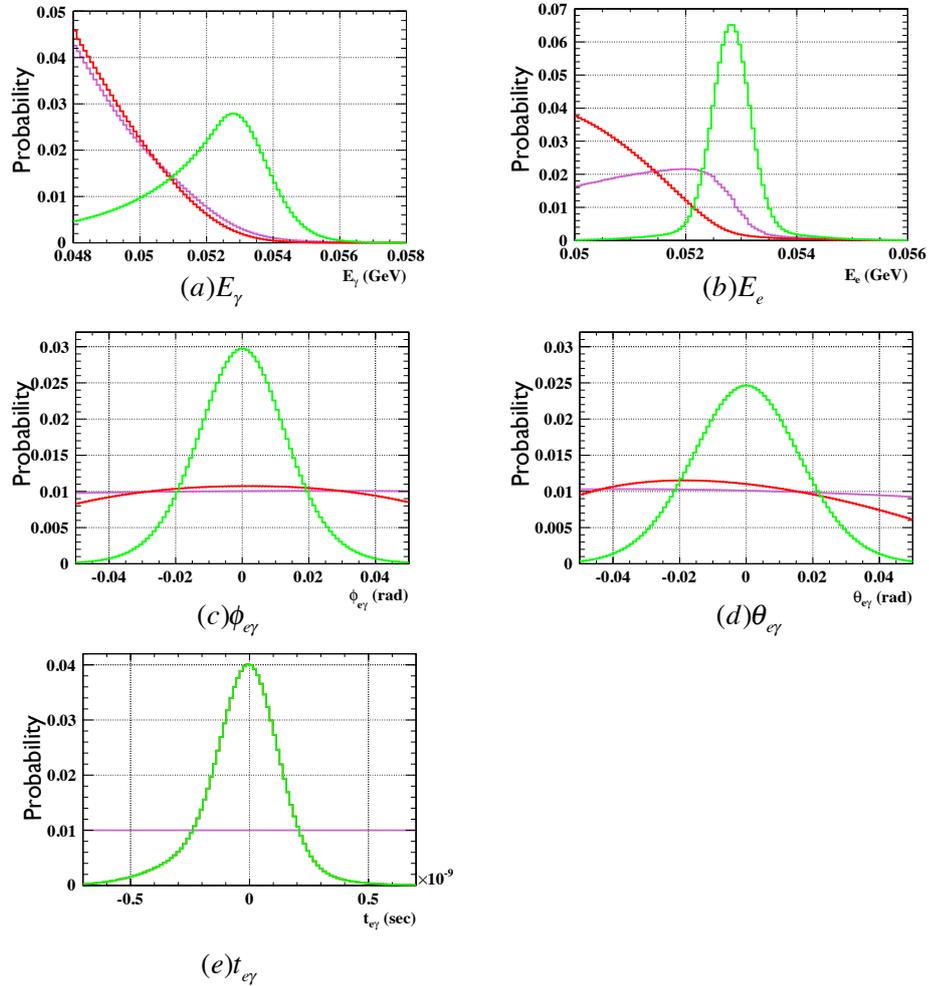


**Figure 9.2:** Probability density functions (PDFs) of each observable ( $E_\gamma$ ,  $E_e$ ,  $\phi_{e\gamma}$ ,  $\theta_{e\gamma}$ ,  $t_{e\gamma}$ ) averaged over all events within the analysis region. The green, red and magenta lines show PDFs of signal, radiative muon decay and accidental background (S, R, B), respectively.

### 9.3.1 Signal

There is no intrinsic correlation among the observables of the signal, however the positron variables are calculated from a fitted track and the intersection with the target, which results in correlations among the measurement errors of the observables. Such correlations are incorporated into PDF. The signal PDF, can be written as

$$\begin{aligned}
 S(E_e, E_\gamma, \theta_{e\gamma}, \phi_{e\gamma}, t_{e\gamma} | u_\gamma, v_\gamma, w_\gamma, x_e, y_e, z_e, \phi_e) = \\
 S(E_e | \phi_e) \times \\
 S(E_\gamma | u_\gamma, v_\gamma, w_\gamma) \times \\
 S(\theta_{e\gamma} | u_\gamma, v_\gamma, w_\gamma, x_e, y_e, z_e, E_e) \times \\
 S(\phi_{e\gamma} | u_\gamma, v_\gamma, w_\gamma, x_e, y_e, z_e, \theta_{e\gamma}, E_e, \phi_e) \\
 S(t_{e\gamma} | E_\gamma, E_e)
 \end{aligned}$$

#### $E_e$ PDF

The positron energy response is evaluated by fitting the kinematic edge of the Michel spectrum. The theoretical Michel spectrum multiplied by an energy dependent detector acceptance approximated by an error function is convolved with a response function modeled by a sum of three Gaussians. We also apply an additional correction for relative angle selection. The effect is evaluated by toy MC. Finally we fit the distribution with a sum of two Gaussians, and the result is used as signal PDF. The details of the parameters are in Table 9.1, together with those for background and radiative muon decay.

The PDF uncertainty from the statistics of side-band sample is evaluated in the fit as a covariance matrix. The global energy scale uncertainty is estimated to be 25 keV by the study with Monte Carlo; the accuracy of the determination of the energy scale with the Michel fit on the MC sample.

Parameter	Sig	BG	RMD
$f_{core}$	0.96	0.95	0.93
$\mu_{core}$ (keV)	79,-49,-21,1	93,-35,8,15	79,-49,-21,1.4
$\sigma_{core}$ (keV)	327	308	314
$\mu_{tail}$ (keV)	92,-36,-8,14	-500	246,141,169,191
$\sigma_{tail}$ (keV)	1144	1076	1165
$\mu_{Acc}$ (MeV)	-	50.4	51.2
$\nu_{Acc}$ (MeV)	-	2.26	2.85

Table 9.1:  $E_e$  parameters.

### Relative Angle PDF

The PDF of relative angles are defined by the angular responses formed by combining the evaluated resolutions of gamma-ray position, positron emission angles and muon decay vertex. The PDF of the relative angles are sum of several Gaussian functions. The means and sigmas of the Gaussian are calculated on an event-by-event basis.

### $t_{e\gamma}$ PDF

The time response is evaluated by the RMD peak in  $E_\gamma$ -sideband, as discussed in Section 7.5.3.

The conditions of the  $E_\gamma$ -sideband data used for the extraction are the following:

1.  $40 < E_\gamma < 47$  MeV
2.  $45 < E_e < 53$  MeV
3.  $|\phi_{e\gamma}| < 280$  mrad and  $|\theta_{e\gamma}| < 280$  mrad
4. kinematic cut of the reconstructed invariant mass  $< M_\mu$

We fit the distribution with a sum of two Gaussians and a flat distribution. The results are listed in Table 9.2. The origin of the tail component is studied with the MC and comes from the error of the tracking, mainly by the scatter on the material between TC and DC, and the responses of XEC and TC are well approximated by a

Gaussian.

$f_{core}$	0.75
$\sigma_{core}$ (psec)	124
$\mu_{tail}$ (psec)	-133
$\sigma_{tail}$ (psec)	250

**Table 9.2:** Fit results of time response extraction from  $E_\gamma$ -sideband.

### $E_\gamma$ PDF

$E_\gamma$  PDF is defined by gamma energy response which is evaluated by the 54.9 MeV gamma ray in  $\pi^0$  run.

To fit the  $\pi^0$  spectrum, we use the following selection criteria:

1. Energy of the gamma ray collected by NaI detector has to be  $65 < E_{NaI} < 98$  MeV for the 54.9 MeV peak at the LXe detector side and  $40 < E_{NaI} < 62$  MeV for the 83.9 MeV peak.
2. Concentration of energy deposition on the central crystal larger than 60 % of the total energy deposition.
3. Opening angle larger than  $170^\circ$ .

Since the selected events are not exactly monochromatic and there is a correlation between opening angle and the two gamma energies, we will later correct the reconstructed energy using the reconstructed opening angle.

We fit the spectrum with the following function,

$$f(x) = f_0(x) \otimes g_{\pi^0}(x) \otimes h_{\pi^-}(x) \quad (9.12)$$

$f_0(x)$  is the response function of the detector and can be written as

$$f_0(x) = \begin{cases} A \exp\left(\frac{t}{\sigma_{up0}^2} \left(\frac{t}{2} - (x - x_0)\right)\right) & x \leq x_0 + t, \\ A \exp\left(\frac{(x-x_0)^2}{-2\sigma_{up0}^2}\right) & x > x_0 + t, \end{cases} \quad (9.13)$$

### 9.3 Probability Density Functions

where  $A$  is a scale parameter;  $x_0$  is the peak position;  $t$  is a transition parameter and  $\sigma_{up_0}$  is a resolution parameter which indicates the spread of distribution in the higher side. The lower tail is because of interactions with material in front of detector and shower escapes mainly from the inner face.

$g_{\pi^0}(x)$  comes from the opening angle resolution and is studied with MC. The spread of energy distribution is found to not negligible and asymmetric (Figure 9.3), which results in an overestimation of energy scale (for the 54.9 MeV peak) and resolution. It is found that this contribution is negligible should we set the opening angle cut as  $> 175^\circ$ . However there is not enough data to use the higher threshold for all positions. Therefore this correction is added and as a result the two energy scales obtained from 54.9 MeV and 83.9 MeV agree within 0.1%.

$h_{\pi^-}(x)$  comes from the different background condition in  $\pi^0$  run. The background under the  $\pi^-$  beam is higher than that under normal  $\mu^+$  beam due to positrons from the beamline (no separator) and neutrons from the  $\pi^-$  reaction or the radiative capture reaction in low energy region and gamma rays from these reactions in high energy region. The pedestal events taken during the run is used as a measurement of the background.

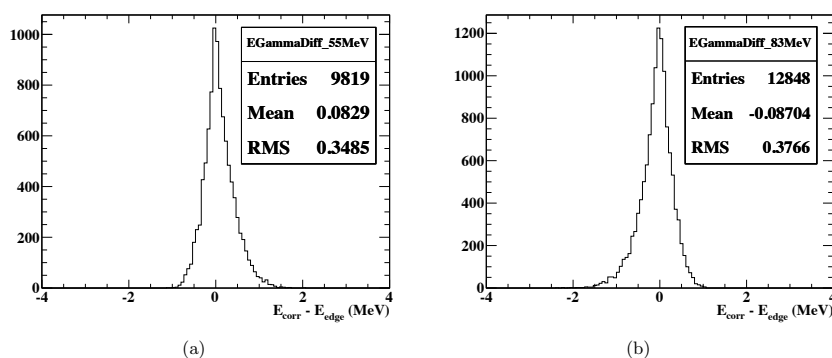


**Figure 9.3:** Residual energy distribution in  $\pi^0$  due to opening angle resolution. The true energy is corrected by the energy-opening angle correlation to the kinematic edge using the reconstructed opening angle. (a) is for the 54.9 MeV side and (b) is for the 83.9 MeV side.

To extract the signal PDFs from  $\pi^0$  data, we divide the acceptance into boxes in  $(u, v, w)$  and extract the position dependent PDF separately for each division. The

## 9. PHYSICS ANALYSIS ON DATA 2010

---

PDFs obtained this way are statistically correct. The divisions for  $(u, v)$  are shown in Figure 9.4. For 2010 data we divide  $w$  into four regions ( $0 < w < 0.8$  cm), ( $0.8 < w < 3$  cm), ( $3 < w < 8$  cm), ( $8 \text{ cm} < w$ ).

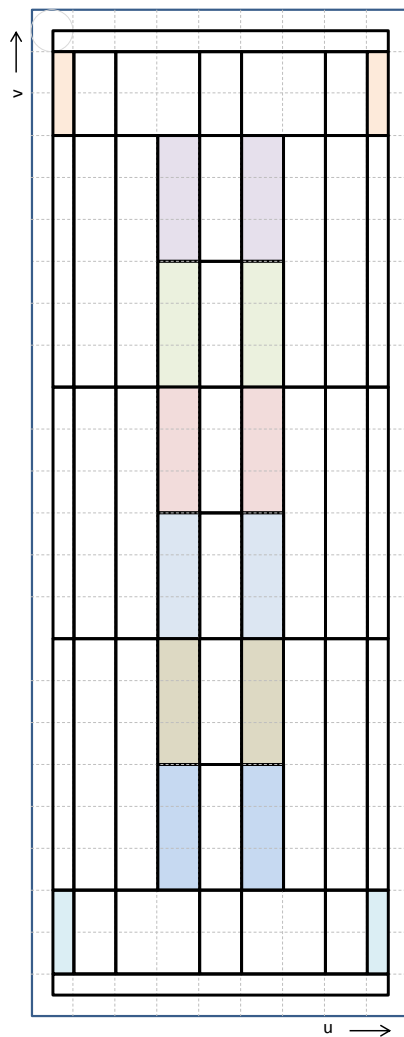
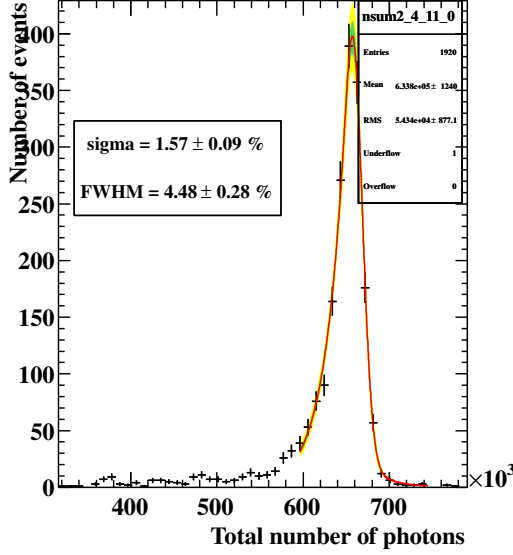
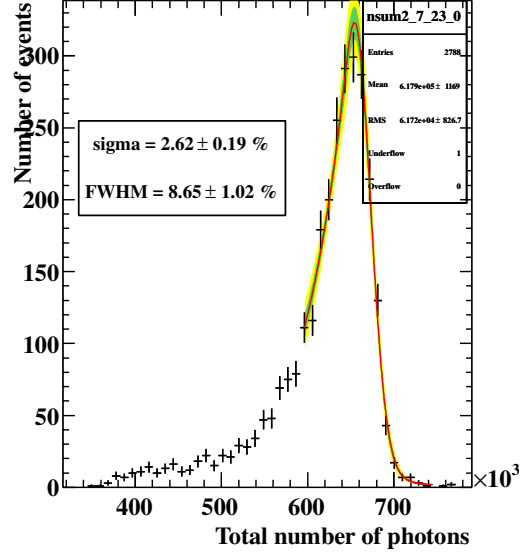


**Figure 9.4:** Divisions in  $(u, v)$  for signal PDF extraction. Separate but same color regions are combined.

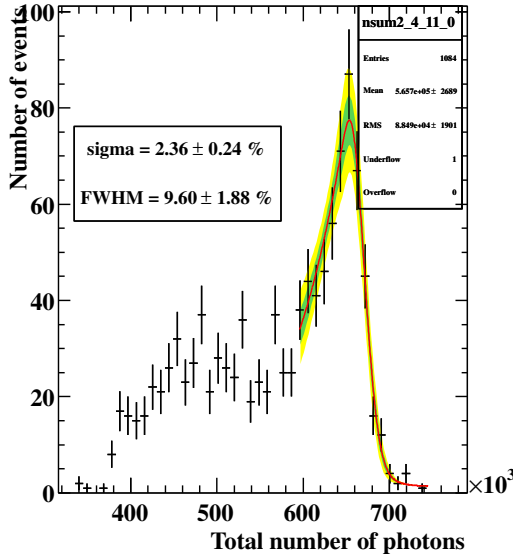
Examples of the fit are shown in Figure 9.5 and all the fit results produce the actual  $\pi^0$  spectra well.



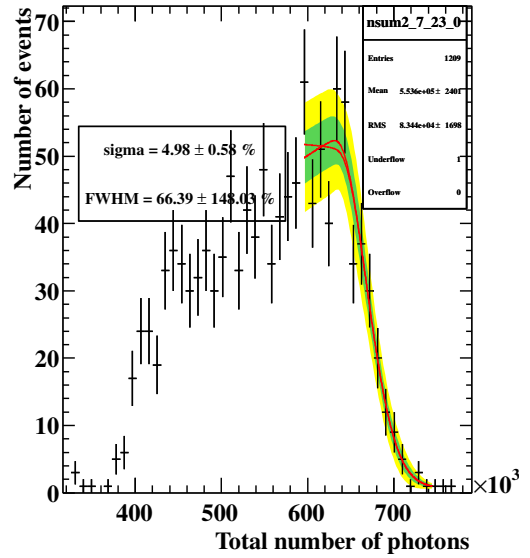
(a)  $3 < w < 8$ , central



(b)  $3 < w < 8$ , edge



(c)  $w < 0.8$ , central



(d)  $w < 0.8$ , edge

**Figure 9.5:** Examples of  $\pi^0$  54.9 MeV peak fit. Red lines are the best fit functions. Green and yellow bands show the confidence intervals of the function at 68% and 95% C.L. calculated with the covariance matrix evaluated in fitting.

### 9.3.2 Radiative Muon Decay

The radiative muon decay has a kinematic correlation between observable parameters. It is defined as

$$R(E_e, E_\gamma, \theta_{e\gamma}, \phi_{e\gamma}, t_{e\gamma} | u_\gamma, v_\gamma, w_\gamma, \phi_e, \theta_e) = \\ R(E_e, E_\gamma, \theta_{e\gamma}, \phi_{e\gamma} | u_\gamma, v_\gamma, w_\gamma, \phi_e, \theta_e) \times \\ R(t_{e\gamma} | E_\gamma, E_e)$$

#### Kinematically correlated term

The kinematically correlated term is formed with the theoretical correlation of radiative decay folded with the detector response functions and acceptance functions. We start by building the first term of the PDF from the theoretical formula of the differential branching ratio of RMD[32], however we cannot ignore terms with polarization vector. The PDF is formed by folding detector responses in four dimensions with the following procedure: multiply the  $E_e$  acceptance curve; Convolve two dimensional angular response; convolve  $E_e$  response from Michel spectrum; Convolve  $E_\gamma$  response which is the same as signal PDF; multiply  $E_\gamma$  efficiency curve, which is the error function extracted from the gamma-ray BG spectrum fit for each position; multiply angular efficiency estimated from BG distribution.

#### $t_{e\gamma}$ PDF

We use the same time PDF as the one for signal except for the correlation. Dependence of the time center  $t_0$  on  $E_e$  in both the data and MC is observed. We measure  $t_0$  values for three  $E_e$  ranges in the  $E_g$ -sideband data, and extract the dependence as a linear function. The coefficient is measured to be 4.6 psec/MeV, which is one order smaller than that of the signal correlation, and it is consistent with that from MC. This dependence is applied to the RMD time PDF.

### 9.3.3 Accidental Background

The accidental background PDF, B, can be written as

$$\begin{aligned}
 B(E_e, E_\gamma, \theta_{e\gamma}, \phi_{e\gamma}, t_{e\gamma} | u_\gamma, v_\gamma, w_\gamma, \phi_e) = & B(t_{e\gamma}) \times \\
 & B(E_\gamma | u_\gamma, v_\gamma, w_\gamma) \times \\
 & B(\theta_{e\gamma} | v_\gamma) \times \\
 & B(\phi_{e\gamma} | u_\gamma) \times \\
 & B(E_e | \phi_e)
 \end{aligned}$$

The PDFs are extracted from sideband data except for  $t_{e\gamma}$  which is assumed to be a constant function.

#### Relative Angle PDF

The PDFs for relative angles are obtained from data in time sidebands with looser cuts of  $|\theta_{e\gamma}| < 200$  mrad,  $|\phi_{e\gamma}| < 200$  mrad and  $E_\gamma > 46$  MeV.

No strong correlation between  $\theta_{e\gamma}$  and  $\phi_{e\gamma}$  is found as shown in Figure 9.6. However Figure 9.7 shows that there is correlation between  $\theta_{e\gamma}$  ( $\phi_{e\gamma}$ ) distribution and  $u_\gamma$  ( $v_\gamma$ ).

To extract the angular PDF, we divide  $\theta_{e\gamma}$  in five slices and  $\phi_{e\gamma}$  in eight slices and fit the distribution with a third degree polynomial function. Figure 9.8 and Figure 9.9 show the angular distributions of BG.

## 9. PHYSICS ANALYSIS ON DATA 2010

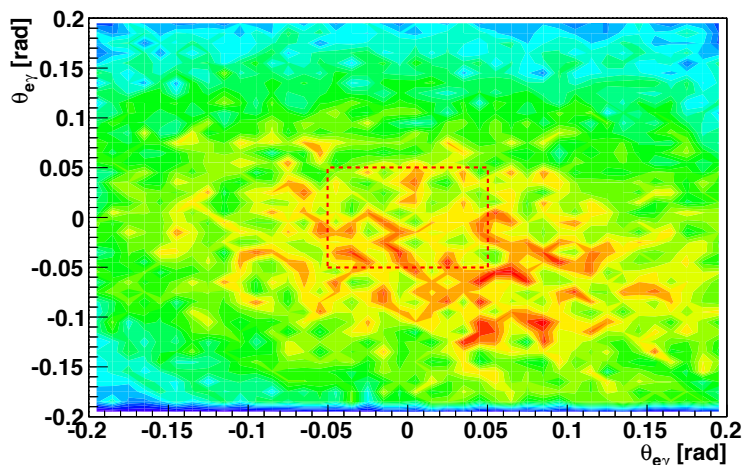


**Figure 9.6:** BG distribution on  $(\theta_{e\gamma}, \phi_{e\gamma})$  measured in time sidebands. The red box is the analysis region.

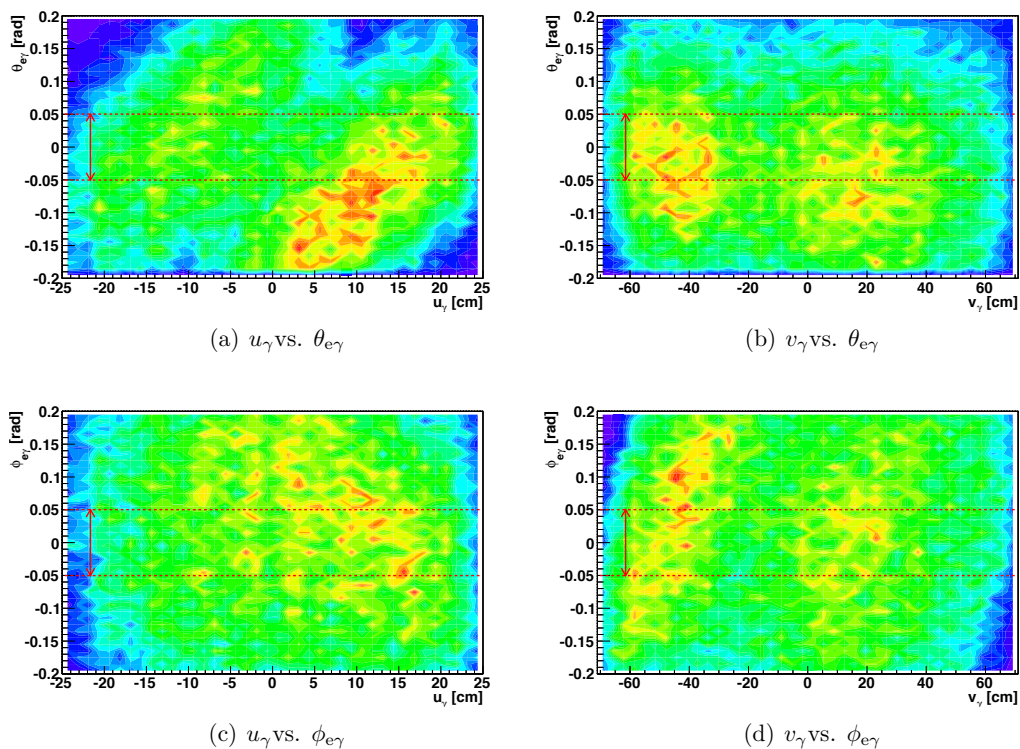


**Figure 9.7:** Position dependence of angular distribution for 2010 data.

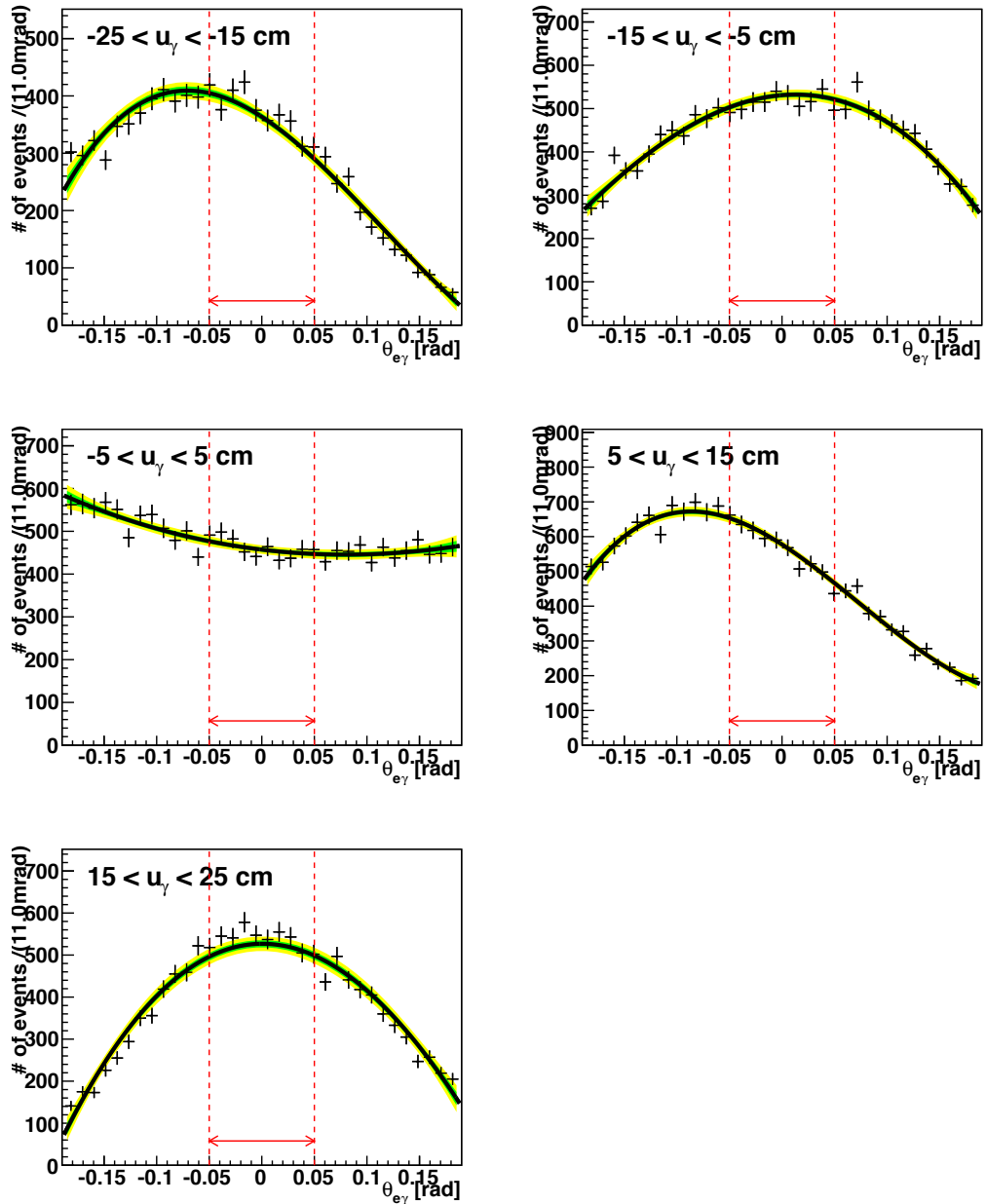
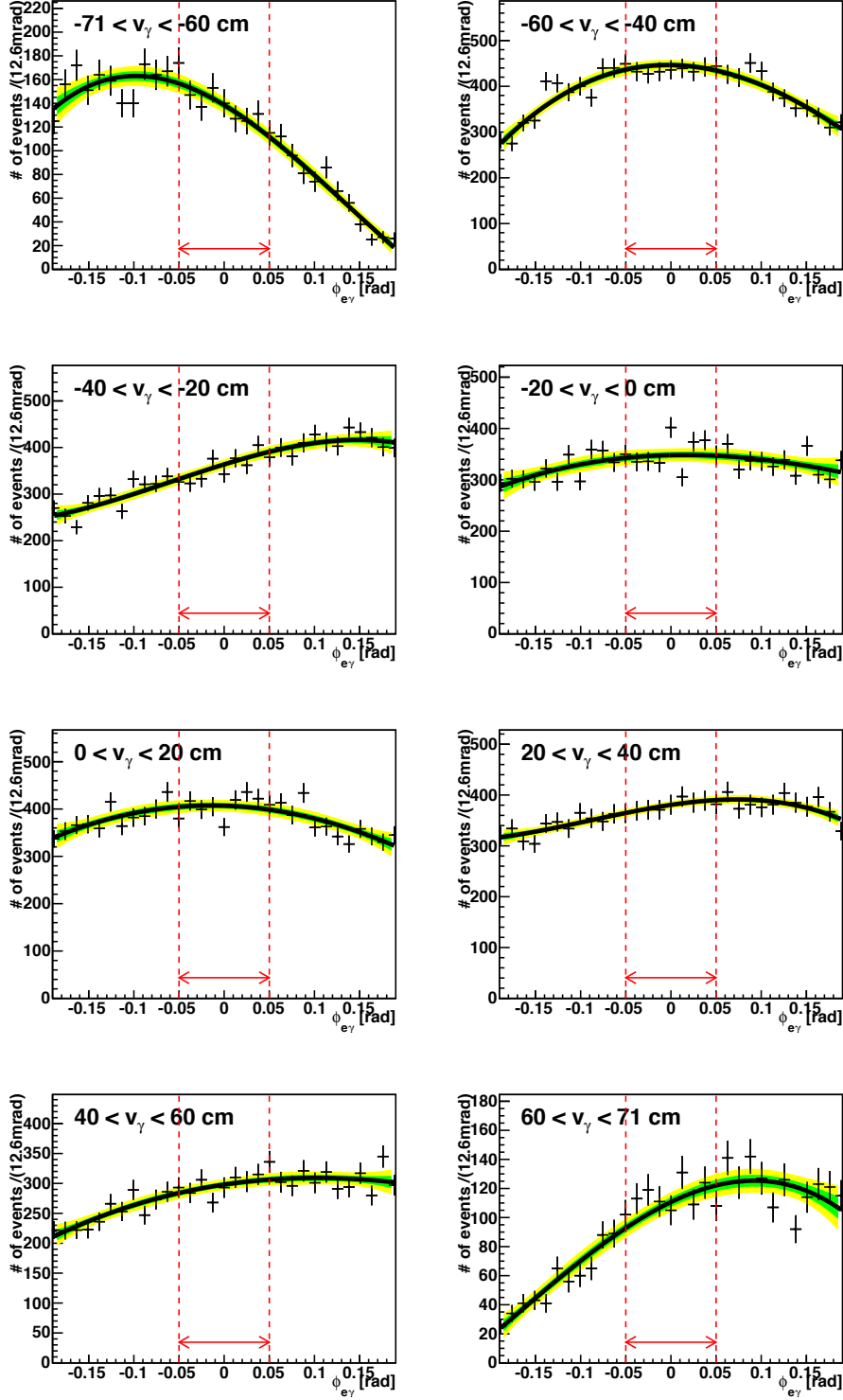


Figure 9.8: BG  $\theta_{e\gamma}$  distributions in  $u_\gamma$  slices for 2010 data. The black line is the best fitted function. The green and yellow band show the 68% and 95% confidence intervals respectively. The red arrow shows the analysis region in the likelihood fit..

## 9. PHYSICS ANALYSIS ON DATA 2010



**Figure 9.9:** BG  $\phi_{e\gamma}$  distributions in  $\nu_\gamma$  slices for 2010 data. The black line is the best fitted function. The green and yellow band show the 68% and 95% confidence intervals respectively. The red arrow shows the analysis region in the likelihood fit.

### $E_e$ PDF

$E_e$  PDFs are measured in side-bands by fitting Michel spectrum, similarly to the signal PDF extraction except that the response is modeled with a sum of two Gaussians. The sideband data used here is cut with  $|\theta_{e\gamma}| < 100$  mrad,  $|\phi_{e\gamma}| < 100$  mrad and the fit region is 49-56 MeV. The fit parameters are given in Table 9.1.

### $E_\gamma$ PDF

$E_\gamma$  is position dependent and estimated by using the BG spectra observed in  $t_{e\gamma}$  sideband. The selection criteria is same as that for signal search except that there is no condition on relative angle. The time range for the sideband is  $1 < |t_{e\gamma}| < 1000$  nsec.

We extract the background PDFs according to position just like signal PDF extraction. This is not only due to different resolutions in different positions but also the BG spectrum itself may be different. We divide the depth into three parts: ( $0 < w < 1$  cm), ( $1 < w < 2$  cm) and ( $w > 2$  cm). The  $(u, v)$  divisions are shown in Figure 9.10. Pileup events are treated separately.

We fit the BG spectra with expected smooth distributions. We start from the MC distribution of energy deposition in LXe detector by a single event from RMD or AIF, then convolve it with pedestal distribution and detector response. Then the cosmic ray spectrum is added and the trigger curves are applied on the lower and higher side.

To take into account the effect of pileup elimination, the pedestal distribution is shrunk by factors depending on the pieup identification result. The factors are adjusted in advance and stay fixed in fitting. The detector response is given as a Gaussian with the sigma for detector resolution and mean for energy scale. The cosmic ray spectrum is obtained from CR runs and is given as position dependent templates. The trigger efficiency curve is an error function with two free parameters at the lower side and at the higher side, it is measured in CR data by applying the trigger selection and comparing the spectra with and without the selection. In total, six parameters are determined in the fit. Some examples of the fit are shown in Figure 9.11. The total

## 9. PHYSICS ANALYSIS ON DATA 2010

---

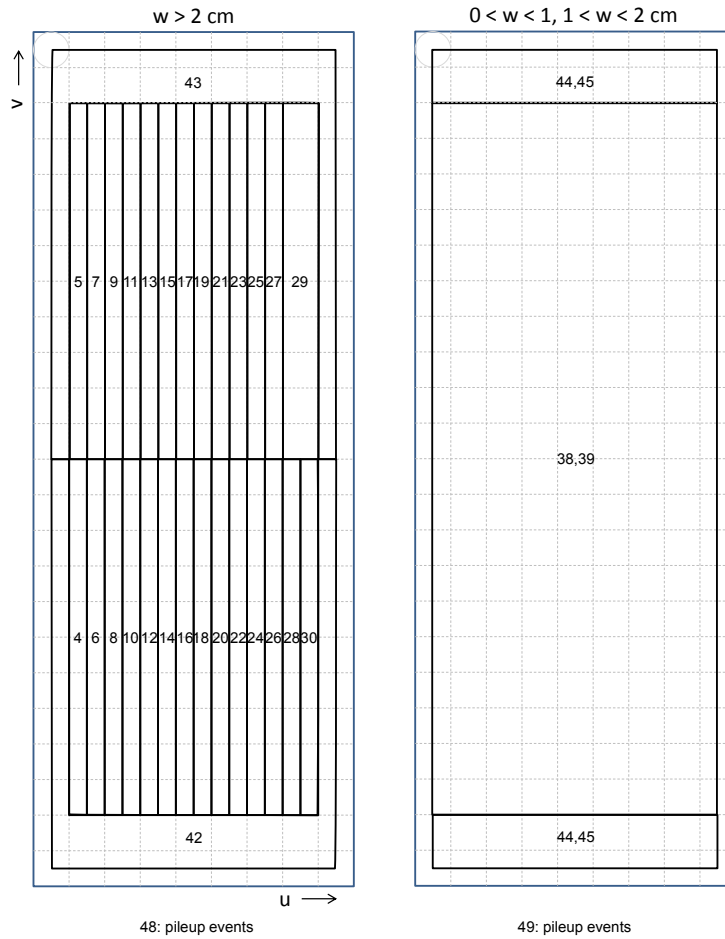


**Figure 9.10:** Divisions in  $(u, v)$  for background PDF extraction.

spectrum, which is an average PDF is shown in (a) but it is not used in the physics analysis.

### 9.3 Probability Density Functions

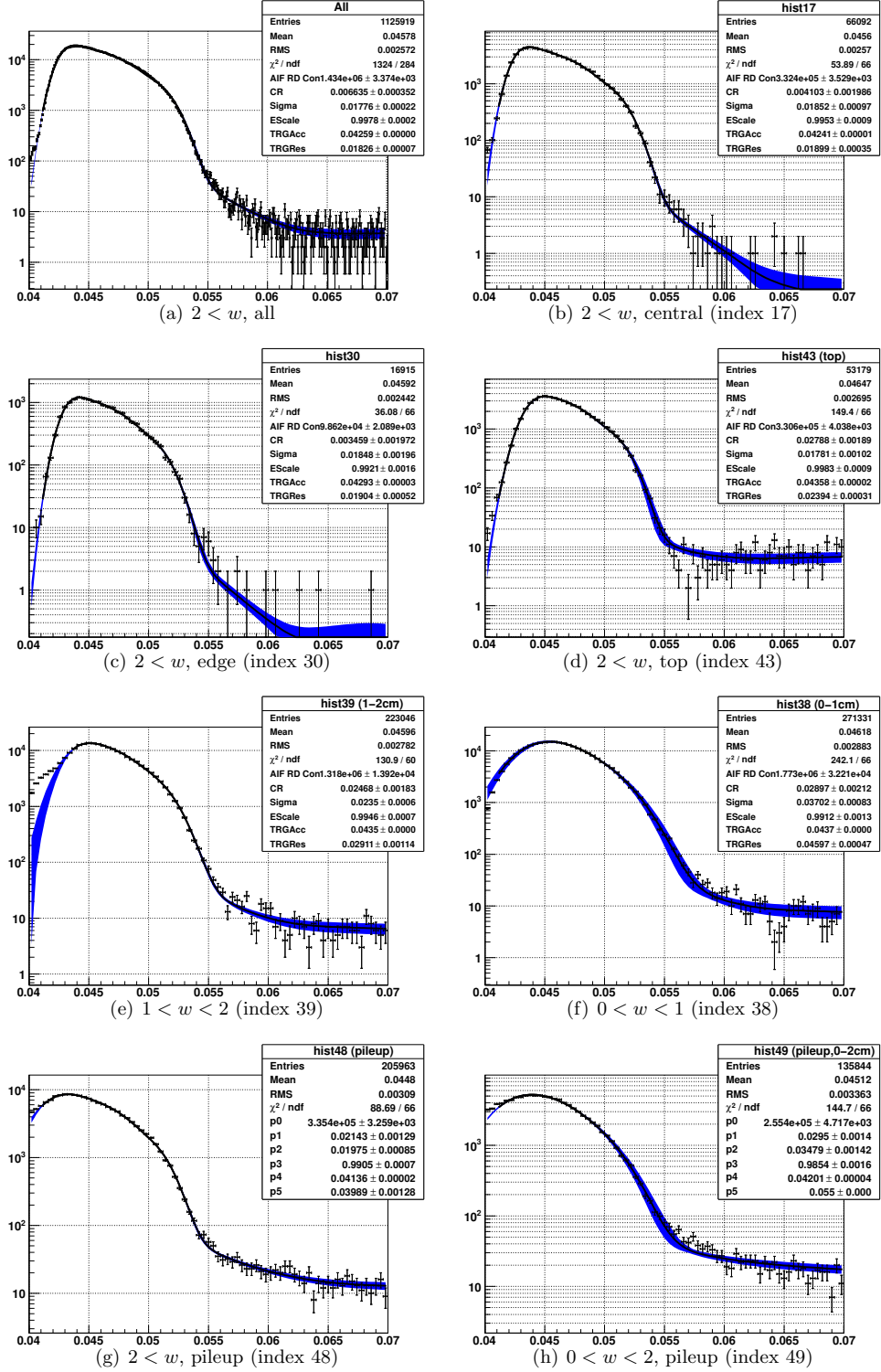


**Figure 9.11:** Examples of background fit for 2010 data. Black lines are the best fit functions and blue bands show the confidence intervals at 95% C. L. calculated with the covariance matrix.

## 9. PHYSICS ANALYSIS ON DATA 2010

---

The functions fit well and we can describe the observed distributions with smooth functions to eliminate statistical fluctuation and estimate the uncertainties. It also shows our understanding of background is correct. We can decompose the components of background. Each component is shown in Figure 9.12 and their fractions are listed in Table 9.3.

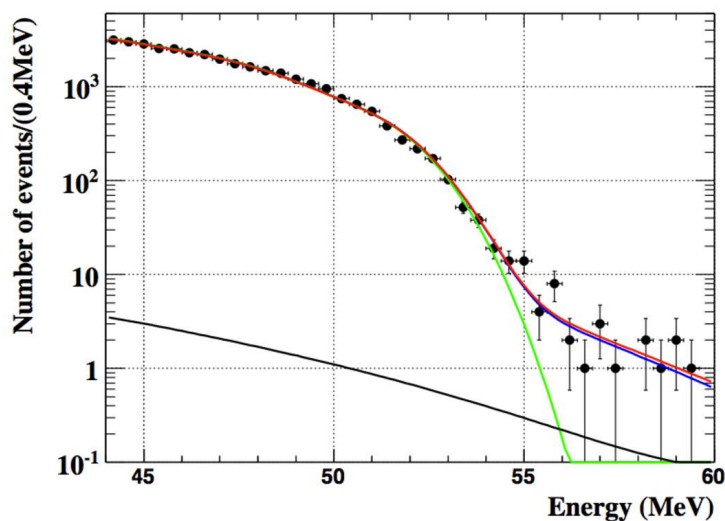


**Figure 9.12:** Components of background. Data points show the  $\gamma$ -ray background spectrum taken from the sideband physics data. Green line is the fitted spectrum from RMD and AIF. Blue line is the green line plus effects of pileup. Black line is the cosmic ray spectrum and the red line is the fitted result of all background.

Component	Fraction
Single $\gamma$ from RMD or AIF	94-96%
Cosmic ray	<1%
All the rest	3-5%

**Table 9.3:** Fractions of background components in the signal region. All the rest come from pileup or reconstruction tail.

### 9.3.4 Confidence Interval

The confidence interval is calculated using the Feldman-Cousins unified approach with the profile-likelihood ordering[64].

We define the following parameters

$$q(N_{sig}) = -2 \ln \lambda_p(N_{sig}) \quad (9.14)$$

$$\ln \lambda_p(N_{sig}) = \frac{\mathcal{L}(N_{sig}, \hat{N}_{RD}(N_{sig}), \hat{N}_{BG}(N_{sig}))}{\mathcal{L}(N_{sig}, \hat{N}_{RD}(N_{sig}), \hat{N}_{BG}(N_{sig}))} \quad (9.15)$$

where  $\hat{N}_j(j = sig, RD, BG)$  is  $N_j$  which maximizes the likelihood and  $\hat{N}$  is  $N_j$  that maximizes the likelihood of a fixed  $N_{sig}$ .

We calculate the confidence interval with the following procedure:

1. Make a list of events from the data. Variables to decide detector response such as positron track quality,  $\phi_{e\gamma}$ ,  $\gamma$  conversion point are associated with each event.
2. Generate many toy-MC experiments assuming a true  $\mathcal{B}$ .  $q(N_{sig})$  is calculated in each experiment. For the toy-MC experiments, an event is picked up from the list made above and detector response is determined according to the list, generating an event. Then calculate  $q(N_{sig})$  on the data and use the distribution of  $q(N_{sig})$  obtained at the earlier step to find the probability to observe  $q(N_{sig})$  that is larger than that observed on the data ( $q^{obs}(N_{sig})$ ).
3. Repeat the second procedure and find the 90% C.L. where the probability is less or equal to 0.9.

With this method when  $\hat{N}_{sig}$  is small only the upper limits are calculated and lower limits appear when  $\hat{N}_{sig}$  becomes large. The confidence intervals at 90% C.L. should include the true  $N_{sig}$  in 90% probability. When the background-only hypothesis is true, the lower limits should appear and  $N_{sig} = 0$  should be excluded in 10% probability.

## 9.4 Normalization

A branching ratio is defined as a ratio of the decay rate for a particular process, in relation to the total one. For muon decay, we use Michel decay for normalization purpose to avoid influences from changes in instantaneous beam intensities or conditions of DC detectors.

The total number of the Michel decay (MD),  $N_{MD}$ , is estimated from the event triggered with only timing  $\phi$  counter mixed in the MEG physics data taking simultaneously. It consists of some efficiencies and acceptances,

$$N_{MD} = N_{\mu} \times T_{e\nu\bar{\nu}} \times B_{e\nu\bar{\nu}} \times f_{e\nu\bar{\nu}}^E \times \frac{1}{P_{e\nu\bar{\nu}}} \times \epsilon_{e\nu\bar{\nu}}^{trig} \times A_{e\nu\bar{\nu}}^{TIC} \times \epsilon_{e\nu\bar{\nu}}^{DCH} A_{e\nu\bar{\nu}}^{DCH} \quad (9.16)$$

where each factor has the following definitions:

$N_{\mu} \times T_{e\nu\bar{\nu}}$  : Number of stopped muons during a time  $T_{e\nu\bar{\nu}}$ .

$B_{e\nu\bar{\nu}}$  Branching ratio of Michel decay.

$f_{e\nu\bar{\nu}}^E$  Fraction of Michel spectrum above 50MeV.

$P_{e\nu\bar{\nu}}$  Pre-scale factor of TIC trigger.

$\epsilon_{e\nu\bar{\nu}}^{trig}$  : Conditional trigger efficiency.

$A_{e\nu\bar{\nu}}^{TIC}$  : Conditional acceptance of timing counter including DC-TC matching efficiency.

$\epsilon_{e\nu\bar{\nu}}^{DCH}$  : Conditional tracking efficiency including selection criteria.

$A_{e\nu\bar{\nu}}^{DCH}$  : Geometrical acceptance of drift chamber.

A similar equation can be written for the number of signals:

$$N_{sig} = N_{\mu} \times T_{e\gamma} \times B_{e\gamma} \times \epsilon_{e\gamma}^{trig} \times A_{e\gamma}^{TIC} \times \epsilon_{e\gamma}^{DCH} A_{e\gamma}^{DCH} \times \epsilon_{e\gamma}^{LX_e} \times A_{e\gamma}^{LX_e} \quad (9.17)$$

where  $\epsilon_{e\gamma}^{LX_e}$  is the gamma-ray detection and reconstruction efficiency and  $A_{e\gamma}^{LX_e}$  is the conditional acceptance of gamma-ray from  $\mu^+ \rightarrow e^+\gamma$  decay.

Then the branching ratio on  $mu^+ \rightarrow e^+\gamma$  decay can be written as

$$\frac{B_{e\gamma}}{B_{e\nu\bar{\nu}}} = \frac{N_{sig}}{N_{MD}} \times \frac{f_{e\nu\bar{\nu}}^E}{P_{e\nu\bar{\nu}}} \times \frac{\epsilon_{e\nu\bar{\nu}}^{trig}}{\epsilon_{e\gamma}^{trig}} \times \frac{A_{e\nu\bar{\nu}}^{TIC}}{A_{e\nu\bar{\nu}}^{TIC}} \times \frac{\epsilon_{e\nu\bar{\nu}}^{DCH}}{\epsilon_{e\gamma}^{DCH}} \times \frac{1}{\epsilon_{e\gamma}^{LX_e}} \times \frac{1}{A_{e\gamma}^{LX_e}} \quad (9.18)$$

Normalization factor  $k$  is defined as

$$1/k = \frac{1}{N_{sig}} \cdot \frac{B_{e\gamma}}{B_{e\nu\bar{\nu}}} \quad (9.19)$$

The factors for calculation include number of Michel positrons (30670), pre-scale factor ( $1 \times 10^7$ ), fraction of Michel spectrum (1.23), trigger efficiency ratio (0.94), DC-TC matching ratio (0.922), gamma ray efficiency (0.59) and gamma ray acceptance (0.99), which give a normalization factor of

$$k_{2010} = (2.23 \pm 0.16) \times 10^{12} \quad (9.20)$$

For the combined data of 2009 and 2010, the normalization factor is

$$k_{combined} = (3.31 \pm 0.22) \times 10^{12} \quad (9.21)$$

## 9.5 Systematics

To incorporate systematics, we use two different methods. For  $N_{RD}$  and  $N_{BG}$ , profile method is used. The best estimates for  $N_{RD}$  and  $N_{BG}$  are calculated for each  $N_{sig}$ . Their uncertainties are incorporated in the  $N_{sig}$  interval through correlations between  $N_{sig}$  and  $N_{RD}$ , and  $N_{sig}$  and  $N_{BG}$ .

The uncertainties of the parameters of the PDF of the observables (the resolutions, correlations, fraction of core and tail etc.) are incorporated by randomizing them in the generation of the toy-MC experiments. The signal normalization uncertainty is incorporated by randomizing  $N_{sig}$  in the generation. The fittings on the toy-MC experiments are done using the same parameters as those used in the fitting on the data.

A random number is generated for each parameter once for each experiment and used to generate all the events in the experiment. Different random numbers are

## 9. PHYSICS ANALYSIS ON DATA 2010

---

generated for the statistically independent uncertainties, such as the time center, the parameters of Michel shape etc. For the common uncertainties, for example the relative alignment between the photon detector and the positron spectrometer, a single random number is used to generate events. The correlations in the errors of the parameters are taken into account using the covariance matrices.

The uncertainty of the signal PDF is evaluated from the data statistics as a covariance matrix since the parameters are highly correlated to each other. The mean parameter is fixed to the best-fit value, and the other PDF parameters are free.

The systematic uncertainties on the mean and  $\sigma$  of the signal  $t_{e\gamma}$  PDF are estimated from the statistical error on those parameters from the fit to the radiative decay timing peak. The mean of the signal  $E_e$  PDF is estimated by using it as a floating parameter in Michel fit to accidental positrons.

The systematic uncertainty in the signal  $E_e$  PDF shape is estimated with the uncertainty of the full RMS within the signal window.

The peak of the signal  $E_\gamma$  PDF is obtained from the 55 MeV in the  $\pi^0$  data. The uncertainty of energy scale is 0.43%. The uncertainties of the shape of the signal  $E_\gamma$  PDF are taken from the statistical error on the fits to the 55 MeV peak.

The typical uncertainties of  $t_{e\gamma}$  PDF are  $\sim 0.05$  on  $f_{core}$ ,  $\sim 7$ psec on  $\sigma_{core}$ ,  $\sim 60$ psec on  $\mu_{tail}$ , and  $\sim 50$ psec on  $\sigma_{tail}$ . The uncertainty of the mean,  $t_0$ , is independently estimated to be 15 psec including systematic errors. The stability of  $t_0$  is confirmed to be within this uncertainty by RD peaks during different run periods.

We estimated the effect of each systematic uncertainty with the following procedure:

1. Generate 100 pseudo experiments with the nominal PDF,  $N_{sig} = Poisson(3.8)$ . 3.8 is the upper limit obtained from the data.
2. Fit to the pseudo experiments with the nominal PDF. And calculate the likelihood ratio at the best fit and  $N_{sig} = 3.8$ .
3. Do the same on the same 100 pseudo experiments using the alternative PDF. In each experiment, the parameters in the fitting PDF are randomized according to their uncertainties.

4. Make a distribution of the difference of negative-log-likelihood-ratio at 2. and 3 (NLL).

Largest contributions come from uncertainties of offsets of the relative angles, correlation in the positron observables and normalization. Negative-log-likelihood-ratio from each factor is summarized in Table 9.4.

**Table 9.4:** Systematic uncertainties.

Factor	Estimated value	$\Delta$ NLL
Center of $\theta_{e\gamma}$ and $\phi_{e\gamma}$	3.9mrad	0.18
Positron correlations		0.16
Normalization	6.7%	0.13
$E_\gamma$ scale	0.31%	0.07
$E_e$ bias, core and tail	50keV(core)250(tail)	0.06
$t_{e\gamma}$ center	15psec	0.06
$E_\gamma$ BG shape		0.04
$E_\gamma$ signal shape		0.03
Positron angle resolutions ( $\theta_e, \phi_e, z_e, y_e$ )	10%	0.02
$\gamma$ angle resolution( $u_\gamma, v_\gamma, w_\gamma$ )	10%	0.02
$E_e$ BG shape		0.02
$E_e$ signal shape		0.01

## 9.6 Sensitivity

### 9.6.1 Background Evaluation By Sideband Analysis

Before analyzing the analysis window, we applied the maximum likelihood fit on side bands. We defined two windows in positive and negative  $t_{e\gamma}$ -sideband and four windows in  $\theta_{e\gamma}, \phi_{e\gamma}$  sideband.

**Negative time sideband:**  $48 \leq E_\gamma \leq 58$  MeV,  $50 \leq E_e \leq 56$  MeV,  $-2.7 \leq t_{e\gamma} \leq -1.3$  ns,  $|\theta_{e\gamma}| \leq 50$  mrad,  $|\phi_{e\gamma}| \leq 50$  mrad

## 9. PHYSICS ANALYSIS ON DATA 2010

---

**Positive time sideband:**  $48 \leq E_\gamma \leq 58$  MeV,  $50 \leq E_e \leq 56$  MeV,  $1.3 \leq t_{e\gamma} \leq 2.7$  ns,  $|\theta_{e\gamma}| \leq 50$  mrad,  $|\phi_{e\gamma}| \leq 50$  mrad

For time sidebands, the negative sideband is defined as  $-2.7 \times 10^{-9}$  ns  $< t_{e\gamma} < -1.3 \times 10^{-9}$  ns and the expected number of background events was scaled from the actual value observed in  $1$  ns  $< t_{e\gamma} < 3.9$  ns. The positive sideband ( $1.3 \times 10^{-9}$  ns  $< t_{e\gamma} < 2.7 \times 10^{-9}$  ns) was fit with the expected number of background events scaled from the observed number in  $-3.9$  ns  $< t_{e\gamma} < -1$  ns. The best fit results and confidence intervals in number of signals and branching ratio are shown in Table 9.5 and Table 9.6. The upper limits obtained from sideband analysis are consistent with the evaluated result from Toy MC (Section 9.6.2).

	$N_{sig}$	$N_{RD}$	$N_{BG}$
Negative time sideband	$2.3^{+7.7}_{-4.8}$	$+7.6^{+21.5}_{-18.8}$	$+619.8^{+25.3}_{-25.2}$
Positive time sideband	$-4.1^{+5.5}_{-2.2}$	$+14.0^{+24.4}_{-21.9}$	$+595.1^{+24.6}_{-24.4}$

**Table 9.5:** Best fit results of number of signal, radiative muon decay and background events.

	UL in $N_{sig}$	UL in $\mathcal{B}$
Negative time sideband	5.2	$2.3 \times 10^{-12}$
Positive time sideband	2.7	$1.2 \times 10^{-12}$

**Table 9.6:** Upper limits at 90% C.L. in number of signal events and branching ratio  $\mathcal{B}$ .

In time sidebands, RD background events are not be counted due to the time shift. Such events however would be observed in angle sidebands, which would offer a cross check in addition to time sidebands. Four angle sidebands are defined as following:

**Negative  $\theta_{e\gamma}$  sideband:**  $48 \leq E_\gamma \leq 58$  MeV,  $50 \leq E_e \leq 56$  MeV,  $|t_{e\gamma}| \leq 0.7$  ns,  $-150 \leq \theta_{e\gamma} \leq -50$  mrad,  $|\phi_{e\gamma}| \leq 50$  mrad

**Positive  $\theta_{e\gamma}$  sideband:**  $48 \leq E_\gamma \leq 58$  MeV,  $50 \leq E_e \leq 56$  MeV,  $|t_{e\gamma}| \leq 0.7$  ns,  $50 \leq \theta_{e\gamma} \leq 150$  mrad,  $|\phi_{e\gamma}| \leq 50$  mrad

**Negative  $\phi_{e\gamma}$  sideband:**  $48 \leq E_\gamma \leq 58 \text{ MeV}, 50 \leq E_e \leq 56 \text{ MeV}, |t_{e\gamma}| \leq 0.7 \text{ ns}, |\theta_{e\gamma}| \leq 50 \text{ mrad}, -150 \leq \phi_{e\gamma} \leq -50 \text{ mrad}$

**Positive  $\phi_{e\gamma}$  sideband:**  $48 \leq E_\gamma \leq 58 \text{ MeV}, 50 \leq E_e \leq 56 \text{ MeV}, |t_{e\gamma}| \leq 0.7 \text{ ns}, |\theta_{e\gamma}| \leq 50 \text{ mrad}, 50 \leq \phi_{e\gamma} \leq 150 \text{ mrad}$

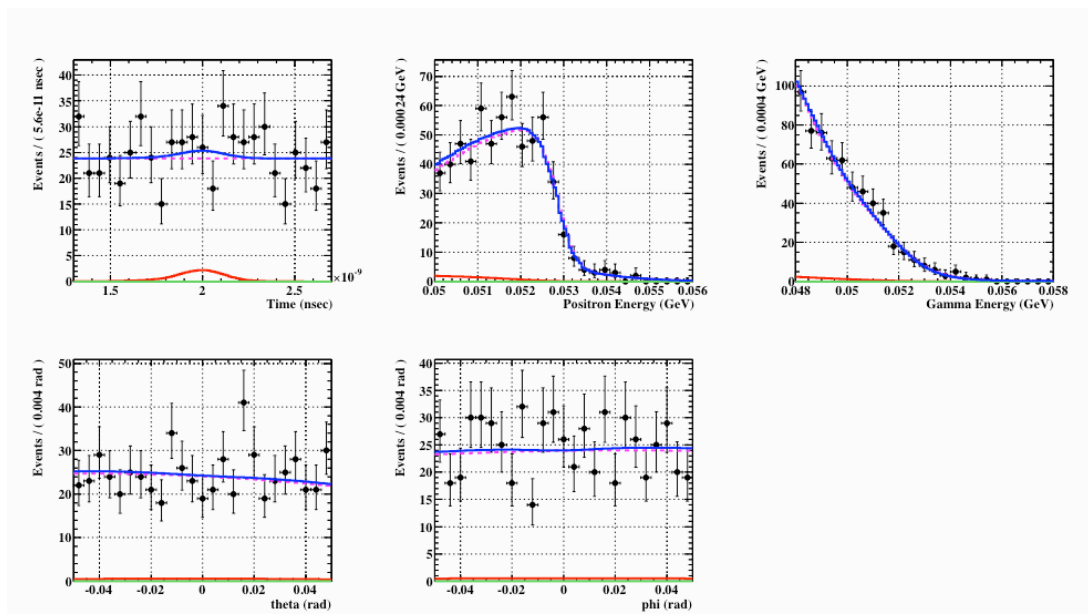
The expected number of BG events are counted as described above. The numbers of RD events are calculated using 10000 generated MC events and scaled with total number of RD in the wider angle region ( $N_{RD} = 87.7$ ). The fit results are shown in Table 9.7.

	$N_{sig}$	$N_{RD}$	$N_{BG}$
$-150 \leq \theta_{e\gamma} \leq -50 \text{ mrad}$	$-5.8^{+5.9}_{-2.8}$	$+26.1^{+4.3}_{-4.3}$	$+556.5^{+23.2}_{-23.0}$
$50 \leq \theta_{e\gamma} \leq 150 \text{ mrad}$	$-0.1^{+4.0}_{-6.4}$	$+13.0^{+2.2}_{-2.1}$	$+446.8^{+20.4}_{-20.2}$
$-150 \leq \phi_{e\gamma} \leq -50 \text{ mrad}$	$-3.5^{+5.9}_{-3.4}$	$+20.6^{+3.4}_{-3.4}$	$+568.3.5^{+23.5}_{-23.3}$
$50 \leq \phi_{e\gamma} \leq 150 \text{ mrad}$	$-4.2^{+6.7}_{-3.9}$	$+23.7^{+3.9}_{-3.9}$	$+558.6^{+22.9}_{-22.7}$

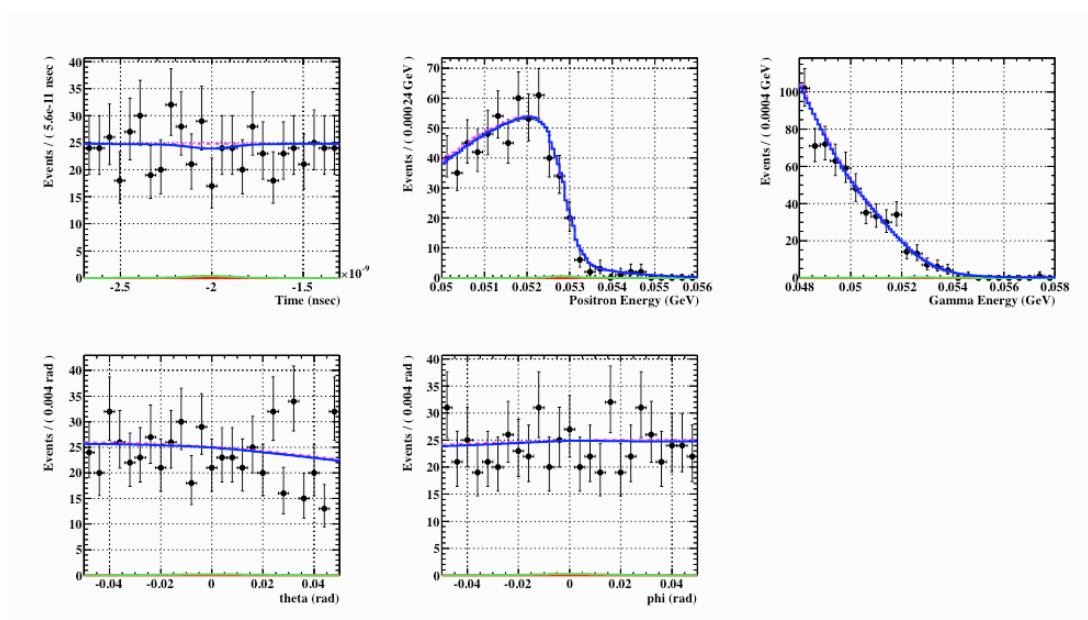
**Table 9.7:** Fit results in angle sidebands.

Figure 9.13 and Figure 9.14 show the likelihood fits in positive and negative time sidebands. Figure 9.15 to Figure 9.18 show the likelihood fit angle sidebands.

## 9. PHYSICS ANALYSIS ON DATA 2010



**Figure 9.13:** Likelihood fit in positive time sideband. Summed PDFs weighted with best fit numbers of each types are superimposed on each plot. The green, red, magenta and blue lines show the signal, RD, background and total sums of PDF respectively.



**Figure 9.14:** Likelihood fit in negative time sideband. Summed PDFs weighted with best fit numbers of each types are superimposed on each plot. The green, red, magenta and blue lines show the signal, RD, background and total sums of PDF respectively.

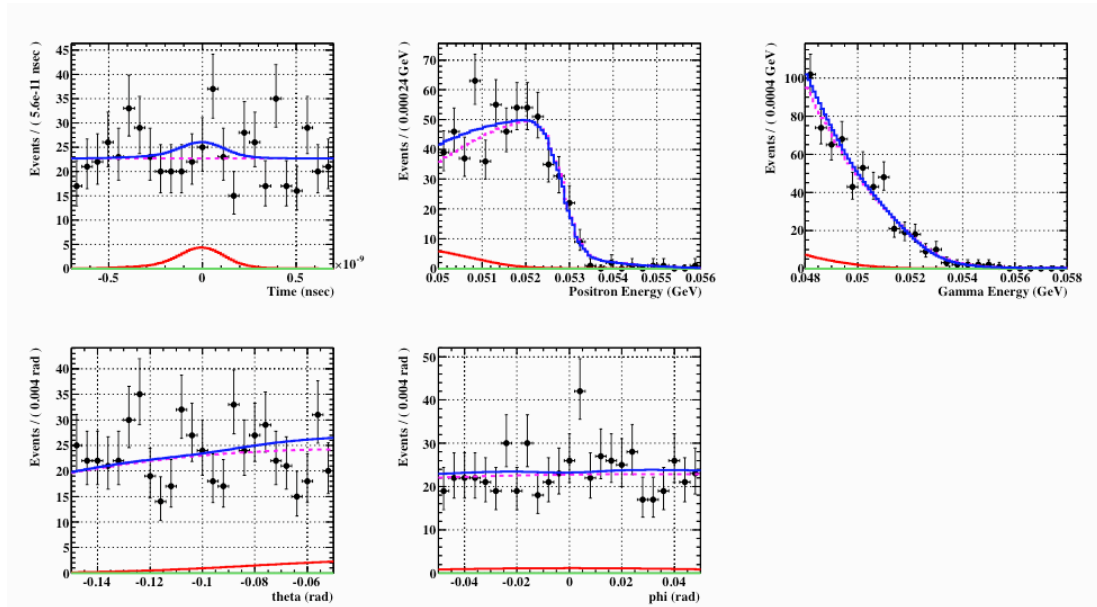


**Figure 9.15:** Likelihood fit in angle sideband. Summed PDFs weighted with best fit numbers of each types are superimposed on each plot. The green, red, magenta and blue lines show the signal, RD, background and total sums of PDF respectively.

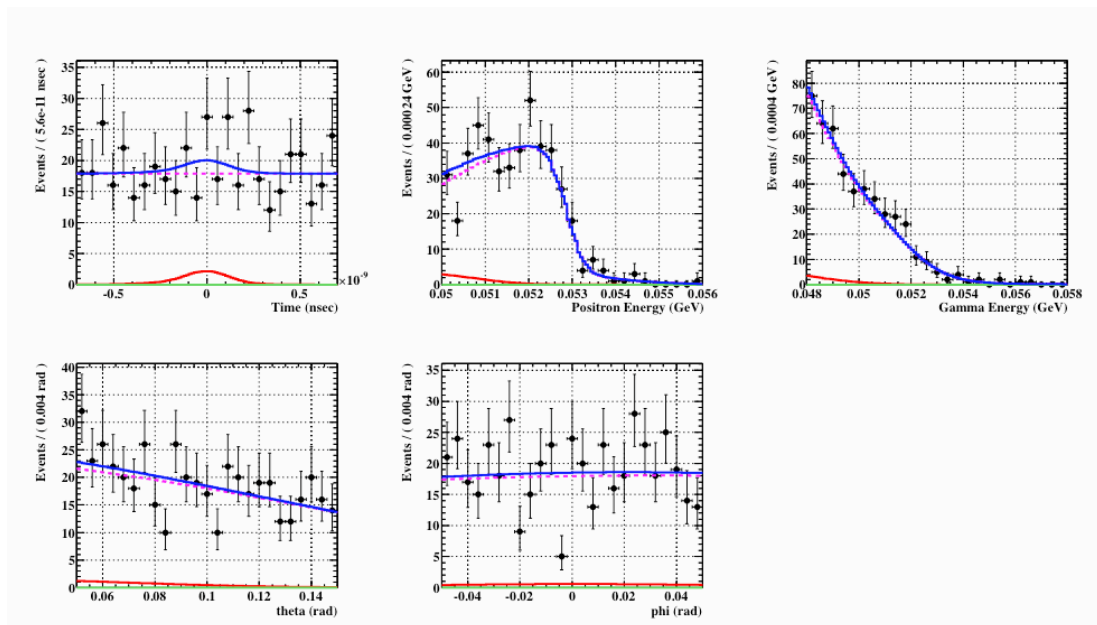


**Figure 9.16:** Likelihood fit in angle sideband. Summed PDFs weighted with best fit numbers of each types are superimposed on each plot. The green, red, magenta and blue lines show the signal, RD, background and total sums of PDF respectively.

## 9. PHYSICS ANALYSIS ON DATA 2010

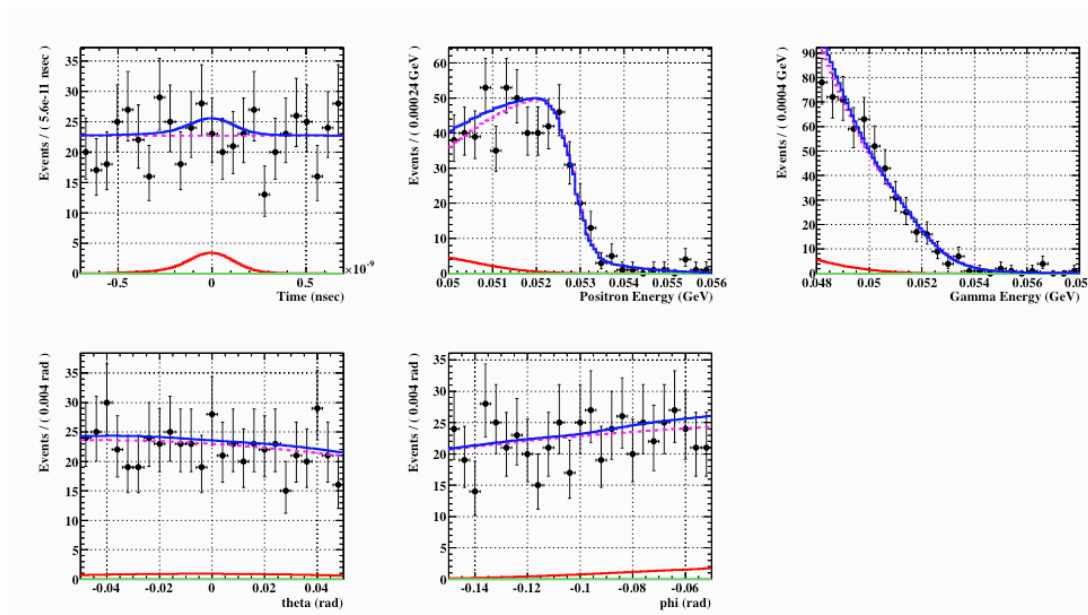


**Figure 9.17:** Likelihood fit in angle sideband. Summed PDFs weighted with best fit numbers of each types are superimposed on each plot. The green, red, magenta and blue lines show the signal, RD, background and total sums of PDF respectively.

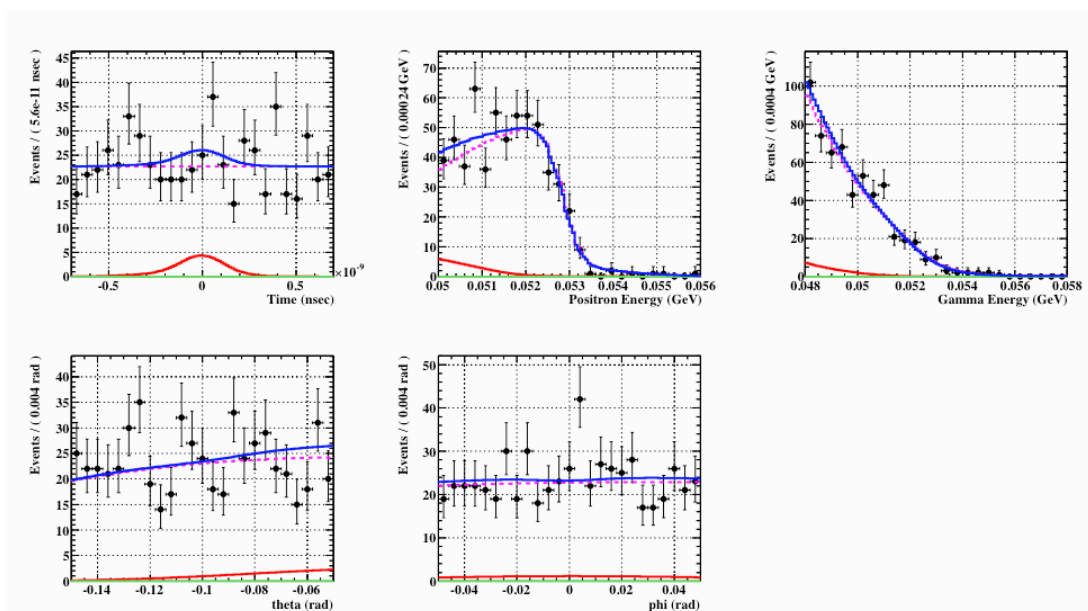


**Figure 9.18:** Likelihood fit in angle sideband. Summed PDFs weighted with best fit numbers of each types are superimposed on each plot. The green, red, magenta and blue lines show the signal, RD, background and total sums of PDF respectively.

### 9.6.2 Sensitivity

The sensitivity of an experiment is a measure of the result that the experiment is expected to give for the limit on a parameter in the absence of signal. It describes accuracy of the experiment, and is independent of the actual data that could fluctuate. We define the 90% confidence sensitivity by the median upper limit at 90% CL of the simulated toy experiments. In each experiment the expected number of RD and BG are given by the values in the signal region estimated with sideband data ( $N_{RD} = 50.2$ ,  $N_{BG} = 608.5$ ) and  $N_{sig}$  is expected to be 0. The upper limit is calculated with the method described in Section 9.3.4.

Fig 9.20 shows the distribution of the upper limit of the number of signal for 1000 experiments (systematic errors are not included). The median is 4.8 for 2010 data. After normalization, it corresponds to a branching ratio of  $2.2 \times 10^{-12}$ .

Figure 9.19 shows the updated sensitivity of 2009 data, which is  $3.3 \times 10^{-12}$ .

The sensitivity for the combined data of 2009 and 2010 is  $1.6 \times 10^{-12}$ , which is shown in Figure 9.21.

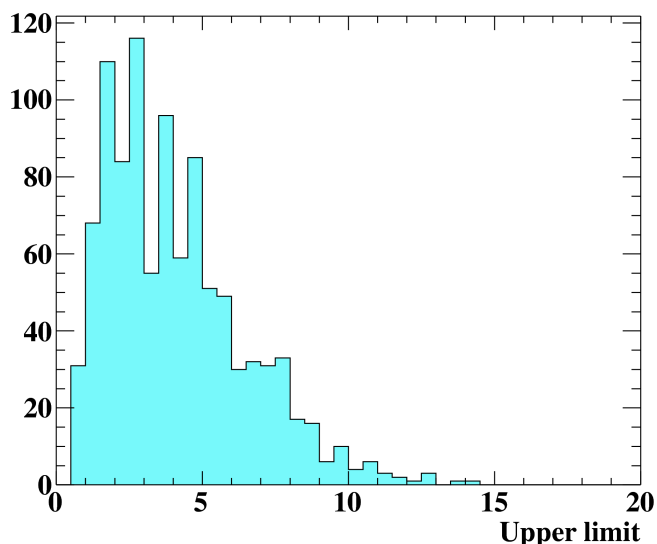
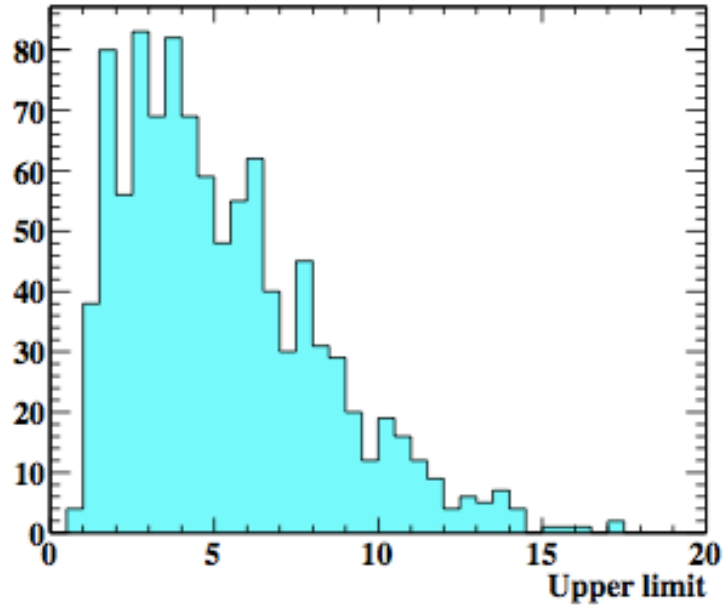
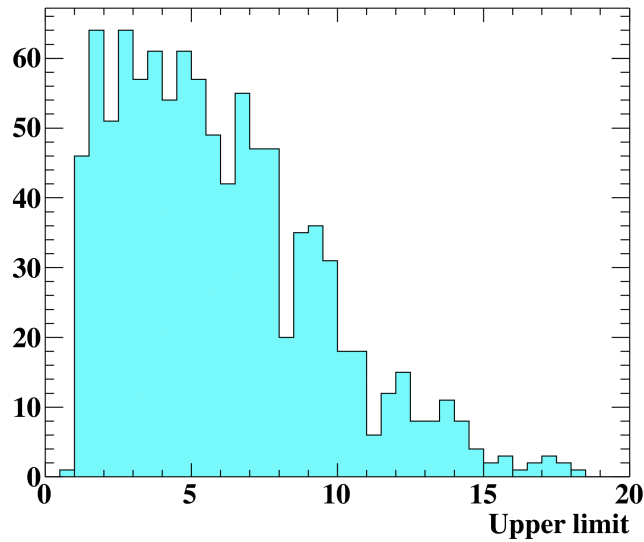


Figure 9.19: Updated result of sensitivity in 2009.



**Figure 9.20:** Distribution of  $N_{sig}$  upper limit at 90% confidence level in toy experiments for 2010 data. A median of this distribution (4.8) is defined as a 90% confidence sensitivity.



**Figure 9.21:** Distribution of  $N_{sig}$  upper limit at 90% confidence level in toy experiments for combined data of 2009 and 2010. A median of this distribution (5.2) is defined as a 90% confidence sensitivity.

## 9.7 Maximum Likelihood Fit on the Data

When we finished the optimization of the analysis and the background studies in the sidebands, we opened the blinding box and performed a likelihood analysis.

For 2009 data, the best fit results are

$$(N_{sig}, N_{RD}, N_{BG}) = (3.4^{+6.6}_{-4.4}, 26.9^{+4.5}_{-4.5}, 273.1^{+12.3}_{-12.3}), N_{obs} = 311 \quad (9.22)$$

Figure 9.22 shows the distribution of each observable with average PDFs scaled with the best fit numbers of each type.

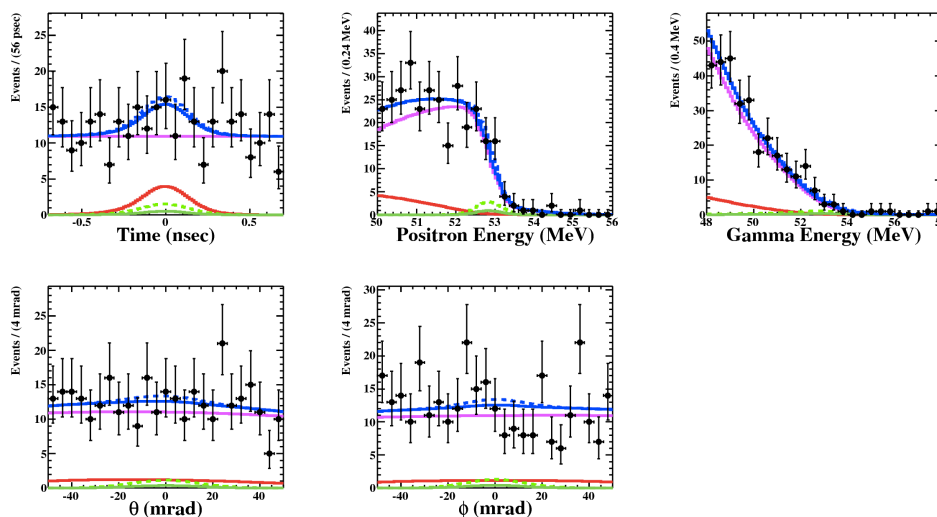


**Figure 9.22:** Updated result of 2009 data. The green, red, magenta and blue lines show the signal, RD, background and total sums of PDF respectively.

For 2010 data, the numbers of signal, radiative muon decay and accidental background are estimated to be,

$$(N_{sig}, N_{RD}, N_{BG}) = (-2.2^{+5.0}_{-1.9}, +50.2^{+9.2}_{-9.2}, +608.5^{+18.7}_{-18.6}) \quad (9.23)$$

where number of analyzed events is  $N_{obs} = 645$  and asymmetric errors are taken from MINUIT of fitting, which is 1.645 sigma MINOS errors.

Figure 9.23 shows the distribution projected onto each observable with averaged PDFs

## 9. PHYSICS ANALYSIS ON DATA 2010

scaled with the best fit number of each type. The blue line is a sum of all PDFs.

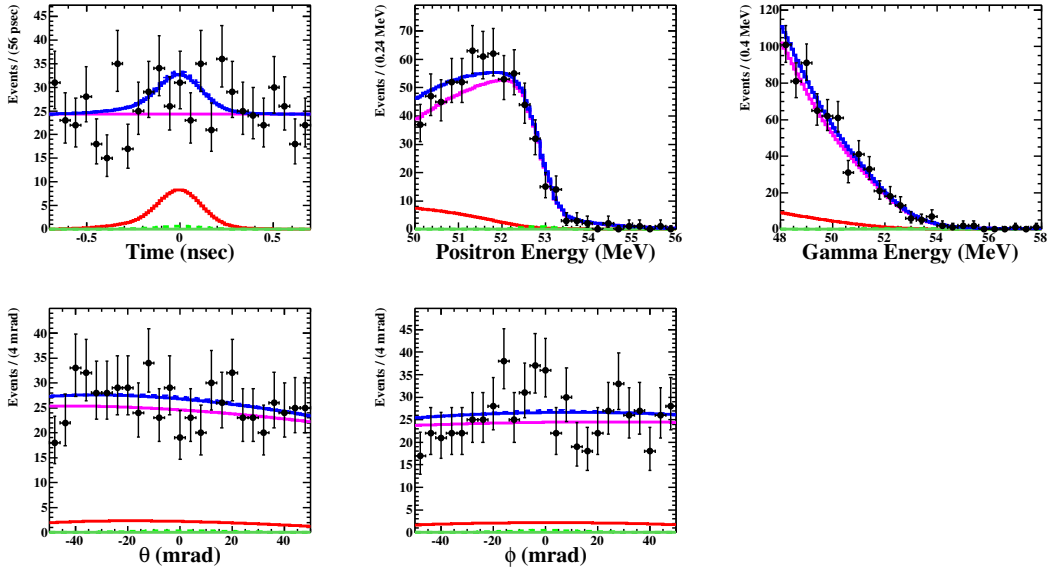


**Figure 9.23:** Result of maximum likelihood fit for 2010 data. Summed PDFs weighted with best fit numbers of each types are superimposed on each plot. The green, red, magenta and blue lines show the signal, RD, background and total sums of PDF respectively.

For the combined data of 2009 and 2010, the best fit results are

$$(N_{sig}, N_{RD}, N_{BG}) = (-0.5^{+7.9}_{-4.7}, +76.5^{+12.0}_{-12.0}, +882.1^{+22.4}_{-22.3}) \quad (9.24)$$

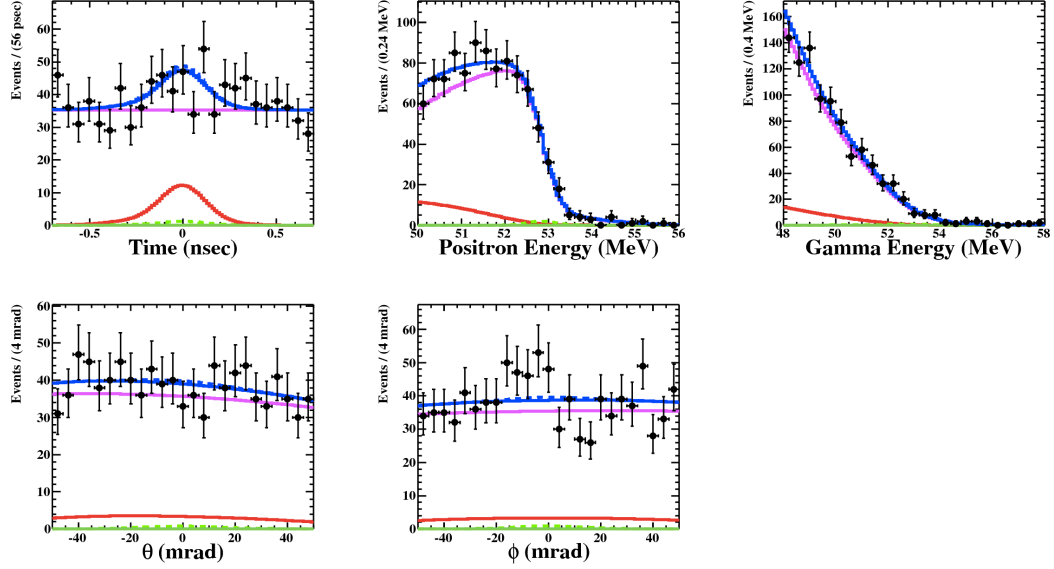
where number of analyzed events is  $N_{obs} = 956$  and asymmetric errors are taken from MINUIT of fitting, which is 1.645 sigma MINOS errors.

Figure 9.24 shows the distribution projected onto each observable with averaged PDFs scaled with the best fit number of each type. The blue line is a sum of all PDFs.

### 9.7.1 Upper Limit on Branching Ratio

Since the fit result is zero-consistent, an upper limit on  $\mu^+ \rightarrow e^+ + \gamma$  branching ratio is set. Together with the normalization factor, the upper limit is calculated to be  $\mathcal{B}(\mu^+ \rightarrow e^+ + \gamma) < 1.7 \times 10^{-12}$  at 90% C.L. for 2010 data and  $\mathcal{B}(\mu^+ \rightarrow e^+ + \gamma) < 2.4 \times 10^{-12}$  for combined data of 2009 and 2010. The total effect of systematic uncertainties is 2%

## 9.7 Maximum Likelihood Fit on the Data



**Figure 9.24:** Result of maximum likelihood fit for combined data of 2009 and 2010. Summed PDFs weighted with best fit numbers of each types are superimposed on each plot. The green, red, magenta and blue lines show the signal, RD, background and total sums of PDF respectively.

change in the upper limit of the combined data set.

The confidence intervals are shown in Table 9.8 to Table 9.10.

	Best fit	LL(90% C.L.)	ULL(90% C.L.)	UL(95% C.L.)	CL@0
$N_{sig}$	3.4	0.2	10.4	11.9	0.92
BR	$3.2 \times 10^{-12}$	$1.7 \times 10^{-13}$	$9.6 \times 10^{-12}$	$1.1 \times 10^{-11}$	0.92

**Table 9.8:** Confidence intervals on 2009 data.

	Best fit	UL(90% C.L.)	UL(95% C.L.)
$N_{sig}$	-2.2	3.8	5.0
BR	$-9.9 \times 10^{-13}$	$1.7 \times 10^{-12}$	$2.3 \times 10^{-12}$

**Table 9.9:** Confidence intervals on 2010 data.

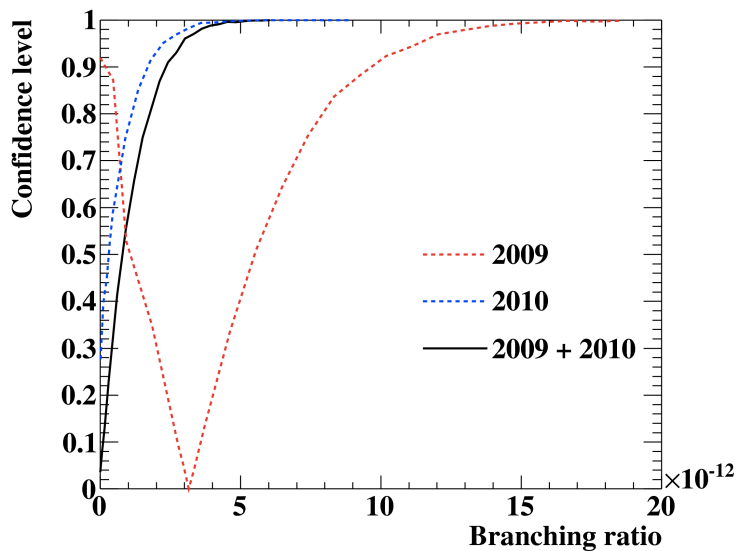


Figure 9.25: Confidence level curve for 2009, 2010 and combined data.

	Best fit	UL(90% C.L.)	UL(95% C.L.)
$N_{sig}$	-0.5	7.8	9.8
BR	$-1.5 \times 10^{-13}$	$2.4 \times 10^{-12}$	$2.9 \times 10^{-12}$

Table 9.10: Confidence intervals on combined data of 2009 and 2010.

### 9.7.2 Event Distribution

The event distributions after the unblinding are shown in Figure 9.26 to Figure ???. The events are labeled with the order of the likelihood ratio defined as  $S/(S + R + B)$ . Figure (a) shows  $E_\gamma$  and  $E_e$  and (b) shows  $t_{e\gamma}$  and  $\cos\Theta_{e\gamma}$ . The best fit result and event distribution of 2009 data is largely unchanged compared to the preliminary result. And an excess of events around the signal region still remain.

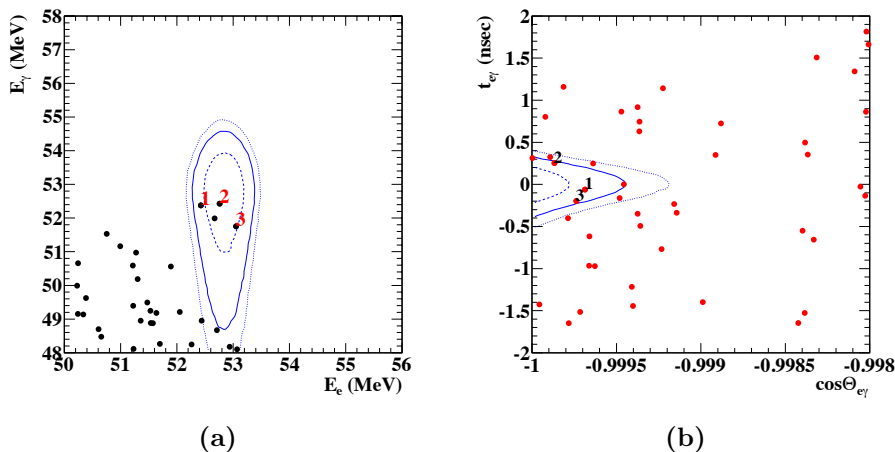


**Figure 9.26:** Updated event distributions in the analysis region for 2009 data. In the left plot, selections in  $t_{e\gamma}$  and  $\theta_{e\gamma}$ , each of which is 90% efficient on the signal, are applied ( $|t_{e\gamma}| < 0.278$  nsec,  $|\theta_{e\gamma}| > 178.34^\circ$ ). In the right plot, a selection in  $E_e$  (90% on the signal) and a selection in  $E_\gamma$  (73% on the signal) are applied ( $51 < E_\gamma < 55$  MeV,  $52.34 < E_e < 55$  MeV).

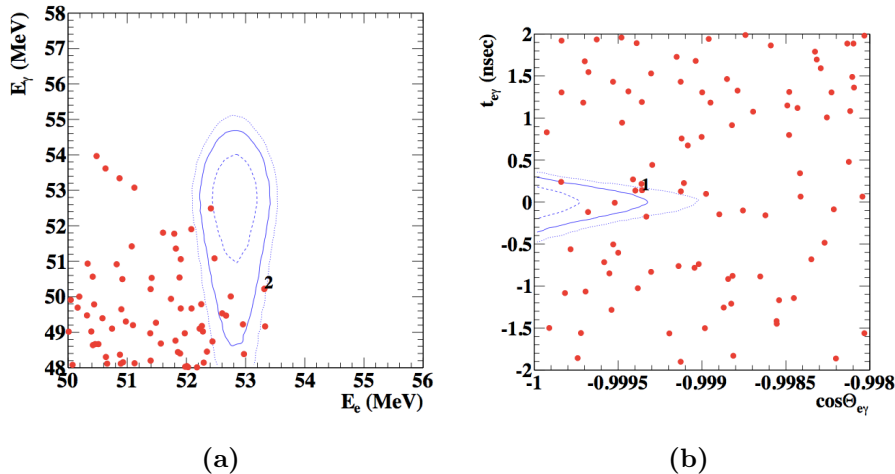


**Figure 9.27:** Event distribution in the analysis region for 2010 data. The signal 2D PDFs are superimposed as contours at 1, 1.64, 2 sigma as blue solid, dot-dashed, and dashed lines respectively. The number shows the rank by  $S/(S + R + B)$ . In plot (a), selections in  $t_{e\gamma}$  and  $\theta_{e\gamma}$ , each of which is 90% efficient on the signal, are applied ( $|t_{e\gamma}| < 0.278$  nsec,  $\cos|\theta_{e\gamma}| < -0.9996$ ). In plot (b), a selection in  $E_e$  (90% on the signal) and a selection in  $E_\gamma$  (73% on the signal) are applied ( $51 < E_\gamma < 55$  MeV,  $52.34 < E_e < 55$  MeV).

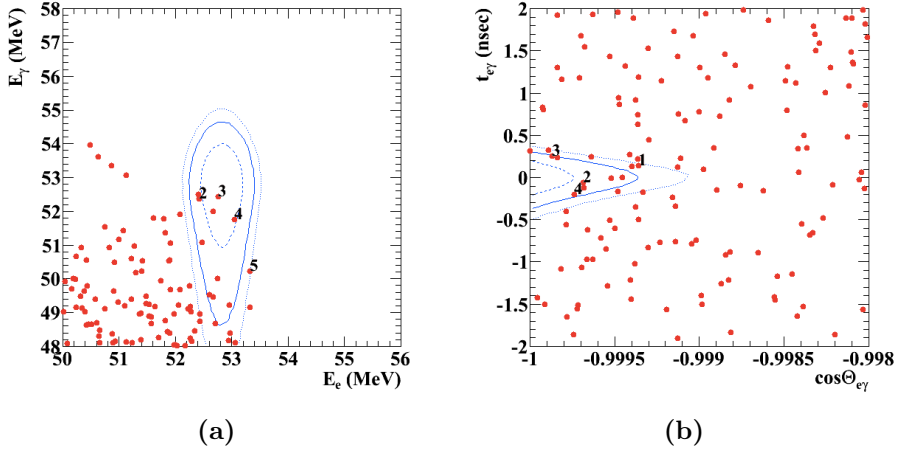


**Figure 9.28:** Event distribution in the analysis region for combined data of 2009 and 2010. The signal 2D PDFs are superimposed as contours at 1, 1.64, 2 sigma as blue solid, dot-dashed, and dashed lines respectively. The number shows the rank by  $S/(S + R + B)$ . Events with rank (2,3,4) are from 2009, events with rank (1,5) are from 2010 data.. In plot (a), selections in  $t_{e\gamma}$  and  $\theta_{e\gamma}$ , each of which is 90% efficient on the signal, are applied ( $|t_{e\gamma}| < 0.278$  nsec,  $\cos|\theta_{e\gamma}| < -0.9996$ ). In plot (b), a selection in  $E_e$  (90% on the signal) and a selection in  $E_\gamma$  (73% on the signal) are applied ( $51 < E_\gamma < 55$  MeV,  $52.34 < E_e < 55$  MeV).

## 9.8 Conclusion

The MEG experiment is a precise rare decay search designed to observe  $\mu^+ \rightarrow e^+\gamma$  or lack thereof as a sensitive low energy probe of new physics. In this thesis we presented an updated result using the data taken in 2010, which correspond to  $1.1 \times 10^{14}$  muon decays in the stopping target.

The previous preliminary result based on the 2009 data gave a higher than expected upper limit of  $1.5 \times 10^{-11}$  at 90% C.L. with a few possible events in the signal region[1][2][3]. To examine this result, we analyzed the 2010 data which has twice higher statistical sensitivity than the 2009 data. In addition, we improved several aspects of calibration and analysis such as detector alignment, implementation of correlations in position observables, improved magnetic field map and improved likelihood analysis. We applied these improvements to the 2009 data and confirmed that the excess signals still remain but the sensitivity is improved.

We adopted a "blind analysis" and a maximum likelihood fit. After unblinding the signal region, the number of  $\mu^+ \rightarrow e^+\gamma$  decay events in the data sample is extracted by a maximum likelihood fit. A 90% confidence interval is then constructed using the Feldman-Cousins technique. We evaluated an expected sensitivity of the 2010 data to be  $2.2 \times 10^{-12}$  by toy Monte Carlo experiment, which was also confirmed by analysis of the side band data. All the analysis is done by hiding the signal region until probability density functions for a likelihood fit are settled upon.

The obtained result is consistent with a null hypothesis and we set an upper limit on the branching ratio

$$B(\mu^+ \rightarrow e^+\gamma) < 1.7 \times 10^{-12} \text{ at 90\% C.L.} \quad (9.25)$$

for the 2010 data and

$$B(\mu^+ \rightarrow e^+\gamma) < 2.4 \times 10^{-12} \text{ at 90\% C.L.} \quad (9.26)$$

## 9. PHYSICS ANALYSIS ON DATA 2010

---

for the combined data of 2009 and 2010. This result exceeds the previous world's best limit of  $1.2 \times 10^{-11}$  set by the MEGA experiment[4].

# 10

## Prospects

MEG continued to take data in 2011 and the total data statistics is doubled with this run. The analysis on data 2011 is ongoing and we expect to continue the data-taking in 2012 and possibly 2013. The total data statistics is expected to be tripled by 2013 and the branching ratio is expected to reach  $\sim 6 \times 10^{-13}$  at 90 % C.L. as shown in Figure 10.1.

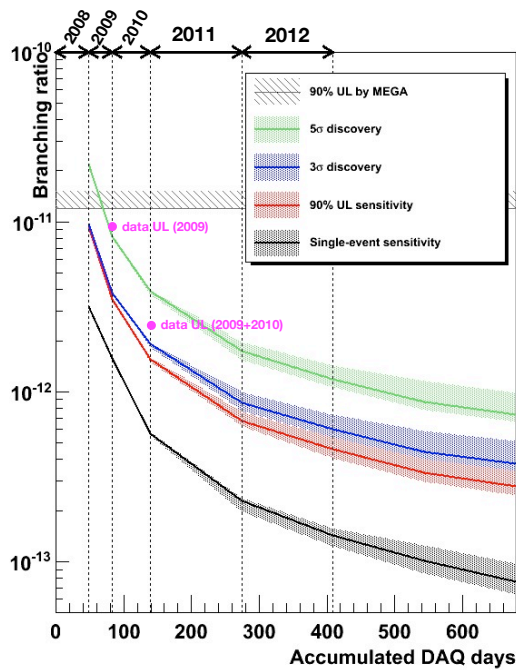


Figure 10.1: Future prospects of sensitivity.

## 10. PROSPECTS

---

We are also considering upgrades to the current detectors in order to further improve sensitivity. One way to increase statistics is to use higher beam rate. However the current positron efficiency is limited to less than 50% due to the material in drift chamber. Use of thinner cables is considered. In order to improve detector performance, currently some ideas such as smaller photodetectors (MPPC) for the LXe detector, new tracking system for positron, timing counter system based on MPPC instead of PMTs, with smaller scintillator cells, etc are under study.

## Acknowledgements

This thesis would not have been possible without the help of many people who contributed and extended their valuable assistance.

First and foremost I would like to express my utmost gratitude to my supervisor, Prof. Toshinori Mori, who provided me opportunities for my doctoral study and supported me throughout the writing of this thesis with his patience and knowledge.

I would like to offer my sincere gratitude to Prof. Wataru Ootani, who gave me tremendous help and support during the writing of this thesis as well as my study in Switzerland.

I would like to thank Prof. Toshiyuki Iwamoto, for his guidance during my study at PSI, and Dr Ryu Sawada, for answering so many of my questions about analysis, and Dr Yusuke Uchiyama, who taught me a lot about calibration. I am greatly indebted to Prof. Satoshi Mihara, Dr. Hajime Nishiguchi, Dr Yasuhiro Nishimura, Mr. Yuki Fujii and Mr. Daisuke Kaneko for their valuable work and advice.

I offer my great appreciation for all the members of the MEG collaboration, without whose hard work the experiment would not have been possible. It has been a great pleasure to work with them.

I am deeply grateful to all of ICEPP members and secretaries.

I would like to convey thanks to PSI for their financial support during my stay at the institute.

Finally, I would like to express my gratitude to my family and friends for their love and support through the duration of my study.

# Bibliography

- [1] Ryu Sawada. Analysis of the MEG experiment to search for  $\mu^+ \rightarrow e^+\gamma$  decays. In *PoS (ICHEP 2010)*, page 263, Paris, 2010.
- [2] Alessandro Massimo Baldini. Rare lepton and k-meson decays. In *PoS (ICHEP 2010)*, page 528, Paris, 2010.
- [3] Y. Nishimura. *A Search for the Decay  $\mu^+ \rightarrow e^+\gamma$  Using a High-Resolution Liquid Xenon Gamma-Ray Detector*. PhD thesis, University of Tokyo, 2010.
- [4] M.L. Books and others. New limit for the family-number non-conserving decay  $\mu^+ \rightarrow e^+\gamma$ . *Phys. Rev. Lett.*, 83:1521, 1999.
- [5] K. Tobe. Lepton flavor violation in susy models with and without r- parity. [arXiv: hep-ph/0008075](https://arxiv.org/abs/hep-ph/0008075).
- [6] Y. Uchiyama. *Analysis of the First MEG Physics Data to Search for the Decay  $\mu \rightarrow e\gamma$* . PhD thesis, University of Tokyo, 2010.
- [7] Photon Cross Sections Data Base. <http://physics.nist.gov/PhysRefData/>.
- [8] MINUIT. Function minimization and error analysis. <http://lcgapp.cern.ch/project/cls/work-packages/mathlibs/minuit/home.html>.
- [9] R. R. Crittenden et al. Radiative decay modes of the muon. *Phys. Rev.*, 121:1823–1832, 1961.
- [10] W. Bertl et al. Search for the decay  $\mu^- \rightarrow e^-e^+e^-$ . *Nucl. Phys. B*, 260:1.31, 1985.
- [11] S. Freedman et al. Limits on neutrino oscillations from  $\bar{\nu}_e$  appearance. *Phys. Rev. D*, 47:811–829, 1993.

## BIBLIOGRAPHY

---

- [12] M. Ahmed et al. Search for the lepton-family-number nonconserving decay  $\mu^+ \rightarrow e^+\gamma$ . *Phys. Rev. D.*, 65:112002, 2002.
- [13] U. Bellgardt et al. Search for the decay  $\mu^- \rightarrow e^-e^+e^-$ . *Nucl. Phys. B*, 299:1–6, 1988.
- [14] R. D. Bolton et al. Search for rare muon decays with the crystal box detector. *Phys. Rev. D*, 38:2077–2101, 1988.
- [15] Particle Data Group. Review of particle physics.
- [16] M. Gell-Mann, P. Ramond, and R. Slansky. *Supergravity*. D. Freedman and P. van Nieuwenhuizen, Amsterdam, 1979.
- [17] R. N. Mohapatra and A. Y. Smirnov. Neutrino mass and new physics. *Ann. Rev. Nucl. Part. Sci.*, 56:569–628, 2006.
- [18] J. I. Illana and M. Masip. Neutrino mixing and lepton flavor violation in susy-gut models. *Acta Phys. Polon*, B34:54135422, 2003.
- [19] M. Dine, Y. Grossman, and S. D. Thomas. Neutrino mixing and lepton flavor violation in susy-gut models. *eConf*, C010630:332, 20001.
- [20] K. S. Hirata et al. Experimental limits on nucleon lifetime for lepton+meson decay modes. *Phys. Lett. B*, 220:308–316, 1989.
- [21] L. Calibbi, A. Faccia, A. Masiero, and S. K. Vempati. Lepton flavour violation from susy-guts: Where do we stand for meg, prism / prime and a super flavour factory,. *Phys. Rev. D*, 74:116002, 2006.
- [22] S. H. Neddermeyer and C. D. Anderson. Note on the nature of cosmic ray particles. *Phys. Rev.*, 51:884–886, 1937.
- [23] H. Yukawa. On the interaction of elementary particles. *Proc. Phys. Math. Soc. Jap.*, 17:48–57, 1935.
- [24] M. Conversi, E. Pancini, and O. Piccioni. On the disintegration of negative mesons. *Phys. Rev.*, 71:209–210, 1947.

- [25] E. P. Hincks and B. Pontecorve. Search for gamma-radiation in the 2.2- microsecond meson decay process. *Phys. Rev.*, 73:257–258, 1947.
- [26] S. Lokonathan and J. Steingeger. Search for improbable muon decay. *Phys. Rev.*, 98:240, 1955.
- [27] G. Feinberg. Decays of the  $\mu$  meson in the intermediate-meson theory. *Phys. Rev.*, 110:1482–1483, 1958.
- [28] G. Danby et al. Observation of high-energy neutrino reactions and the existence of two kinds of neutrinos. *Phys. Rev. Lett.*, 9:36–44, 1962.
- [29] A. van der Schaaf et al. A search for the decay  $\mu^+ \rightarrow e^+\gamma$ . *Nucl. Phys.*, A340:249–270, 1980.
- [30] W. W. Kinnison et al. Search for  $\mu^+ \rightarrow e^+\gamma$ . *Phys. Rev. D*, 25:2846–2868, 1982.
- [31] F.Xiao. *Measurement of the Radiative Muon Decay Branching Fraction in the MEG Experiment*. PhD thesis, University of California, Irvine, 2010.
- [32] Y. Kuno and Y. Okada. Muon decay and physics beyond the standard model. *Rev. Mod. Phys.*, 73:151, 2001.
- [33] T.Mori et al. Search for  $\mu^+ \rightarrow e^+\gamma$  down to  $10^{-14}$  branching ratio, research proposal to Paul Scherrer Institut, R-99-05, 1999.
- [34] ROHACELL. <http://www.rohacell.com>.
- [35] R. Sawada. *A Liquid Xenon Scintillation Detector to Search for the Lepton Flavor Violating Muon Decay with a Sensitivity of  $10^{-13}$* . PhD thesis, University of Tokyo, 2008.
- [36] D. Lide. *Handbook of Chemistry and Physics 2004-2005*. Crc Pr. I Llc., 2005.
- [37] A. C. H. Hallett. *ARGON, HELIUM AND THE RARE GASES*, volume I. Chap IX, Interscience Publishers, Inc., London, 1961.
- [38] C. W. Fabjan and F. Gianotti. Calorimetry for particle physics. *Rev. Mod. Phys.*, 75:1243–1286, 2003.

## BIBLIOGRAPHY

---

- [39] J. Jortner, L. Mever, S. A. Rice, and E. G. Wilson. Localized excitations in condensed ne, ar, kr, and xe. *J. Chem. Phys.*, 42:4250–4253, 1965.
- [40] L. M. Barkov, A. A. Grebenuk, N. M. Ryskulov, P. Yu. Stepanov, and S. G. Zverev. Measurement of the refractive index of liquid xenon for intrinsic scintillation light. *Nucl. Instr. Meth. A*, 379:482–483, 1996.
- [41] T. Doke et al. Absolute scintillation yields in liquid argon and xenon for various particles. *Jpn. J. Appl. Phys.*, 41:1538–1545, 2002.
- [42] A. Hitachi et al. Effect of ionization density on the time dependence of luminescence from liquid argon and xenon. *Phys. Rev. B*, 27:5279–5285, 1983.
- [43] G. M. Seidel, R. E. Lanou, and W. Yao. Rayleigh scattering in rare-gas liquids. *Nucl. Instr. Meth. A*, 489:189–194, 2002.
- [44] S. Kubota et al. Dynamical behavior of free electrons in the recombination process in liquid argon, krypton, and xenon. *Phys. Rev. B*, 20:3486–3496, 1979.
- [45] Hamamatsu Photonics. <http://www.hamamatsu.com/>.
- [46] T. Haruyama et al. Development of a high-power coaxial pulse tube refrigerator for a liquid xenon calorimeter. *Adv. Cryo. Eng.*, 49:1459–1466, 2004.
- [47] S. Mihara et al. Development of a method for liquid xenon purification using a cryogenic centrifugal pump. *Cryogenics*, 46:688–693, 2006.
- [48] W. Ootani et al. Development of a thin-wall superconducting magnet for the positron spectrometer in the meg experiment. *IEEE Trans. Appl. Superconduct.*, 14:568–571, 2005.
- [49] A. Sharma. Properties of some gas mixtures used in tracking detectors. SLAC-J-ICFA-16-3.
- [50] R. Veenhof. Garfield simulation of gaseous detectors. <http://garfield.web.cern.ch/garfield/>.
- [51] Saint-Gobain Ceramics and Plastics. <http://www.detectors.saint-gobain.com/>.

- [52] MIDAS. Maximum integration data acquisition system. <https://midas.psi.ch/>.
- [53] S. Ritt. The drs chip: cheap waveform digitizing in the ghz range. *Nucl. Instr. Meth. A*, 518:470–471, 2004.
- [54] S. Ritt. Design and performance of the 5 ghz waveform digitizing chip drs3. *Nucl. Sci. Symmp. Conf. Rec. IEEE.*, 4:2485–2488, 2007.
- [55] S. Ritt et al. Application of the drs chip for fast waveform digitizing. *Nucl. Instr. Meth. A*, 623:486–488, 2010.
- [56] A. Devices. Ad9218, 10 bit 3v dual a/d converter. <http://www.analog.com/en/index.html>.
- [57] Xilinx. Virtex ii pro. <http://www.xilinx.com/>.
- [58] GEANT. Detector description and simulation tool version 3.21. <http://wwwasd.web.cern.ch/wwwasd/geant/>.
- [59] ROME. Root based object oriented midas extension. <https://midas.psi.ch/rome/>.
- [60] B. Golden. *In Pursuit of the Rare Decay  $\mu^+ \rightarrow e^+\gamma$ : A Window to the UV Completion of the Standard Model*. PhD thesis, University of California, Irvine, 2012.
- [61] T. Iwamoto, W. Ootani, R. Sawada, and Y. Uchiyama. Relative alignment of sub-detectors for run 2009, MEG technical note TN069, 2011.
- [62] R. E. Kalman. A new approach to linear filtering and prediction problems. *Transaction of the AMSE-J. Basic Engineering*, D82:35–45, 1985.
- [63] Peter Schlper, G. Steinbrueck, and Markus Stoye. Software alignment of the cms tracker using millepede ii. *Comput. Phys. Commun.*, 182:1760–1763, 2006.
- [64] J. Adam et al. Likelihood analysis on MEG data 2009 and 2010, MEG technical note TN074, 2011.